

A Thesis Entitled

**STUDY ON FLOW AND HEAT TRANSFER
CHARACTERISTICS OF
NEWTONIAN/NON-NEWTONIAN FLUIDS**

Submitted to the

Faculty of Science and Technology



For the Award of the Degree of

Doctor of Philosophy

in

MATHEMATICS

by

SHANKARALINGAPPA B M

Research Supervisor

Dr. B. J. GIREESHA

Professor of Mathematics

Department of P.G. Studies and Research in Mathematics,
Jnana Sahyadri, Shankaraghatta - 577 451,
Shivamogga, Karnataka, India.

September 2022

Declaration

I hereby declare that the thesis entitled **Study on Flow and Heat Transfer Characteristics of Newtonian/non-Newtonian Fluids**, submitted to the Faculty of Science and Technology, Kuvempu University for the award of the degree of Doctor of Philosophy in Mathematics is the result of the research work carried out by me in the Department of P.G. Studies and Research in Mathematics, Kuvempu University under the guidance of **Dr. B. J. Gireesha**, Professor, Department of P.G. Studies and Research in Mathematics, Kuvempu University, Jnana Sahyadri, Shankaraghatta.

I also declare that this thesis or part of it has not been submitted for the award of any degree, diploma, title or recognition.

Place: Jnana Sahyadri

Date: 13/09/2022


Shankaralingappa B M



KUVEMPU UNIVERSITY
Department of Mathematics

Dr.B.J.GIREESHA,
M.Sc., M.Phil., Ph.D., Post Doc (USA)
Professor

Certificate

This is to certify that the thesis entitled **Study on Flow and Heat Transfer Characteristics of Newtonian/non-Newtonian Fluids** submitted to the Faculty of Science and Technology, Kuvempu University for the award of the degree of Doctor of Philosophy in Mathematics by **Shankaralingappa B M** is the result of bonafide research work carried out by him under my guidance in the Department of P.G. Studies and Research in Mathematics, Kuvempu University, Jnana Sahyadri, Shankaraghatta.

The matter embodied in this thesis has not been submitted in part or full to any other University or Institute for the award of any degree.

Place: Jnana Sahyadri

Date: 13/09/2022

Dr. B./J. Gireesha

Research Supervisor
Dr. B.J. GIREESHA
M.Sc., M.Phil., Ph.D., PDF (USA)
Professor
Department of Mathematics
Kuvempu University, Jnana Sahyadri
SHANKARAGHATTA-577 451

**DEDICATED TO MY BELOVED
FAMILY, TEACHERS AND
FRIENDS**



Admiration

Dr. B J Gireesha, Professor, Department of Mathematics, Kuvempu University, himself is a dynamic personality, who has been my support throughout my research work and has always been kind enough to supervise my research work with his extreme knowledge and kind support. I am very much grateful to him for giving me an opportunity to pursue my Ph.D under his able guidance, reliable advice, patience and fruitful discussions, which has really helped me a lot. It's my privilege to be his student.

I am extremely grateful to **Prof. C. S. Bagewadi**, Emeritus Professor, Department of Mathematics, Kuvempu University, for his timely suggestions.

I express my utmost gratitude to **Prof. S K Narasimhamurthy** and **Prof. Venkatesha**, Department of Mathematics, Kuvempu University, for their great support and timely suggestions.

I extend my heartfelt gratitude to **Prof. I S Shivakumara**, **Prof. H G Nagaraja**, **Dr. B C Prasannakumara**, and **Dr. K M Eshwarappa**, for their esteemed support and guidance.

My sincere thanks to S H Gange Gowda, Dr. Harshendra, Dr Mallikarjuna I, and Sudhakar K B for their substantial support to pursue my Ph.D.

I extend my heartfelt special thanks to Ms Pavithra, Ms Sushma, Ms Keerthi, Ms Felcita Almeida, Ms Sowmya D O, and Mr Manohar R Gombi for their invaluable contribution in writing my thesis.

My special gratitude to Dr. N G Rudraswamy and Dr. M R Krishna Murthy for their kind support during the initial days of my Ph.D work.

I extend my special thanks to my fellow researchers, Dr. Nagaraja B, Raghavendra, Dr. Ganeshkumar, Dr. Archana, Dr. Sowmya, Dr. Sindhu, Dr. Roja, Mrs. Dhanalakshmi, Dr. Arunkumar, Dr. Devaraja M Naik, Ms. Surekha Desai, Mrs. Bhanumathi, Mrs. Rajeshwari, Ms. Shruthi, Ms. Anitha, Mr. Manjunatha, Ms. Aishwarya and Ms. Kavya for their sincere and valuable support in the department.

A special thanks to Mrs. Latha M P, Mr. Rakesh S M and Mr. Shivakumara, office staff , Department of Mathematics, Kuvempu University for their valuable support in the department.

I take this opportunity to express my heartfelt gratitude to my beloved mother **Smt. Lalithamma** and beloved father **Late. Marulappa** who have been everything to me in my life and I cordially extend my heartfelt thanks to my beloved wife **Asha M S** and my beloved son **Sathwik B S**, for their unconditional, invaluable support throughout my Ph.D period.

Place: Jnanasahyadri

Shankaralingappa B M

Date:

Preface

The study of all fluids in static and dynamic situations is the domain of fluid mechanics. Fluid mechanics is a branch of continuum mechanics that studies the interaction of forces, motions and static situations in a continuous medium. Kinematic, stress, conservation, regulating, and constitutive relationships are the five most beneficial relationships in fluid mechanics issues. The simplification of vector quantities is governed by the choice of the system of interest and the volume of interest, which regulate the analysis of fluid mechanics issues. In fluid mechanics research, combustion and engineering physics encompasses a broad spectrum of problems in multi-phase and particulate flow hydrodynamics, reacting flows, aerodynamics, turbulence and ocean-related flows. The significance of fluid mechanics in civil infrastructure, food production, transportation, materials processing and manufacturing, power generation and conversion cannot be overstated. The study is applicable to a wide range of engineering and industrial fields, including flow across magnetic tapes and disks, bio-fluid dynamics, global climate prediction, aeronautical guidance and control, aircraft and automotive design.

A boundary layer is a thin flow area next to a surface where the flow is impacted by friction between the solid surface and the liquid. Prandtl proposed the essential notion of the boundary layer, which describes the boundary layer as a layer of fluid developing inflows with extremely high Reynolds numbers, that is, with comparatively low viscos-

ity compared to inertial forces. Boundary layer solutions, which are often applicable to shock-free, attached, and subsonic flows, have always been vital for understanding liquid behaviour and have offered extremely significant qualitative information. These concepts are used in the nonstop cooling of fibre, crystallization process techniques, pulling of filaments through a static liquid, vaporization of liquid coatings, and production of rubber and plastic films. Sakiadis (1961) examined the boundary-layer behavior for two-dimensional, axisymmetric flow on continuous solid surfaces. The traditional issue of two-dimensional motion produced by a non-linearly expanding surface was proposed by Vajravelu (2001). Sajid and Hayat (2008) looked into the influence of radiation on the boundary layer flow due to an exponentially stretching sheet. In the presence of nano liquid. Khan et al. (2015) examined the solar energy uses on a 3D flow in a non-linear stretching surface. Recently, Gireesha et al. (2020), Fatunmbi and Okoya (2020), Dawar et al (2021), Puneeth et al. (2021), Raja et al. (2022) carried out effective studies on 3D boundary layer flow of fluid over a stretching sheet.

Non-Newtonian liquid flow in fluid mechanics have piqued the attention of a numerous researchers because of their widespread use in industries and technologies. Paints, emulsions, lubricating oils, suspensions, and various biological liquids are all examples of fluids exhibiting non-Newtonian behaviour. Non-Newtonian liquids are so complicated, that single constitutive equation cannot account for all of their properties. As a result, many non-Newtonian liquid models have been proposed. The explicit solutions for the flow of a non-Newtonian liquid across a stretched sheet were reported by Chang et al. (1991). Abel et al. (2004) investigated the MHD flow owing to a stretched surface with non-Newtonian liquid heat and mass transport. In the presence of free stream velocity, Mustafa et al. (2011) examined the unsteady boundary layer heat transport characteristics of a Casson

liquid generated by a rapidly shifted plate. Recently, Almakki et al. (2019), Irfan et al. (2020), Dahab et al. (2021), Pandey et al (2022) worked on the non-Newtonian behaviour of the fluid in different geometries.

The study of dust particle suspension in a fluid known as the dusty liquid has piqued the interest of various researchers due to its two-phase flow features. Dusty liquid is also associated with a number of practical concerns, such as chemical reactions in raindrops and dusty air, which need mathematical modelling and investigation of the dusty fluid flow. Saffman (1961) initiated the study on influence of dust particles in viscous and laminar flow and computed stability analysis. Vajravelu and Nayfeh (1992) examined the magneto dusty liquid flow past a stretching surface. Chamkha (2000) investigated the Stokes issue in the presence of a magnetic field, heat production, and wall suction impacts for a dusty liquid. Giresha et al. (2018), Souayeh et al (2019), Reddy et al (2021), Khan et al (2022) gave away the results for the flow of dusty fluid under various effects.

Nanoparticle research has become a hot topic of debate owing to its several uses in minerals, oil, solar energy and microelectronics. When compared to bigger particles, nanoparticles with diameters less than or equal to 100 nm may remain suspended in a fluid for a longer duration. The heat-mass transmission capacity of basic liquids is greatly improved as a result of this saturation, and such a liquid is referred to as a nanofluid. Nanoliquids are cutting-edge coolants that outperform traditional liquids like water and oil in terms of cooling efficiency. Unfortunately, the nanofluid has a greater viscosity than the basic fluid. As a result, viscosity has a direct impact on the system's pressure drop and pumping usage. Many studies have noted greater thermal conductivity, superior stability, and low rising pressure loss as essential qualities of nanofluids. On an upright plate, Rana and Bhargava (2011) investigated the heat conveyance improvement in a convective

stream of Ag/CuO/Cu/TiO₂-water-based nanoliquid flow. Sheikholeslami et al. (2014) swotted the MHD impact on the free convective transfer of heat of Cu-water nano liquid past an elliptic cylinder. Hashmi et al. (2017), Nayak et al. (2019), Ashraf et al. (2020), Uddin et al. (2021), Sharif et al. (2022) conferred the MHD stagnation point stream and thermal distribution on a nanofluid in an expanding sheet.

In the era of engineering, biotechnology, and environmental systems, bioconvection has been metalized as a key process. Convection is created by the density of uneven stratification induced by microorganisms moving upstream. Because of their usefulness in ecological fuels, fuel cells, fertilizers, and ethanol, microorganisms' swimming behaviours have been examined in water and a variety of denser materials. The incorporation of microbes in nanomaterials may explain why microscale intermixing, mass transportation, and nanoparticle stability are all being studied. In light of this, many researchers explored the bio convective stream over diverse surfaces. Uddin et al. (2016), Hosseinzadeh et al. (2020), Rana et al. (2021), Imran et al (2022), studied the impact of gyrotactic microorganisms on nanoliquid streams under different circumstances.

Here, we have considered the flows of Newtonian/ non-Newtonian fluids, dusty, nanofluid and hybrid nanofluid upon various geometries in two and three dimensions. The flow governed equations are reduced by using suitable similarity transformation from partial differential equations into ordinary differential equations. Later, these reduced equations have been solved numerically by using Runge-Kutta-Fehlberg's fourth fifth-order approach along with the shooting technique. The numerical extractions are then used to plot graphs and tables. A detailed discussion has been produced of the results obtained in each chapter. Our humble endeavour to examine two and three-dimensional Newtonian/non-Newtonian fluids model is successful. The present thesis work comprises

with the following organized **EIGHT** chapters:

The **First** chapter considers the magnetic effect, Stefan blowing, bioconvection, Cattaneo-Christov theory, and the Buongiorno model in the analysis of heat and mass transfer on the radiative flow of Maxwell nanoliquid across a stretching cylinder. The Runge-Kutta-Fehlberg fourth-fifth order technique (RKF-45) is used to solve the reduced equations, combined with a shooting strategy. Variations in involved profiles as a result of many dimensionless characteristics are also discussed using graphs. The large variability in Brownian factor improves the thermal profile but decreases the concentration profile in this case. The concentration of microorganisms decreases when the microorganism difference parameter and Peclet number increase.

The **Second** chapter focuses on the effect of heat source/sink on flow of nanofluid over an exponentially stretchable sheet containing TiO₂ nanoparticle suspension in base liquid water. The modelling takes into consideration of activation energy, Newtonian heating and the porous medium. The influence of essential aspects on flow fields, heat and mass transfer rates is studied and addressed using graphical representations. The results of this chapter show that when the porosity and suction parameters increase, the velocity field decreases, and as the heat source/sink parameter increases, the heat transfer decreases.

The **Third** chapter focuses on analysing flow, heat and mass transfer characteristics in the context of their applications. The use of non-Newtonian liquids in biological and technological areas has sparked a lot of curiosity. Having such substantial interest in non-Newtonian fluids, our objective was to investigate the flow of Oldroyd-B liquid on a stretched sheet using Cattaneo-Christov double diffusion and a heat source/sink. In addition, the modelling takes into account of relaxation chemical reactions and thermophoretic particle deposition. To offer a clear understanding of the behaviour of dimensionless pa-

rameters on dimensionless velocity, concentration and temperature profiles, physical descriptions are strategized and argued using graphical representations. Here in the chapter, it is concluded that the rise in values of relaxation times parameter of concentration, thermophoretic and chemical reaction rate parameters declines the concentration profile. Similar behaviour is observed in the thermal profile for increasing values of relaxation times parameter of temperature.

The influence of Darcy-Forchheimer flow and Cattaneo-Christov heat transfer of dusty tangent hyperbolic liquid across a stretching sheet is investigated in the **Fourth** chapter. The effects of different factors on velocity and thermal profiles were shown using graphs, and the key characteristics were addressed in depth. Graphs and tables are also used to display the numerical values of the skin friction coefficient and the local Nusselt number. The temperature profile for both the fluid and dust phases is reduced as the Prandtl number is increased. Furthermore, higher values of the radiation parameter generate more heat for the working fluid, resulting in an increase in the temperature profile.

The **Fifth** chapter focuses on the incompressible, laminar 3D flow of a Casson nano liquid when TPD occurs across a non-linearly stretching sheet. The governing equations are framed with enough assumptions in this case, and suitable similarity transformations are used. The numerical findings for linear and non-linear instances are derived, and graphs for different dimensionless restrictions are generated. The results reveal that higher Casson parameter values lower axial velocities but enhance thermal distribution, while higher thermophoretic parameter values lower the concentration profile.

In the **Sixth** chapter, the characteristics of magnetohydrodynamics (MHD) flow and melting heat transfer of dusty Casson fluid across a stretched sheet using a modified version of Fourier's equation and CCHF are studied. The coefficients of the Runge-Kutta

scheme are required to provide precision and refinement in the results. The influence of flow regulating factors on relevant profiles is analyzed quantitatively and qualitatively to have a thorough understanding of the present situation. The graphical and tabular representations of the wall friction factor and heat transfer coefficient calculations are provided. Because of the melting effect, the temperature and thickness of the thermal boundary layer are larger for the relaxation time parameter.

The **Seventh** chapter interrogates the outcome of Alumina (Al_2O_3) nanoparticles shapes (platelet, brick and cylinder) on magnetohydrodynamic (MHD) steady flow of Maxwell liquid past a wedge existing with nonlinear thermal radiation, variable magnetic field and Cattaneo-Christov heat flux impact. Equations administering the flow are formulated by making use of a top mentioned effects and assumptions. To support the research, a diagrammatic depiction of the flow's streamlines has been provided. For increases in the values of the thermal relaxation time parameter, the copy of the output declares that platelet-shaped nanoparticles have greater heat transfer enhancement and that the rate of decline in heat transport is quicker for the brick scenario.

The **Eighth** chapter focuses on the impact of the uniform horizontal magnetic field, heat source/sink and thermal radiation on Zinc Oxide-Society of Automotive Engineers 50 nano lubricant flow (ZnO -SAE50 nano lubricant) over a porous rotating disk. This study utilizes the RKF-45 method with the shooting process to simulate fluid flow, temperature, and mass transfer with the uniform horizontal magnetic field. The outcome reveals that, the radiation plays an important role in increasing the heat transfer for the ZnO -SAE50 nano lubricant flow over the disk surface.

Contents

Preface	i-vii
1 Combined impact of Cattaneo-Christov double diffusion and radiative heat flux on bio-convective flow of Maxwell liquid configured by a stretched nano-material surface	1-24
1.1 Prelude	1
1.2 Mathematical Elucidation	2
1.3 Method of Numerical Extraction	5
1.4 Deliberation of Results	5
1.5 Inference	9
2 Evaluation of heat and mass transfer characteristics in a nanofluid flow over an exponentially stretchable sheet with activation energy	25-41
2.1 Prelude	25
2.2 Mathematical Elucidation	26
2.3 Method of Numerical Extraction	29
2.4 Deliberation of Results	30
2.5 Inference	32
3 The impact of Cattaneo-Christov double diffusion on Oldroyd-B fluid flow over a stretching sheet with thermophoretic particle deposition and relaxation chemical reaction	42-59
3.1 Prelude	42
3.2 Mathematical Elucidation	43
3.3 Method of Numerical Extraction	47
3.4 Deliberation of Results	47
3.5 Inference	50

4	Darcy-Forchheimer flow of dusty tangent hyperbolic fluid over a stretching sheet with Cattaneo-Christov heat flux	60-83
4.1	Prelude	60
4.2	Mathematical Elucidation	61
4.3	Heat Transfer Analysis	64
4.4	Method of Numerical Extraction	66
4.5	Deliberation of Results	68
4.6	Inference	71
5	Influence of thermophoretic particle deposition on the 3D flow of Sodium alginate-based Casson nanofluid over a stretching sheet	84-100
5.1	Prelude	84
5.2	Mathematical Elucidation	85
5.3	Method of Numerical Extraction	88
5.4	Deliberation of Results	90
5.5	Inference	93
6	MHD flow and melting heat transfer of dusty Casson fluid over a stretching sheet with Cattaneo Christov heat flux model	101-120
6.1	Prelude	101
6.2	Mathematical Elucidation	102
6.3	Heat Transfer Analysis	104
6.4	Method of Numerical Extraction	106
6.5	Deliberation of Results	107
6.6	Inference	110
7	Particle shape effect on MHD Water Functionalized Al_2O_3 nanoparticles steady flow over Wedge	121-134
7.1	Prelude	121
7.2	Mathematical Elucidation	122
7.3	Method of Numerical Extraction	125
7.4	Deliberation of Results	126
7.5	Inference	128

8 Significant consequences of uniform horizontal magnetic field on three-dimensional radiative flow of ZnO-SAE50 nano-lubricant over a porous rotating disk	135-149
8.1 Prelude	135
8.2 Mathematical Elucidation	136
8.3 Deliberation of Results	140
8.4 Inference	142
Bibliography	150-163
Nomenclature	164-169
Reprints	170-176

Chapter 1

Combined impact of Cattaneo-Christov double diffusion and radiative heat flux on bio-convective flow of Maxwell liquid configured by a stretched nano-material surface

1.1 Prelude:

The current chapter explores the magnetic effect, Stefan blowing, and bioconvection in the radiative flow of Maxwell nanoliquid on a stretching cylinder. The equations that represent the indicated flow are transformed to ordinary differential equations by choosing relevant similarity variables. The reduced equations are solved using a Runge-Kutta-Fehlberg fourth-fifth order approach (*RKF* – 45) and a shooting system. Physical descriptions are strategized and discussed using graphical representations to provide a clear understanding of the behaviour of dimensionless parameters on dimensionless velocity, concentration, and temperature profiles. The considerable findings obtained using the

presented model persuaded of a decreasing velocity change owing to the curvature constant. As a result of changing the thermal and mass relaxation times parameters, the thermal and concentration trends are both reduced.

1.2 Mathematical Elucidation:

This model considers the bio-convection impact on Maxwell nano-material containing swimming gyrotactic microorganisms over a stretching cylinder. In Maxwell fluid phenomenon also examined the Brownian motion and thermophoresis diffusion. Effect of magnetic field and Cattaneo-Christov double diffusion are discussed in this nanofluid model. The cylinder attaining the radius R_1 compensate the $u_w(t, z) = \frac{az}{1-\gamma_1 t}$ as shown in Fig.(1.1). Before we go any further, we'll assume that all body forces other than those listed above are ignored. The Joule and viscous dissipation, as well as Hall effects are not taken into account. The governing equations by considering the above stated situations of the flows are as follows (see refs. [36], [37] and [38]):

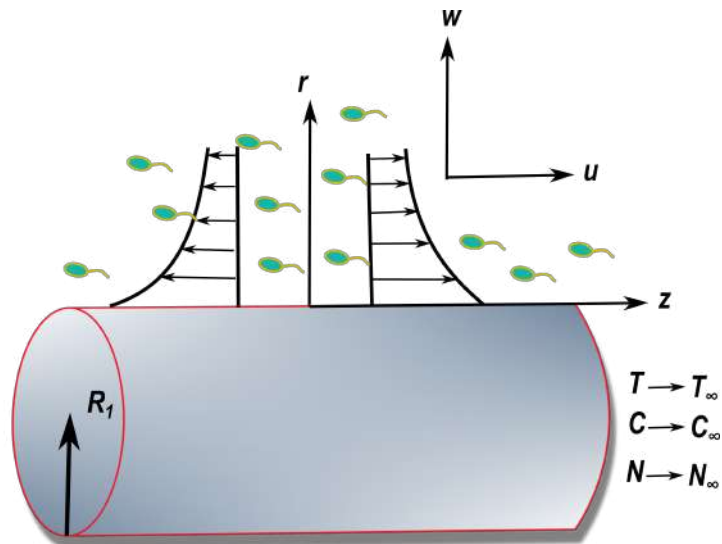


Figure 1.1: Flow Geometry.

$$\frac{\partial(ru)}{\partial z} + \frac{\partial(rw)}{\partial r} = 0, \quad (1.2.1)$$

$$\begin{aligned} \frac{\partial u}{\partial t} + u \frac{\partial u}{\partial z} + w \frac{\partial u}{\partial r} + \lambda_1 \left(\frac{\partial^2 u}{\partial t^2} + u^2 \frac{\partial^2 u}{\partial z^2} + 2u \frac{\partial^2 u}{\partial t \partial z} + w^2 \frac{\partial^2 u}{\partial r^2} + 2w \frac{\partial^2 u}{\partial t \partial r} \right) \\ + \lambda_1 2uw \frac{\partial^2 u}{\partial z \partial r} = \nu_f \left(\frac{1}{r} \frac{\partial u}{\partial r} + \frac{\partial^2 u}{\partial r^2} \right) - \frac{\sigma^* B_0^2}{\rho_f} \left(u + \lambda_1 w \frac{\partial u}{\partial r} \right), \end{aligned} \quad (1.2.2)$$

$$\begin{aligned} \frac{\partial T}{\partial t} + u \frac{\partial T}{\partial z} + w \frac{\partial T}{\partial r} + \lambda_1 \left(\frac{\partial^2 T}{\partial t^2} + \frac{\partial u}{\partial t} \frac{\partial T}{\partial z} + 2u \frac{\partial^2 T}{\partial t \partial z} + \frac{\partial T}{\partial r} \frac{\partial w}{\partial t} + 2w \frac{\partial^2 T}{\partial t \partial r} \right) \\ + \lambda_1 \left(2uw \frac{\partial^2 T}{\partial z \partial r} + u^2 \frac{\partial^2 T}{\partial z^2} + w^2 \frac{\partial^2 T}{\partial r^2} + u \frac{\partial u}{\partial z} \frac{\partial T}{\partial z} + w \frac{\partial u}{\partial r} \frac{\partial T}{\partial z} + u \frac{\partial w}{\partial z} \frac{\partial T}{\partial r} \right) \\ + \lambda_1 w \frac{\partial w}{\partial r} \frac{\partial T}{\partial r} = \alpha_1 \left(\frac{1}{r} \frac{\partial T}{\partial r} + \frac{\partial^2 T}{\partial r^2} \right) - \frac{1}{(\rho C_p)_f} \left[\frac{1}{r} \frac{\partial}{\partial r} (r q_r) \right] \\ + \tau \left[D_B \frac{\partial T}{\partial r} \frac{\partial C}{\partial r} + \frac{D_T}{T_\infty} \left(\frac{\partial T}{\partial r} \right)^2 \right], \end{aligned} \quad (1.2.3)$$

$$\begin{aligned} \frac{\partial C}{\partial t} + u \frac{\partial C}{\partial z} + w \frac{\partial C}{\partial r} + \lambda_C \left(\frac{\partial^2 C}{\partial t^2} + \frac{\partial u}{\partial t} \frac{\partial C}{\partial z} + 2u \frac{\partial^2 C}{\partial t \partial z} + \frac{\partial C}{\partial r} \frac{\partial w}{\partial t} + 2w \frac{\partial^2 C}{\partial t \partial r} \right) \\ + \lambda_C \left(2uw \frac{\partial^2 C}{\partial z \partial r} + u^2 \frac{\partial^2 C}{\partial z^2} + w^2 \frac{\partial^2 C}{\partial r^2} + u \frac{\partial u}{\partial z} \frac{\partial C}{\partial z} + w \frac{\partial u}{\partial r} \frac{\partial C}{\partial z} + u \frac{\partial w}{\partial z} \frac{\partial C}{\partial r} \right) \\ + \lambda_C \left(w \frac{\partial w}{\partial r} \frac{\partial C}{\partial r} \right) = D_B \frac{1}{r} \frac{\partial}{\partial r} \left(r \frac{\partial C}{\partial r} \right) + \frac{D_T}{T_\infty} \frac{1}{r} \frac{\partial}{\partial r} \left(r \frac{\partial T}{\partial r} \right), \end{aligned} \quad (1.2.4)$$

$$\frac{\partial N}{\partial t} + u \frac{\partial N}{\partial z} + w \frac{\partial N}{\partial r} + \frac{b^* W_c}{(C_w - C_\infty)} \left[\frac{\partial}{\partial r} \left(N \frac{\partial C}{\partial r} \right) \right] = D_m \left(\frac{\partial^2 N}{\partial r^2} \right), \quad (1.2.5)$$

Now the suitable boundary constraints for the present flow model are as follows:

$$\left. \begin{aligned} r = R_1, u(t, z, r) = \frac{az}{1-\gamma_1 t}, w(t, z, r) = v_w, T = T_w, C = C_w, N = N_w, \\ r \rightarrow \infty, u \rightarrow 0, T \rightarrow T_\infty, C \rightarrow C_\infty, N \rightarrow N_\infty. \end{aligned} \right\} \quad (1.2.6)$$

The required similarity transformations to reduce the system of partial differential equations into ordinary ones are given by:

$$\left. \begin{aligned} \psi &= \sqrt{\frac{av_f}{1-\gamma_1 t}} z R_1 f(\eta), u = \frac{1}{r} \frac{\partial \psi}{\partial r} = \frac{az}{1-\gamma_1 t} f'(\eta), w = -\frac{1}{r} \frac{\partial \psi}{\partial z} = \frac{-R_1}{r} \sqrt{\frac{av_f}{1-\gamma_1 t}} f(\eta), \\ \eta &= \frac{r^2 - R_1^2}{2R_1} \sqrt{\frac{a}{\nu_f(1-\gamma_1 t)}}, \theta(\eta) = \frac{T - T_\infty}{T_w - T_\infty}, \chi(\eta) = \frac{C - C_\infty}{C_w - C_\infty}, \vartheta(\eta) = \frac{N - N_\infty}{N_w - N_\infty}. \end{aligned} \right\} \quad (1.2.7)$$

After employing the similarity transformation Eq. 1.2.7 the governing Eq.1.2.1 is satisfied and remaining Eqs. 1.2.2-1.2.6 captures its new reduced dimensionless form as follow:

$$\left. \begin{aligned} (1 + 2\alpha\eta) f'''' + 2\alpha f f'' - \frac{S_1}{2} \eta f'' - S_1 f' - f'^2 + f f'' - \frac{7}{4} \beta^* S_1^2 \eta f'' \\ - \frac{\beta^*}{4} \eta^2 S_1^2 f'''' - 2\beta^* S_1^2 f' - 2S_1 \beta^* f'^2 - \beta^* \eta S_1 f' f'' + 3S_1 \beta^* f f'' \\ + S_1 \beta^* \eta f f'' + 2\beta^* f f' f'' - \frac{\alpha\beta^*}{(1+2\alpha\eta)} f^2 f'' - \beta^* f^2 f'''' - M^2 (f' - \beta^* f f'') = 0 \end{aligned} \right\} \quad (1.2.8)$$

$$\left. \begin{aligned} (1 + 2\alpha\eta) \left(1 + \frac{4}{3}R\right) \theta'' + 2\alpha\theta' + \text{Pr} f\theta' - \text{Pr} \frac{S_1}{2} \eta\theta' + (1 + 2\alpha\eta) \text{Pr} N_b \theta' \chi' \\ + (1 + 2\alpha\eta) \text{Pr} N_t \theta'^2 - \text{Pr} \beta_t \left(\frac{3}{4} S_1^2 \eta\theta' - \frac{3}{2} S_1 f\theta' - \frac{S_1}{2} \eta\theta' f'\right) \\ - \text{Pr} \beta_t \left(\frac{1}{4} S_1^2 \eta^2 \theta'' - S_1 \eta f\theta'' + \theta'' f^2 + \theta' f f'\right) = 0 \end{aligned} \right\} \quad (1.2.9)$$

$$\left. \begin{aligned} (1 + 2\alpha\eta) \chi'' + 2\alpha\chi' + \text{Le} \text{Pr} f\chi' - \text{Le} \text{Pr} \frac{S_1}{2} \eta\chi' + (1 + 2\alpha\eta) \text{Pr} \frac{N_t}{N_b} \theta'' \\ + 2\alpha \frac{N_t}{N_b} \theta' - \text{Le} \text{Pr} \beta_C \left(\frac{3}{4} S_1^2 \eta\chi' - \frac{3}{2} S_1 f\chi' - \frac{S_1}{2} \eta\chi' f' + \frac{1}{4} S_1^2 \eta^2 \chi''\right) \\ - \text{Le} \text{Pr} \beta_C (-S_1 \eta f\chi'' + \chi'' f^2 + \chi' f f') = 0 \end{aligned} \right\} \quad (1.2.10)$$

$$(1 + 2\alpha\eta) \vartheta'' + 2\alpha\vartheta' + L_b \text{Pr} f\vartheta' - L_b \text{Pr} \frac{S_1}{2} \eta\vartheta' - \text{Pe} \left(\chi'' (\vartheta + \varpi) + \vartheta' \chi'\right) = 0. \quad (1.2.11)$$

The corresponding reduced boundary condition acquires its shape in the following form:

$$\left. \begin{aligned} f(0) = \kappa\chi'(0), \quad f'(0) = 1, \quad \theta(0) = 1, \quad \chi(0) = 1, \quad \vartheta(0) = 1, \\ f'(\infty) \rightarrow 0, \quad \theta(\infty) \rightarrow 0, \quad \chi(\infty) \rightarrow 0, \quad \vartheta(\infty) \rightarrow 0. \end{aligned} \right\} \quad (1.2.12)$$

Here, $\kappa(\geq 0)$ be blowing constant against mass transfer. Moreover, $\beta_c = \frac{\lambda_c a}{1-\gamma_1 t}$, $N_t = \frac{\tau D_B (T_w - T_\infty)}{T_\infty \nu_f}$, $S_1 = \frac{\gamma_1}{a}$, $\varpi = \frac{N_\infty}{N_w - n_0}$, $M = \sqrt{\frac{\sigma^* l B_0^2}{U_0 \rho_f}}$, $L_b = \frac{\nu_f}{D_m}$, $R = \frac{4\sigma^{**} T_\infty^3}{k k^{**}}$, $Le = \frac{\alpha_1}{D_B}$, $Pe = \frac{bW_c}{D_m}$, $N_b = \frac{\tau D_B (C_w - C_\infty)}{\nu_f}$, $Pr = \frac{\nu_f}{\alpha_1}$, $\beta^* = \frac{\lambda_1 a}{1-\gamma_1 t}$, $\alpha = \frac{1}{R_1} \sqrt{\frac{\nu_f (1-\gamma_1 t)}{a}}$, $\beta_t = \frac{\lambda_t a}{1-\gamma_1 t}$.

The dimensionless form of engineering quantities of interest the Nusselt number (Nu), Sherwood number (Sh) and microorganism's density number (Sn) are given as:

$$Nu Re_x^{\frac{1}{2}} = -(1 - \frac{4}{3}R)\theta'(0), \quad (1.2.13)$$

$$Sh Re_x^{-\frac{1}{2}} = -\chi'(0), \quad (1.2.14)$$

$$Sn Re_x^{-\frac{1}{2}} = -\vartheta'(0) \quad (1.2.15)$$

1.3 Method of Numerical Extraction:

The dimensionless equations expressed in 1.2.8-1.2.11 with 1.2.12 are solved numerically with the implementation of shooting technique. This numerical scheme is preferable due to good accuracy. Since this scheme is famous so the detail of this method has not been presented here [39-41]. The solution confirmation of obtained numerical data is done by performing the comparison with Wang [42], Khan and Pop [43] and Acharya et al. [44] in Table 1.1. A fine agreement is noticed between these investigations.

1.4 Deliberation of Results:

The radiative flow of Maxwell nanofluid on a stretching cylinder is investigated numerically by considering magnetic effect, Stefan blowing and bioconvection. By selecting appropriate similarity variables, the equations that reflect the stated flow are transformed to

Table 1.1: Comparison of numerical results for $-\theta'(0)$ against Pr

	$-\theta'(0)$			
Pr	Wang [42]	Khan and Pop [43]	Acharya et al. [44]	Present results
0.2	0.1691	0.1691	0.16918852	0.169185
0.7	0.4539	0.4539	0.45392176	0.4539315
2.0	0.9114	0.9114	0.91142210	0.9114225
7.0	1.8954	1.8954	1.89541203	1.8954190
20	3.3539	3.3539	3.35397421	3.353986

ordinary differential equations. A numerical scheme is used to give a clear knowledge of the behaviour of flow fields, which have been followed for the graphical frame work. The effect of dimensionless parameters on involved profiles is studied using graphs in this section. The impact of α on $f'(\eta)$ is exposed in Fig.1.2. The increasing values of α upsurges the $f'(\eta)$. Here, the radius of the cylinder increases as the α increases. Hence, fluid flow improves. Fig. 1.3 demonstrates the variation of $f'(\eta)$ for varied β^* . The plot explains that the inclining values of β^* declines the $f'(\eta)$. Physically, the increasing value of β^* increases the stress relaxation phenomena, which reduces the flow properties of nanofluid. Fig. 1.4 demonstrates the variation of $f'(\eta)$ for varied κ . The plot explains that the inclining values of κ declines $f'(\eta)$. The aspects of M for $f'(\eta)$ is expressed via Fig.1.5. The $f'(\eta)$ decreases as the value of M rises. The physical aspect of this behaviour is due to a resistive force produced by magnetic field acting in the axial direction, which causes the fluid velocity to decrease. When a magnetic field is present in the flow field region, the fluid moves more slowly. The Lorentz force, which forces the liquid motion to struggle harder. The Lorentz force is produced by the magnetic field, which acts as a delaying force, resulting in $f'(\eta)$ declination. Fig. 1.6 demonstrates the variation of $f'(\eta)$ for varied

S_1 . The plot explains that the inclining values of S_1 improves the $f'(\eta)$. Here, S_1 has a direct physical relationship with the positive constant a . The unsteadiness parameter is increased by raising a , which increases the cylinder's stretching rate. As a result, as the S_1 increases, the velocity upsurges. The impact of α on $\theta(\eta)$ is revealed in Fig.1.7. The growing values of α upsurges the $\theta(\eta)$. Physically, an improvement in α improves the heat transfer coefficients which augment $\theta(\eta)$. Fig.1.8 depicts the impact of β_t on $\theta(\eta)$. The upward β_t drops the profile of $\theta(\eta)$. The immediate transport of thermal waver control via relaxation time parameters in Cattaneo–Christov theory necessitates extra time for mass and heat transfer. As a result, as β_t increases, the thermal profile decreases. The power of N_b on $\theta(\eta)$ is exposed in Fig.1.9. The upward values of N_b inclines the $\theta(\eta)$. Since there is a commensurate increase in random mobility of nanoparticles with rise in N_b . This rise in random motion leads to an increase in nanoparticles collisions, which converts kinetic energy to heat. As a result of the rise in N_b , the $\theta(\eta)$ of the fluid increases. The inspection in $\theta(\eta)$ in view of N_t is evaluated in Fig.1.10. The peak nature of N_t inclines $\theta(\eta)$. This is because increasing N_t value enhance the force of thermophoresis, which may transport the nanoparticle from a warmer area to the cooler zone to increase the fluid temperature. The impact of R on $\theta(\eta)$ shown in Fig.1.11. The increasing values of R upsurges the $\theta(\eta)$. When R upsurges, the coefficient of mean absorption diminutions. An advanced R effectually transmits more heat to functioning fluids, resulting in a greater upsurge in $\theta(\eta)$. Fig.1.12 demonstrates the variation of $\theta(\eta)$ for varied S_1 . The plot explains that the inclining values of S_1 improves the $\theta(\eta)$. The augmentation of S_1 allows for less heat transmission from the surface. An important finding is that the rate of cooling is considerably quicker for larger values of S_1 , while cooling under steady flows may take longer. Fig.1.13 portrays the impact of β_c on $\chi(\eta)$. The rise in values of β_c

declines the $\chi(\eta)$. The immediate transmission of thermal waver control via relaxation time parameters in Cattaneo–Christov theory necessitates extra time for mass and heat transfer. As a result, as β_c increases, the $\chi(\eta)$ decreases. Fig.1.14 portrays the impact of Le on $\chi(\eta)$. The rise in values of Le declines the $\chi(\eta)$. Brownian diffusion coefficient and Le are inversely correlated. For the greater values of Le , the lower the thermal diffusivity and the higher the Brownian diffusivity of the fluid, which reasons in the lessening of $\chi(\eta)$. Fig.1.15 depicts the influence of N_b on $\chi(\eta)$. The rise in values of N_b declines the $\chi(\eta)$. The advanced values of N_b are the cause of the random mobility between the particles in the fluid. The fluid concentration is reduced as a result of this. The effect of Pe on $\vartheta(\eta)$ shown in Fig.1.16. The increasing values of Pe declines $\vartheta(\eta)$. Bioconvection alters the pattern of microorganisms significantly with higher Pe values. The intrinsic energy of the microorganisms is the source of bioconvection. The mass distribution of microorganisms decreases as they travel faster with advanced Pe . The impact of ϖ on $\vartheta(\eta)$ shown in Fig.1.17. The increasing values of ϖ declines the $\vartheta(\eta)$. The numerical outcome for the influence of pertinent parameters on Nusselt number is showed in Table 1.2. The improved values of N_b , M , β^* , S_1 and R declines the Nusselt number but escalating values of β_t improves the Nusselt number. The numerical outcome for the influence of pertinent parameters on Sherwood number is showed in Table 1.3. The rise in values of β_c , Le , β^* , and S_1 inclines the Sherwood number but escalating values of κ and β_t declines the Sherwood number. The numerical outcome for the influence of pertinent parameters on microorganism's density number is showed in Table 1.4 The rise in values of L_b , β_t , and β^* inclines the microorganism's density number but escalating values of Pe , ϖ , S_1 and β_c declines the microorganism's density number. The three-dimensional (3D) Fig. 1.18 shows the impact of S_1 and M on surface drag force. The growing values of S_1 and M improves

the surface drag force. The three-dimensional (3D) Fig.1.19 shows the impact of S_1 and R on $NuRe^{1/2}$. The growing values of S_1 and R improves the $NuRe^{1/2}$. The 3D Fig.1.20 displays the influence of N_t and N_b on $NuRe^{1/2}$. The growing values of N_t declines the $NuRe^{1/2}$. The impact of N_t and N_b on $ShRe^{-1/2}$ is showed in 3D figure Fig.1.21. The escalating values of N_t and N_b improves the $ShRe^{-1/2}$. The 3D Fig.1.22 portrays the effect of S_1 and Le on $ShRe^{-1/2}$. The rise in values of S_1 inclines the $ShRe^{-1/2}$. The 3D Fig.1.23 explores the impact of L_b and Pe on $SnRe^{-1/2}$. The rise in values of L_b inclines the $ShRe^{-1/2}$ but rise in Pe drops down the $SnRe^{-1/2}$.

1.5 Inference:

The present study exemplifies the radiative flow of Maxwell nanofluid on a stretching cylinder numerically by considering magnetic effect, Stefan blowing and bioconvection effects. By selecting appropriate similarity variables, the equations that reflect the stated flow are transformed to ODEs. The numerical algorithm is followed for simulation task. The effect of dimensionless parameters on involved profiles is studied using graphs. The following are the major findings of the present study:

- The inclining values of S_1 improves the $f'(\eta)$.
- The inclining values of α upsurges the $f'(\eta)$.
- The $f'(\eta)$ decreases as the value of M rises.
- The inclining values of κ and β^* decays the $f'(\eta)$.
- The increase in values of β_t decreases the $\theta(\eta)$.
- The growing values of N_t and N_b inclines the $\theta(\eta)$.

- The increasing values of R and α upsurges the $\theta(\eta)$.
- The rise in values of Le , β_c and N_b declines the $\chi(\eta)$.
- The increasing values of Pe and ϖ declines the $\vartheta(\eta)$.
- The rise in values of N_b , M , β^* , S_1 and R declines the Nusselt number but escalating values of β_t improves the Nusselt number.
- The rise in values of β_c , L_e , β^* , and S_1 inclines the Sherwood number but escalating values of κ and β_t declines the Sherwood number.
- The rise in values of L_b , β_t , and β^* inclines the microorganism's density number but escalating values of Pe , ϖ , S_1 and β_c declines the microorganism's density number.

Table 1.2: Numerical frame work for flow parameters.

N_b	M	β^*	S_1	β_t	R	θ'	Nu
0.1	4	1	0.2	0.5		-1.0918	1.106357
0.2						-0.6843	0.693424
0.3						-0.4451	0.451035
0.4						-0.2904	0.294272
	0.1					-0.839	0.850187
	0.5					-0.8171	0.827995
	1					-0.7923	0.802864
	2					-0.7496	0.759595
		0.1				-0.7371	0.746928
		0.2				-0.7304	0.740139
		0.3				-0.724	0.733653
			0.1			-0.8476	0.858901
			0.3			-0.5399	0.547099
			0.5			-0.2733	0.276944
				0.1		-0.6329	0.641339
				0.2		-0.645	0.6536
				0.3		-0.6576	0.666368
				0.4		-0.6707	0.679643
					0.1	-0.5917	0.670593
					0.2	-0.5234	0.662973
					0.3	-0.476	0.6664

Table 1.3: Computational outcome for Sherwood number.

κ	β_c	β_t	L_e	S_1	β^*	χ'	Sh
0.01	0.5	0.5	1.5	0.2	1	1.5012	-1.5012
0.02						1.5497	-1.5497
0.03						1.6031	-1.6031
-0.01						1.4161	-1.4161
-0.02						1.3783	-1.3783
-0.03						1.3432	-1.3432
	0.1					1.6089	-1.6089
	0.2					1.583	-1.583
	0.3					1.5565	-1.5565
		0.2				1.2385	-1.2385
		0.2				1.3006	-1.3006
		0.3				1.3651	-1.3651
			1			1.8213	-1.8213
			2			1.22	-1.22
			3			0.7527	-0.7527
				0.1		2.2297	-2.2297
				0.3		0.8886	-0.8886
				0.5		-0.3293	0.3293
					0.1	1.7037	-1.7037
					0.3	1.6543	-1.6543
					0.5	1.6075	-1.6075

Table 1.4: Computational outcome for microorganism's density number.

Pe	L_b	ϖ	β_t	β_c	β^*	S_1	$\vartheta'(0)$	Sn
0.01	1.5	0.3	0.5	0.5	1	0.2	-0.4736	0.4736
0.03							-0.4693	0.4693
0.05							-0.465	0.465
	1						-0.444	0.444
	2						-0.4998	0.4998
	3						-0.5419	0.5419
		0.1					-0.474	0.474
		0.2					-0.4738	0.4738
		0.4					-0.4734	0.4734
			0.1				-0.4727	-0.4727
			0.2				-0.4729	-0.4729
			0.3				-0.4732	-0.4732
				0.1			-0.474	-0.474
				0.2			-0.4739	-0.4739
				0.3			-0.4738	-0.4738
					0.1		-0.4978	-0.4978
					0.2		-0.4948	-0.4948
					0.3		-0.4919	-0.4919
						0.1	-0.5856	-0.5856
						0.3	-0.3737	-0.3737
						0.5	-0.214	-0.214

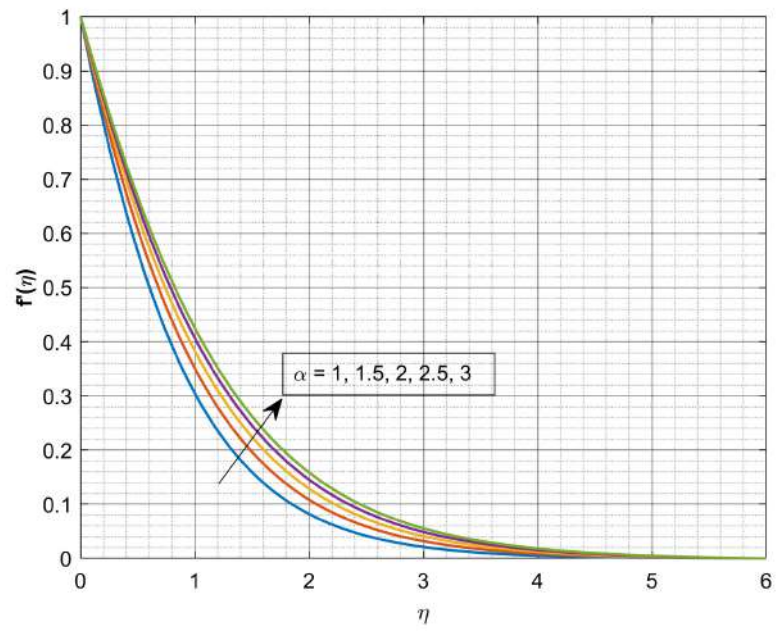


Figure 1.2: Impact of α on $f'(\eta)$.

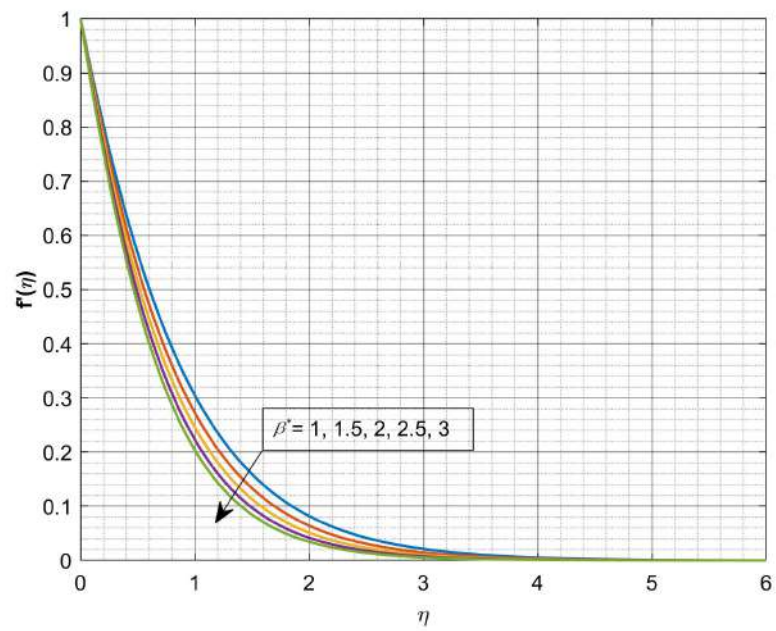


Figure 1.3: Impact of β^* on $f'(\eta)$.

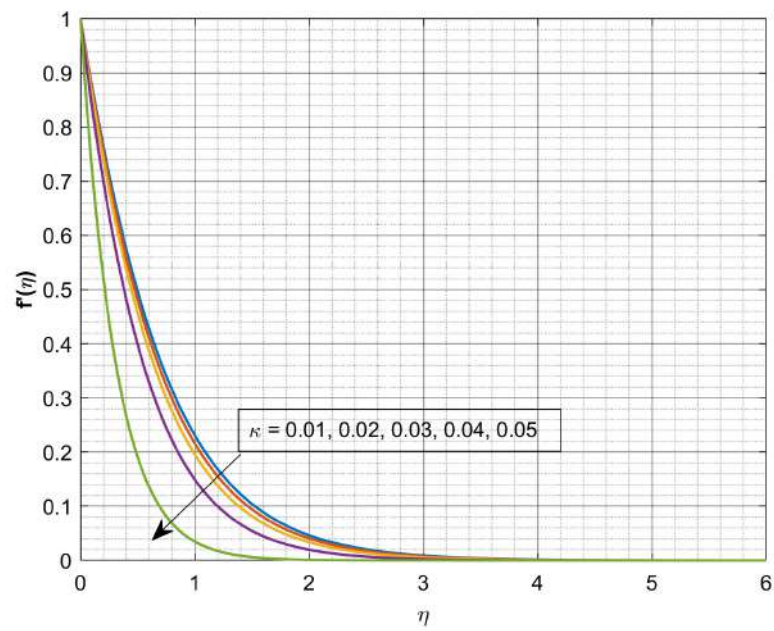


Figure 1.4: Impact of κ on $f'(\eta)$.

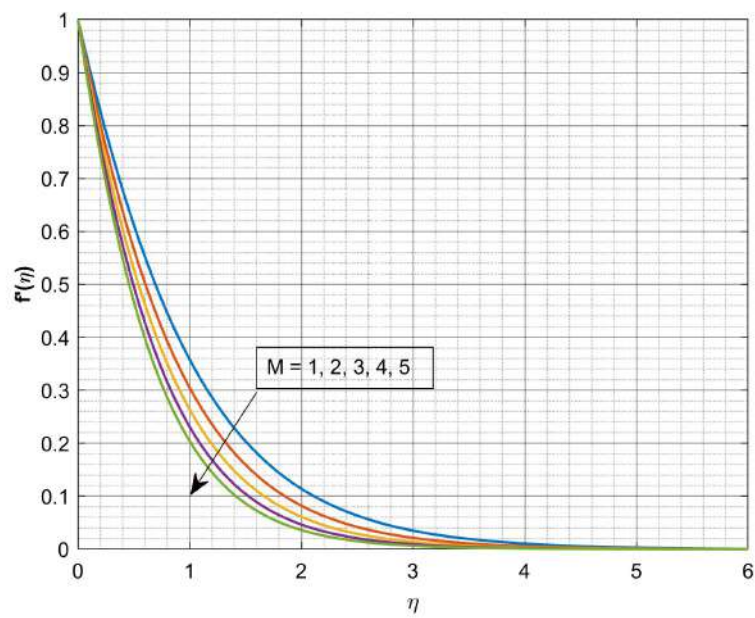


Figure 1.5: Impact of M on $f'(\eta)$.

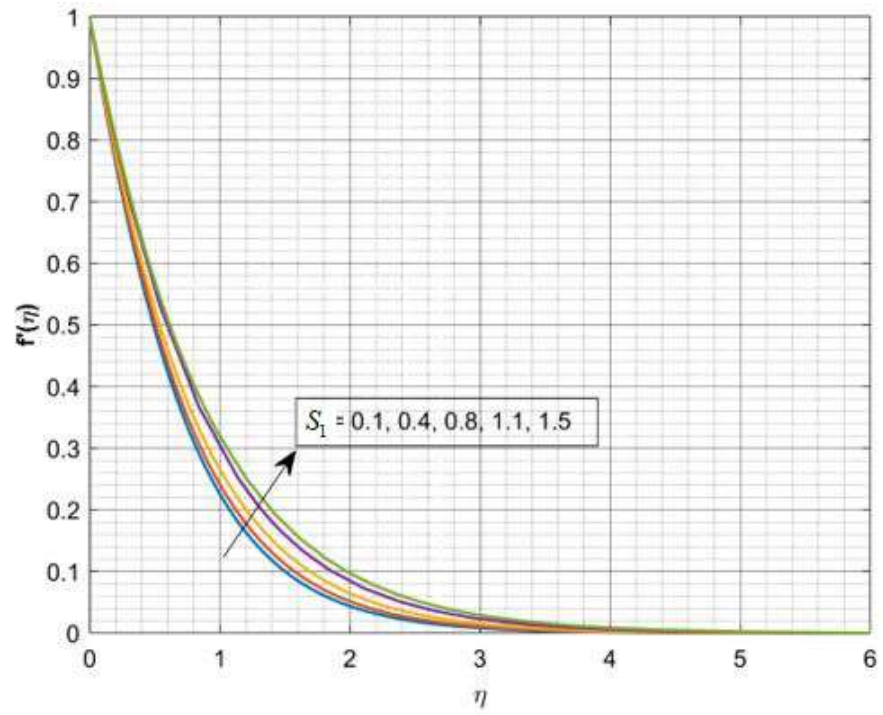


Figure 1.6: Impact of S_1 on $f'(\eta)$.

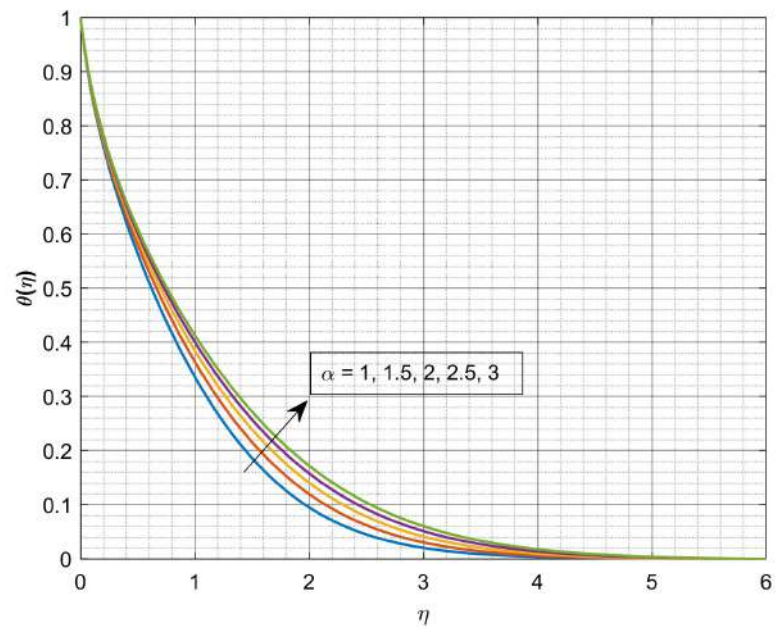


Figure 1.7: Impact of α on $\theta(\eta)$.

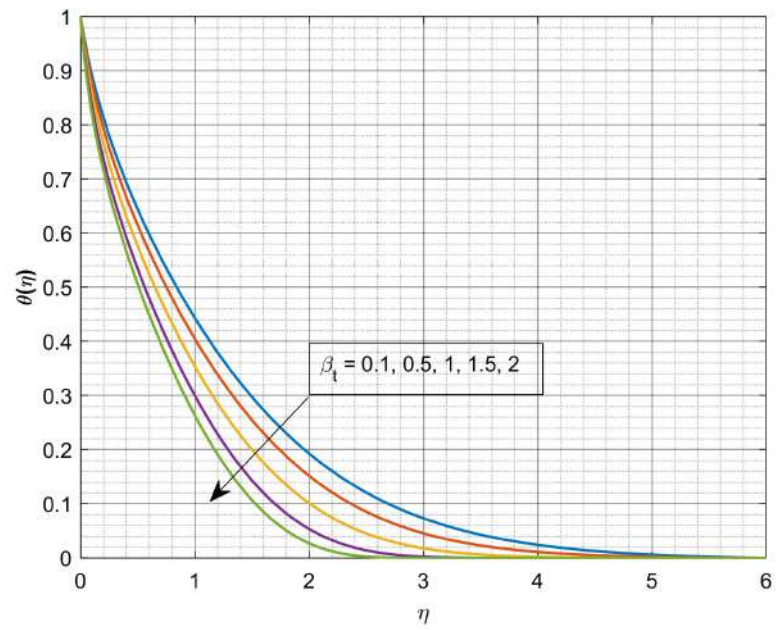


Figure 1.8: Impact of β_t on $\theta(\eta)$.

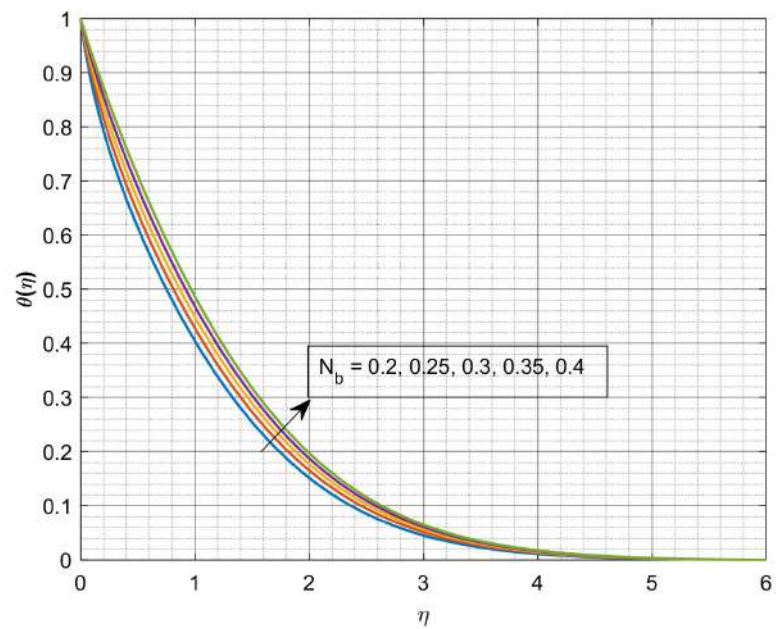


Figure 1.9: Impact of N_b on $\theta(\eta)$.

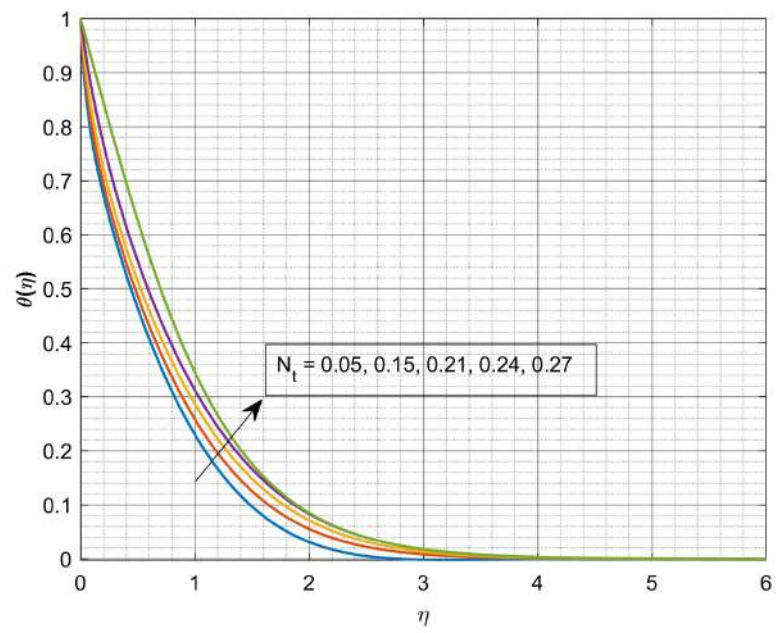


Figure 1.10: Impact of N_t on $\theta(\eta)$.

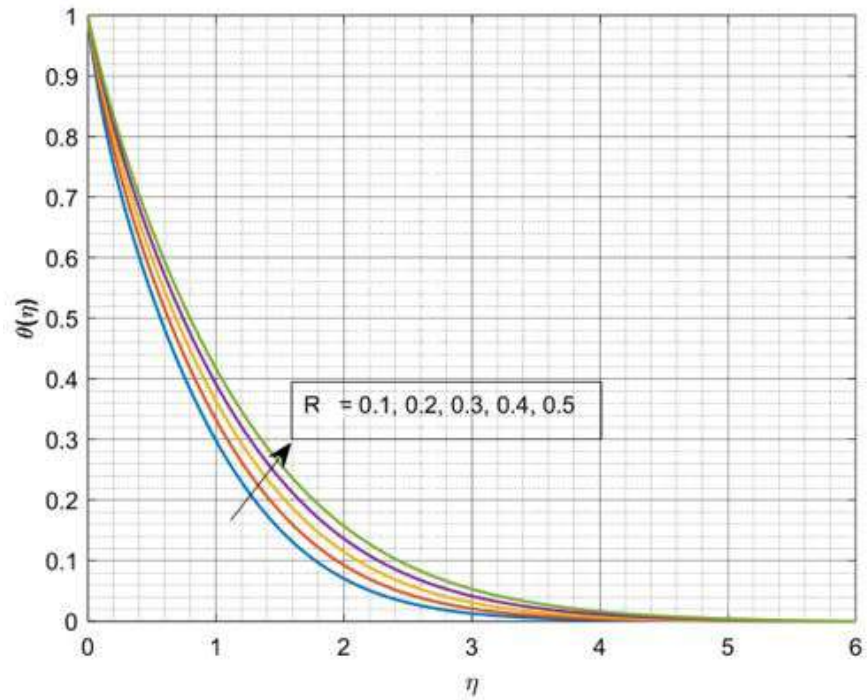


Figure 1.11: Impact of R on $\theta(\eta)$.

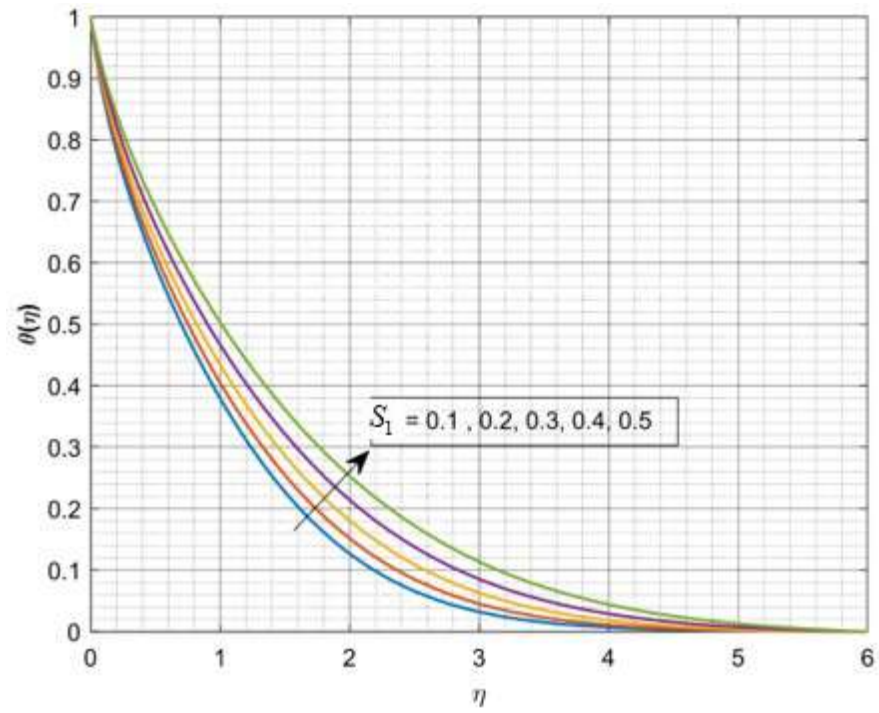


Figure 1.12: Impact of S_1 on $\theta(\eta)$.

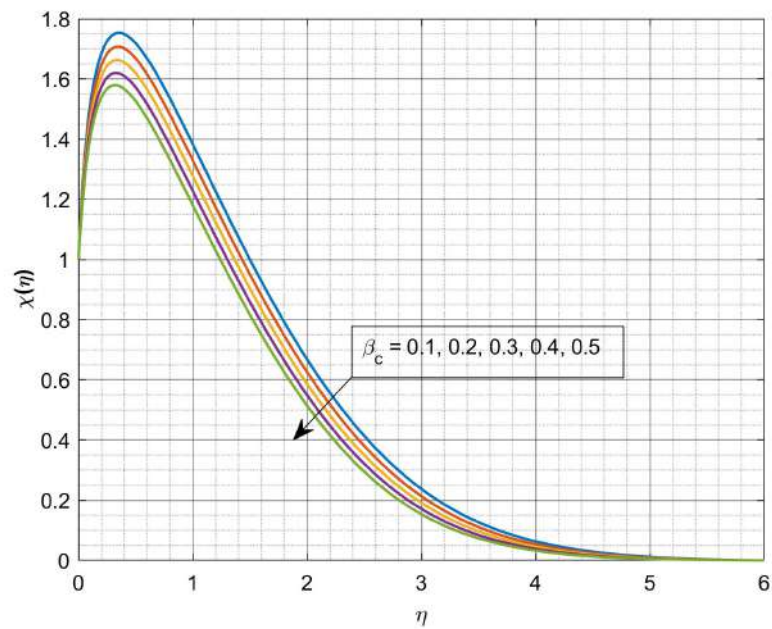


Figure 1.13: Impact of β_c on $\chi(\eta)$.

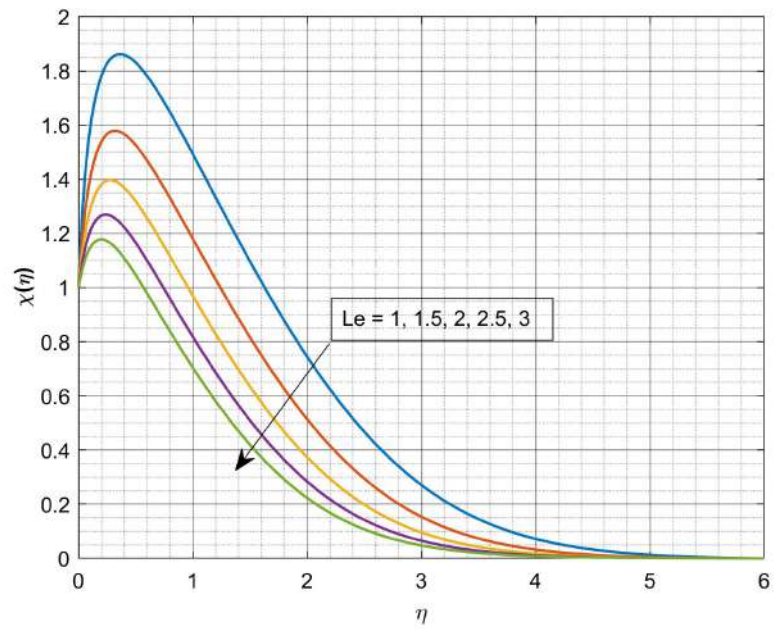


Figure 1.14: Impact of Le on $\chi(\eta)$.

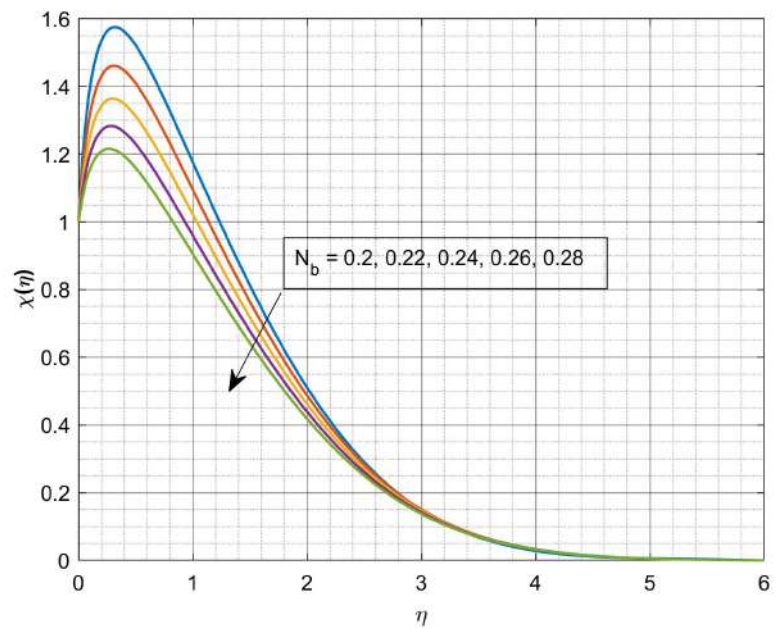


Figure 1.15: Impact of N_b on $\chi(\eta)$.

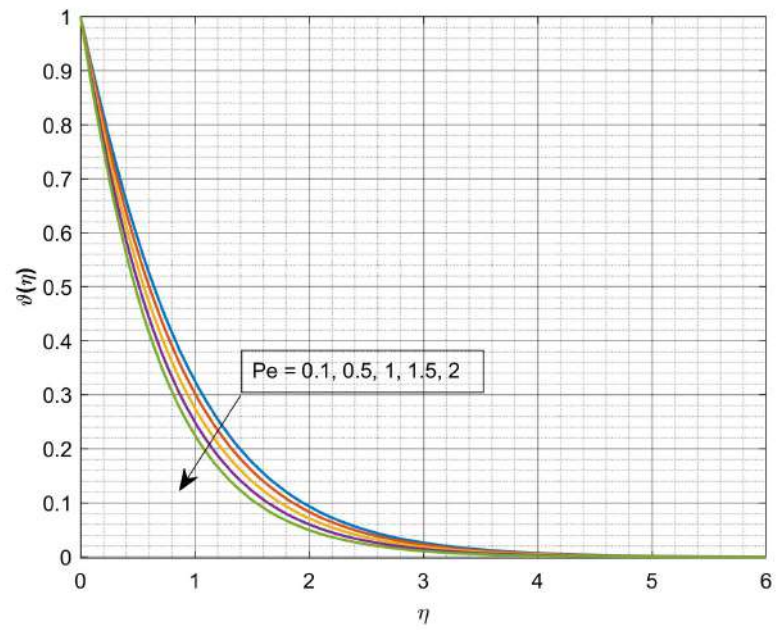


Figure 1.16: Impact of Pe on $v(\eta)$.

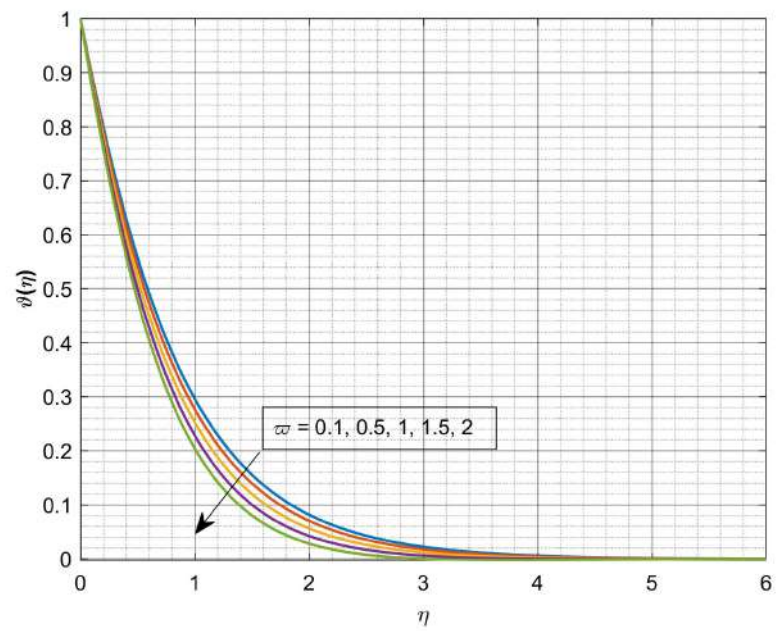


Figure 1.17: Impact of ω on $v(\eta)$.

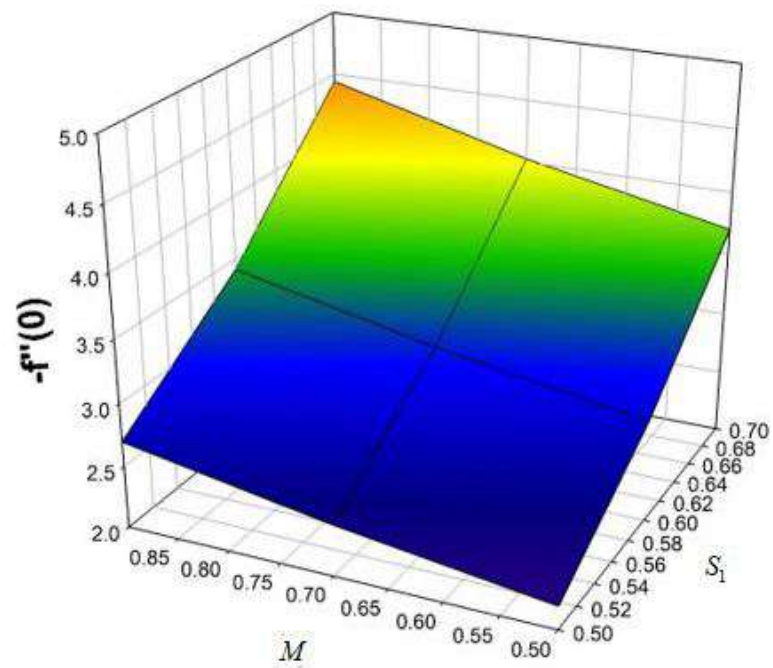


Figure 1.18: Impact of S_1 and M on $-f''(0)$.

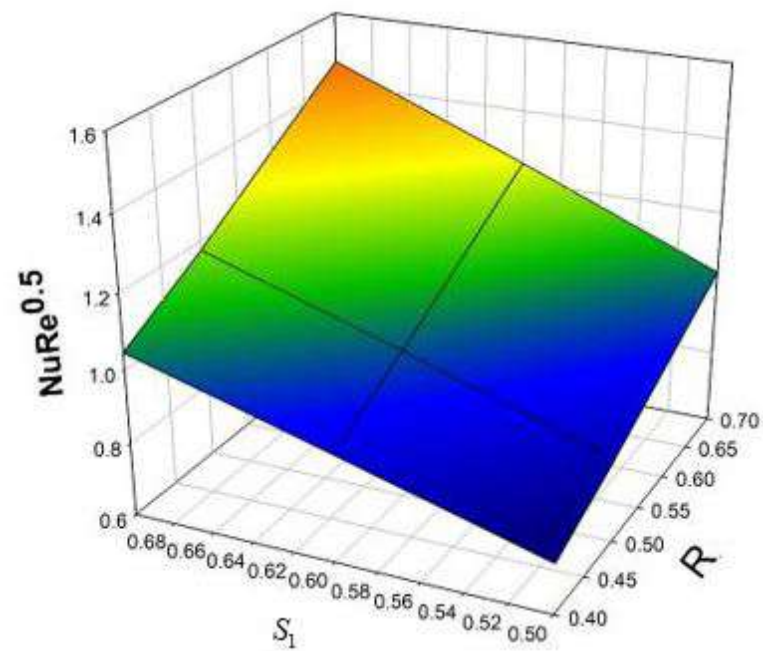


Figure 1.19: Impact of S_1 and R on $\text{NuRe}^{1/2}$.

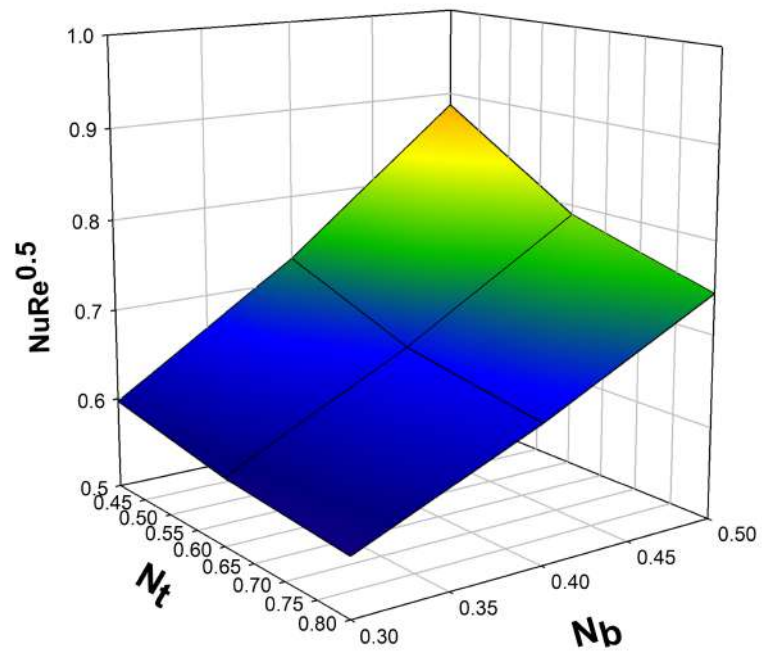


Figure 1.20: Impact of N_t and N_b on $NuRe^{1/2}$.

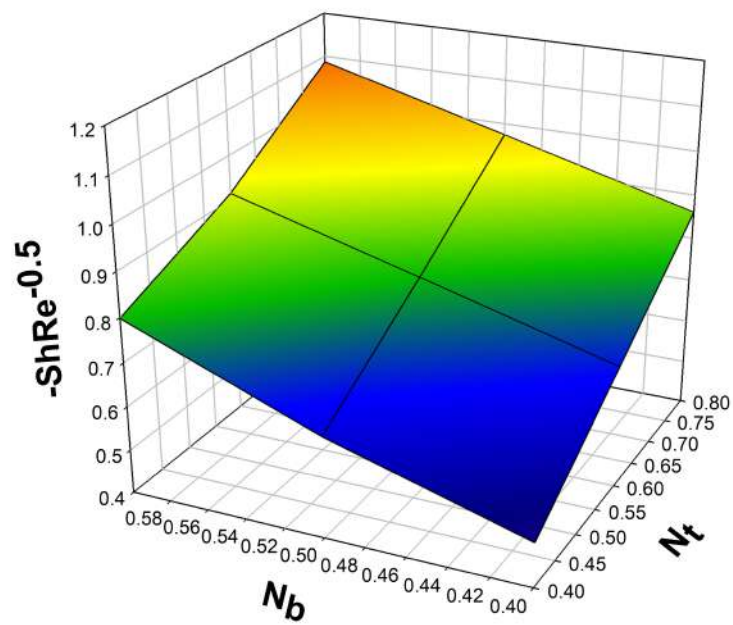


Figure 1.21
Impact of N_t and N_b on $ShRe^{-1/2}$.

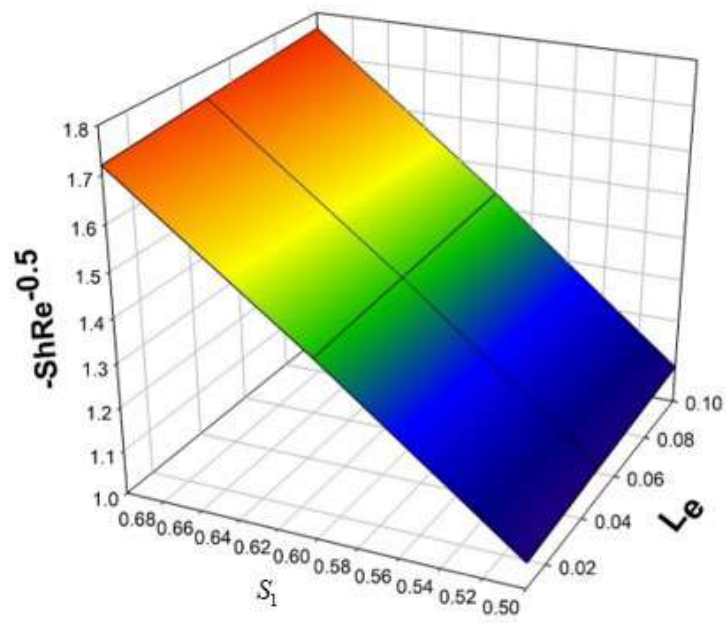


Figure 1.22: Impact of S_1 and Le on $ShRe^{-1/2}$.

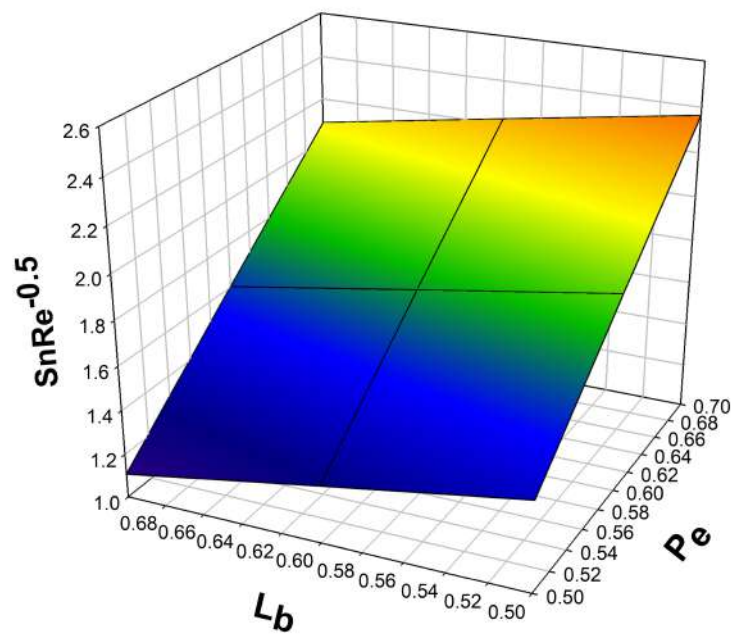


Figure 1.23: Impact of L_b and Pe on $SnRe^{-1/2}$.

Chapter 2

Evaluation of heat and mass transfer characteristics in a nanofluid over an exponentially stretchable sheet with activation energy

2.1 Prelude:

The effect of a heat source/sink on the flow of nanofluid over an exponentially stretchable sheet containing TiO_2 as a nanoparticle suspended in base liquid water is investigated in this chapter. In addition, activation energy, Newtonian heating, and a porous media are all taken into consideration in the simulation. Using similarity transformations, the modelling equations are converted into a system of ordinary differential equations *ODEs*. The Runge Kutta Fehlberg 45 (*RKF45*) technique and shooting strategy are used to numerically solve these equations. The influence of pertinent parameters on flow fields, heat, and mass transfer rates is studied and addressed using graphical representations. The results show that when the porosity and suction parameters increase, the velocity field decreases. The heat transmission decreases as the values of the heat source/sink parameter rises. Furthermore, in the Newtonian heating (*NH*) case, the rate of declination in heat transport is quicker than in the common wall temperature (*CWT*) case.

2.2 Mathematical Elucidation:

Consider a two-dimensional flow of nanofluid across an exponential stretching sheet in the presence of a porous material. Heat source/sink, activation energy, and Newtonian heating are also considered. The x axis is taken along the direction of sheet is stretching and y axis is normal to x axis. Further the sheet is stretched by keeping origin fixed as shown in Fig. 2.1. The surface is elastic in nature and stretching in the direction of x with velocity $U = U_1 e^{\frac{x}{l}}$. The temperature of the sheet is T_w and it is given by $T_w = T_\infty + T_0 e^{\frac{x}{2l}}$. T_∞ is far field temperature and T_0 is reference temperature. Concentration at the sheet is denoted by C_w and it is given by $C_w = C_\infty + C_0 e^{\frac{x}{2l}}$. C_∞ is ambient concentration and C_0 is concentration distribution in stretching sheet, n is fitted rate constant. Throughout the fluid motion, fluid properties are assumed to be constant.

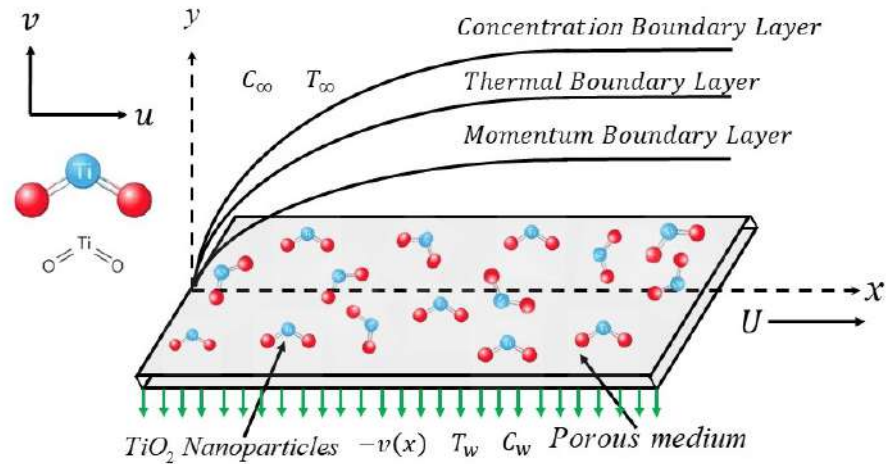


Figure 2.1: Flow Geometry.

Based on the above assumption the governing equations for the described problem are as follows(see refs. [45] and [46]).

$$u_x + v_y = 0, \quad (2.2.1)$$

$$uu_x + vv_y = \nu_{nf}u_{yy} - \frac{\nu_{nf}}{K^*}u, \quad (2.2.2)$$

$$uT_x + vT_y = \frac{k_{nf}}{(\rho C_p)_{nf}}T_{yy} + \frac{\widehat{Q}}{(\rho C_p)_{nf}}(T - T_\infty), \quad (2.2.3)$$

$$uC_x + vC_y = D_{nf}C_{yy} - K_r^2 (TT_\infty^{-1})^n (C - C_\infty) e^{-\frac{E_a}{KT}}, \quad (2.2.4)$$

The related boundary conditions are given by (see ref. [45]):

$$\left. \begin{aligned} u = U, v = -v(x) = -v_0 e^{\frac{x}{2l}}, C = C_w, T = T_w (CWT), \\ \frac{\partial T}{\partial y} = -h_1 e^{\frac{x}{2l}} T (NH) \text{ at } y = 0 \\ u \rightarrow 0, C \rightarrow C_\infty, T \rightarrow T_\infty \text{ as } y \rightarrow \infty \end{aligned} \right\} \quad (2.2.5)$$

The following similarity variables are introduced:

$$\left. \begin{aligned} \eta = \sqrt{\frac{U_1}{2\nu_f l}} y e^{\frac{x}{2l}}, \Psi = \sqrt{2\nu_f U_1 l} e^{\frac{x}{2l}} f(\eta), u = \frac{\partial \Psi}{\partial y} = f'(\eta) e^{\frac{x}{2l}} U_1, \\ v = -\frac{\partial \Psi}{\partial x} = -\sqrt{\frac{\nu_f U_1}{2l}} e^{\frac{x}{2l}} (f'(\eta)\eta + f(\eta)), \theta = \frac{T - T_\infty}{T_w - T_\infty}, \chi = \frac{C - C_\infty}{C_w - C_\infty} \end{aligned} \right\} \quad (2.2.6)$$

The effective properties of nanofluid are provided as (see refs. [47], [48] and [49]): The density of TiO_2 is $4250 kgm^{-3}$, the specific heat of TiO_2 is $686.2 Jkg^{-1}K^{-1}$, the thermal conductivity of TiO_2 is $8.9538 Wm^{-1}K^{-1}$. The density of water is $997.1 kgm^{-3}$, the specific heat of water is $4179 Jkg^{-1}K^{-1}$, the thermal conductivity of water is $0.613 Wm^{-1}K^{-1}$. The expressions for thermal conductivity, specific heat capacity, dynamic viscosity, density

and mass diffusivity of nanofluids are given by:

$$k_{nf} = \frac{k_s + 2k_f - 2\phi(k_f - k_s)}{k_s + 2k_f + 2\phi(k_f - k_s)} k_f, \quad (2.2.7)$$

$$(\rho C_p)_{nf} = (\rho C_p)_f \left(1 - \phi + \phi \left(\frac{(\rho C_p)_s}{(\rho C_p)_f} \right) \right), \quad (2.2.8)$$

$$\mu_{nf} = \frac{\mu_f}{(1 - \phi)^{2.5}}, \quad (2.2.9)$$

$$\rho_{nf} = \rho_f \left(1 - \phi + \phi \frac{\rho_s}{\rho_f} \right), \quad (2.2.10)$$

$$D_{nf} = D_f (1 - \phi)^{2.5}, \quad (2.2.11)$$

The reduced system of ODEs are as follows:

$$f'''(\eta) + (1 - \phi)^{2.5} \left(1 - \phi + \phi \frac{\rho_s}{\rho_f} \right) \left(f(\eta) f''(\eta) - (2f'(\eta))^2 \right) - K f'(\eta) = 0, \quad (2.2.12)$$

$$\frac{k_{nf}}{k_f} \theta''(\eta) + \text{Pr} \left(1 - \phi + \phi \frac{(\rho C_p)_s}{(\rho C_p)_f} \right) (\theta'(\eta) f(\eta) - f'(\eta) \theta(\eta)) + 2 \text{Pr} Q \theta(\eta) = 0, \quad (2.2.13)$$

$$(1 - \phi)^{2.5} \chi''(\eta) + \text{Sc} (\chi'(\eta) f(\eta) - f'(\eta) \chi(\eta)) - \text{ReSc} (1 + \delta \theta(\eta))^n e^{\frac{-E}{(1 + \delta \theta(\eta))}} \chi(\eta) = 0 \quad (2.2.14)$$

Boundary conditions,

$$\left. \begin{aligned} f'(0) = 1, f(0) = S, \theta(0) = 1 \text{ (CWT)}, \theta'(0) = -\gamma (1 + \theta(0)) \text{ (NH)}, \\ \chi(0) = 1 : \eta = 0, f'(\infty) = 0, \theta(\infty) = 0, \chi(\infty) = 0 : \eta \rightarrow \infty \end{aligned} \right\} \quad (2.2.15)$$

$$\text{where, } K = \frac{2\nu_f l}{K_0 U_1}, Q = \frac{Q_0 l}{(\rho C_p)_f U_1}, \text{Sc} = \frac{\nu_f}{D_f}, \text{Re} = \frac{K_1^2 l}{U_1}, \delta = \frac{T_w - T_\infty}{T_\infty}, E = \frac{E_a}{K T_\infty},$$

$$\gamma = h_1 \sqrt{\frac{2\nu_f l}{U_1}}, S = v_0 \sqrt{\frac{2l}{U_1 \nu_f}}.$$

Engineering coefficients:(see ref [46])

$$Cf_x = \frac{2\tau_w}{\rho_f U^2}, Nu_x = \frac{lq_w}{k_f (T_w - T_\infty)}, Sh_x = \frac{lq_m}{D_f (C_w - C_\infty)} \quad (2.2.16)$$

The terms τ_x , q_w and q_m are defined as follows

$$\left. \begin{aligned} \tau_x &= \mu_{nf} \left(\frac{\partial u}{\partial y} \right)_{y=0}, \quad q_w = -k_{nf} \left(\frac{\partial T}{\partial y} \right)_{y=0}, \quad q_m = -D_{nf} \left(\frac{\partial C}{\partial y} \right)_{y=0} \\ Re_x^{0.5} C f_x &= \frac{f''(0)}{(1-\phi)^{2.5}}, \quad Re_x^{-0.5} Sh_x = -(1-\phi)^{2.5} \chi'(0), \\ Re_x^{-0.5} Nu_x &= -\frac{k_{nf}}{k_f} \theta'(0), \\ Re_x &= \frac{U_1 e^{\frac{x}{l}}}{2\nu_f} \text{ (is Local Reynolds number.)} \end{aligned} \right\} \quad (2.2.17)$$

2.3 Method of Numerical Extraction:

The reduced ordinary differential equations 2.2.12 - 2.2.14 and boundary conditions 2.2.15 are higher order and two-point boundary value problem. To solve these equations, we have first converted into initial value problem and then we guess the missing boundary condition by applying shooting scheme.

$$f'(\eta) = g_1, f''(\eta) = g_2, f'''(\eta) = g_3, \quad (2.3.1)$$

$$g_3 + (1-\phi)^{2.5} \left(1 - \phi + \phi \frac{\rho_s}{\rho_f} \right) (f(\eta)g_2 - (2g_1)^2) - K g_1 = 0, \quad (2.3.2)$$

$$\theta'(\eta) = g_4, \theta''(\eta) = g_5, \quad (2.3.3)$$

$$\frac{k_{nf}}{k_f} g_5 + Pr \left(1 - \phi + \phi \frac{(\rho C_p)_s}{(\rho C_p)_f} \right) (g_4 f(\eta) - g_1 \theta(\eta)) + 2 Pr Q \theta(\eta) = 0, \quad (2.3.4)$$

$$\chi'(\eta) = g_6, \chi''(\eta) = g_7, \quad (2.3.5)$$

$$(1-\phi)^{2.5} g_7 + Sc (g_6 f(\eta) - g_1 \chi(\eta)) - Rc Sc (1 + \delta \theta(\eta))^n e^{\frac{-E}{(1+\delta \theta(\eta))}} \chi(\eta) = 0, \quad (2.3.6)$$

with,

$$\left. \begin{aligned} g_1(0) &= 1, \quad f(0) = S, \quad \theta(0) = 1 \text{ (CWT)}, \quad g_4(0) = -\gamma (1 + \theta(0)) \text{ (NH)}, \\ \chi(0) &= 1 : \eta = 0, \text{ and } g_1(\infty) = 0, \quad \theta(\infty) = 0, \quad \chi(\infty) = 0 : \eta \rightarrow \infty., \end{aligned} \right\} \quad (2.3.7)$$

The above equations are solved with the help of well-known mathematical computing software maple implementing Runge Kutta Fehlberg 4th 5th order by setting the values of the constraints $\phi = 0.01, K = 0.5, Q = 0.5, Sc = 0.8, Rc = \delta = 0.5, S = 1, E = 0.5, n = 0.1, \gamma = 1$ and taking 0.1 as step size with tolerance error about 10^{-8} .

2.4 Deliberation of Results:

The current study explores the laminar continuous flow of incompressible nanofluid across an ESS in the existence of a porous medium. Heat source/ sink, activation energy, and Newtonian heating are also considered. In the present examination, the modelled problem is reduced to dimensionless form by using appropriate set of similarity variables. During this process some substantial parameters have been encountered and the effect of these pertinent parameters on involved profiles are conferred graphically and explained in brief. The three-dimensional (3D) graphs show the difference in friction factor, mass and heat conveyance rates for several values of different parameters. Table 2.1 and Table 2.2 represents the numerical validation for $f''(0)$ and $-\theta'(0)$ values of present work with published paper and attained a good agreement with each other

Fig.2.2 shows the impact of K on f' . Increase in values of K decays the f' . As the porosity component value rises, the system's resistance rises as well. Fluid flow is decreased as a result of the higher frictional force. In this situation, increased porosity improves the surface's resistance to liquid movement. The extra resistance causes the liquid's velocity to slow down. The impact of S on f' is exposed in Fig. 2.3. Upsurge in values of S drops the f' . Fig. 2.4 displays the impact of Q on θ for both CWT and NH cases. Escalation in values of Q drops the θ . Further, rate of declination is faster for NH case than CWT case. It's worth noting that when Q becomes higher, the thermal distribution decays. The rise

in Q values declines the specific heat capacitance which results in thermal gradient decay.

The influence of Sc on χ is revealed in Fig.2.5. Gain in values of Sc declines the χ . The smallest Sc denotes the nanoparticles' greatest concentration. As Sc rises, momentum diffusivity increases, causing mass transport to degrade. The diffusion coefficient decreases as Sc increases, which drops down the mass transfer. Fig.2.6 shows the impact of Rc on χ . Rise in values of Rc declines the χ . A greater chemical reaction has a negative effect that degrades the reactant species. Due to this, the concentration gradient is reduced when Rc is increased. The influence of E on χ is revealed in Fig. 2.7. Gain in values of E improves the χ . Low temperature and low activation energy slow down the reaction rate, causing chemical reaction processes to decay. The Arrhenius equation explains that the injection of activation energy into any system can clearly demonstrating that the decrease in heat and acceleration leads in a low reaction rate constant. As a result, the generative chemical process is stimulated causing the concentration of nanoparticles to rise. As a result, the χ rises.

Fig.2.8 shows the impact of δ on χ . Rise in values of δ declines the χ . Physically, it shows that as the temperature difference increases, the thickness of the concentration boundary decreases. Fig.2.9 shows the impact of n on χ . Rise in values of n declines the χ . Chemically, when the value of n increases, damaging chemical processes increase owing to the decrease in fluid concentration. Fig.2.10 displays the effect of ϕ over f' . The f' decays with increase in the values of ϕ . Addition of solid volume fraction ϕ improves the thickness of the boundary layer. As a result, the fluid will flow slowly, reduces $f'(\eta)$ The change in ϕ on θ is presented through Fig.2.11. The thermal distribution enhances with increase in ϕ . Due to the increased thickness of the boundary layer caused by the accumulation of solid nanoparticles to the base fluid, the thermal distribution will progressively improve and

heat will be rapidly transferred between the particles. The Impact of ϕ on χ is showed in Fig.2.12. Here inclined values of ϕ will decline the mass transfer.

The 3D view in Fig.2.13 represents the impact of K and S on skin friction coefficient. Here, the growing values of both K and S improves the skin friction coefficient. The 3D view in Fig.2.14 represents the impact of Rc and E on Sherwood number. Here, the growing values of E advances the Sherwood number but reverse behaviour is seen for upward values of Rc . The 3D view in Fig.2.15 displays the impact of Q and ϕ on Nusselt number for both CWT and NH cases. Upsurge in values of Q and ϕ drops down the Nusselt number for both CWT and NH cases. Further, the fluid shows improved rate of heat transfer for CWT case than NH case. Table 2.3 represents the Computational values of $-f''(0)$, $-\theta'(0)$ and $-\chi'(0)$ for the impact of varied dimensionless parameters. Here, escalation in values of K and Q decays the $-f''(0)$, $-\theta'(0)$ and $-\chi'(0)$.

2.5 Inference

Many engineering processes and industries rely on research on boundary layer flow and heat transfer caused by a stretching surface. In the engineering process, it was shown that the rate of heat transfer affected the quality of the finished product. In this article, we have considerably explained the influence of heat sink/source on the stream of nanofluid over an ESS. Further, Activation energy, porous medium and NH are accounted here. The behaviour of concentration, thermal and velocity fields is analysed graphically. The main conclusions drawn from the current study are:

- Escalation in values of K deteriorates the f' due to the higher frictional force.
- Upsurge in values of S deteriorates the f' .

- Escalation in values of Q declines specific heat capacitance which drops down the θ . Further, rate of declination is faster for NH case than CWT case.
- Increase in values of Sc and Rc declines the χ due to increased momentum diffusivity and decreased the reactant species concentration. But inverse behaviour is seen for rise in values of E which reasons for higher particle concentration.
- The thermal distribution enhances with increase in ϕ but inverse behaviour is seen in velocity and mass transfer for improved volume fraction
- The growing values of both K and S improves the skin friction coefficient.
- Boom in values of Q and ϕ declines the Nusselt number for both CWT and NH cases. Further, the fluid shows improved rate of heat transfer for CWT case than NH case.
- The growing values of E advances the Sherwood number but reverse behaviour is noticed for upward values of Rc.

Table 2.1: Numerical Validation for $f''(0)$ in the absence of K , ϕ and $S = 0$

Khan et al. [50] (VIPM)	Kameswaran et al. [51] (RKF)	Present Results (RKF-45)
-1.28138	-1.281809	-1.28185

Table 2.2: Numerical Validation for $-\theta'(0)$ for some reduced cases

Pr	1	2	3	5	10
Magyari and Keller [52]	0.954782	–	1.869075	2.500135	3.660379
El-Aziz [53]	0.954785	–	1.869074	2.500132	3.660372
Bidin and Nazar [54]	0.9548	1.4714	1.8691	–	–
Ishak [55]	0.9548	1.4715	1.8691	2.5001	3.6604
Mukhopadhyay and Gorla [56]	0.9547	1.4714	1.8691	2.5001	3.6603
Present results	0.954955	1.4714207	1.8690440	2.5001089	3.6603543

Table 2.3: Computational Values of $-f''(0)$, $-\theta'(0)$ and $-\chi'(0)$ for dimensionless parameters

K	Q	Rc	Sc	δ	E	ϕ	S	γ	$-f''(0)$	$-\theta'(0)$ CWT	$-\theta'(0)$ NH	$-\chi'(0)$
0.1									1.896330	6.591028	1.176764	1.410030
0.5	0.5	0.5	0.8	0.5	0.5	0.01	1	1	2.036445	6.570183	1.177576	1.392574
0.8									2.133098	6.555946	1.178117	1.381175
	-0.5								2.133098	7.989216	1.142239	1.380078
	0.5								2.133098	6.555946	1.177576	1.381175
		0.2							2.133098	6.555946	1.177576	1.341804
		0.5							2.133098	6.555946	1.177576	1.381175
		0.8							2.133098	6.555946	1.177576	1.418859
			0.8						2.133098	6.555946	1.177576	1.418859
			1.2						2.133098	6.555946	1.177576	1.932014
			1.5						2.133098	6.555946	1.177576	2.324893
				0.3					2.133098	6.555946	1.177576	1.378118
				0.5					2.133098	6.555946	1.177576	1.381175
				0.7					2.133098	6.555946	1.177576	1.384064
					0.5				2.133098	6.555946	1.177576	1.471369
					1				2.133098	6.555946	1.177576	1.417347
					1.5				2.133098	6.555946	1.177576	1.381175
						0			2.125178	6.792146	1.172232	1.443147
						0.01			2.036445	6.570183	1.177576	1.392574
						0.03			2.144823	6.882691	1.195281	1.530318
							0.5		1.830860	3.654842	1.357900	1.203891
							0.8		2.007414	5.393092	1.222964	1.359580
							1		2.133098	6.555946	1.177576	1.381175
							0		1.610954	-	0.00000	2.119209
							1		1.610954	-	1.177576	2.121214
							2		1.610954	-	2.863676	2.123880

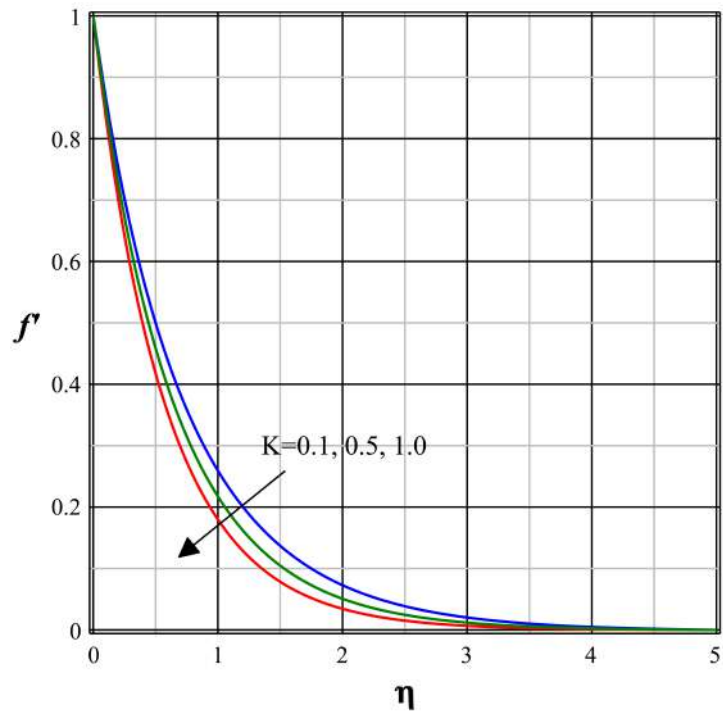


Figure 2.2: Impact of K on f'

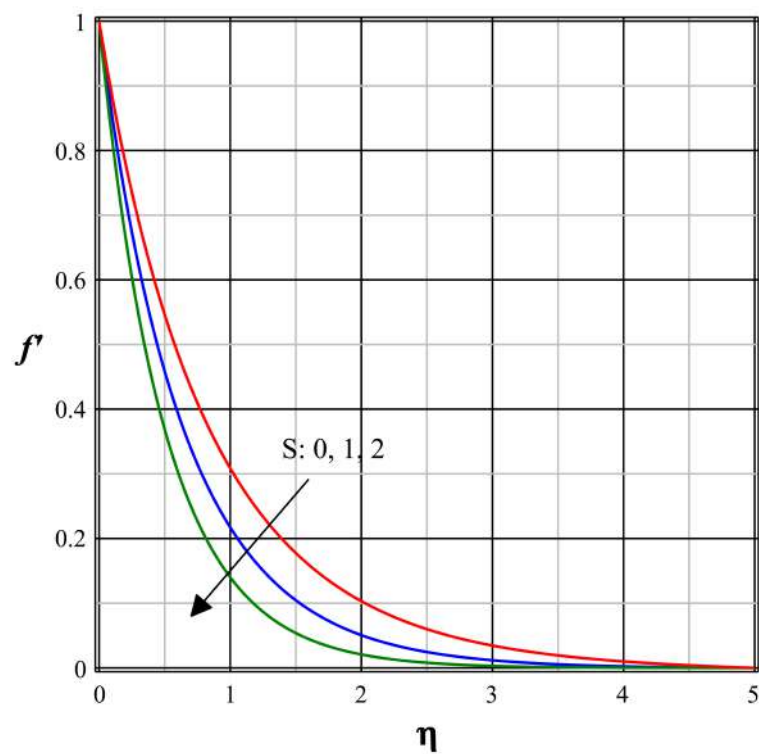


Figure 2.3: Impact of S on f'

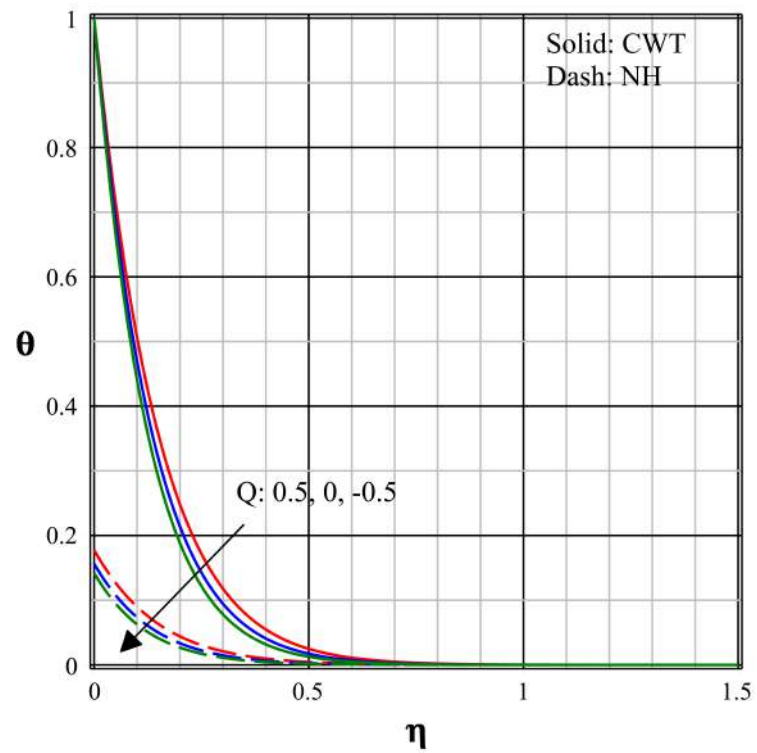


Figure 2.4: Impact of Q on θ

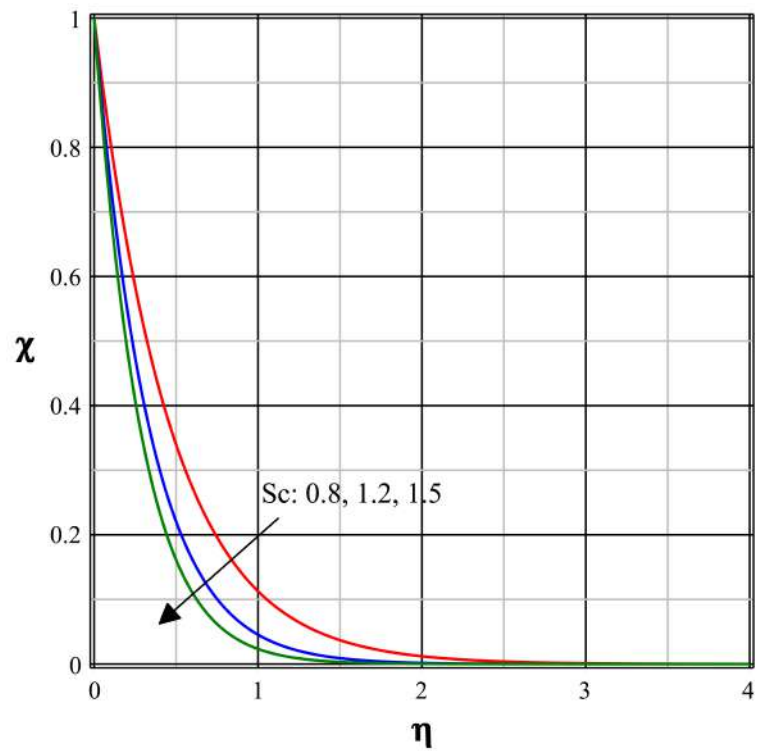


Figure 2.5: Impact of Sc on χ .

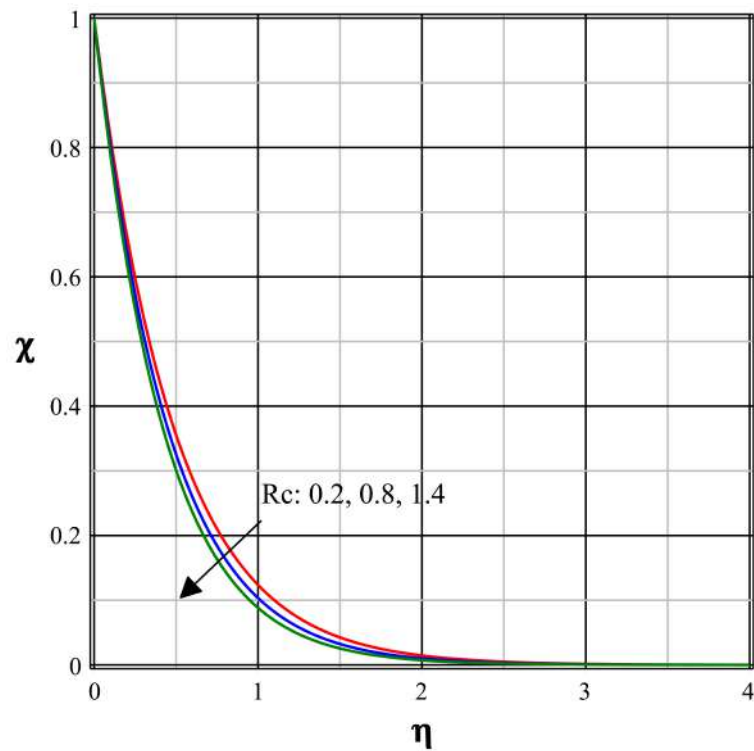


Figure 2.6: Impact of Rc on χ .

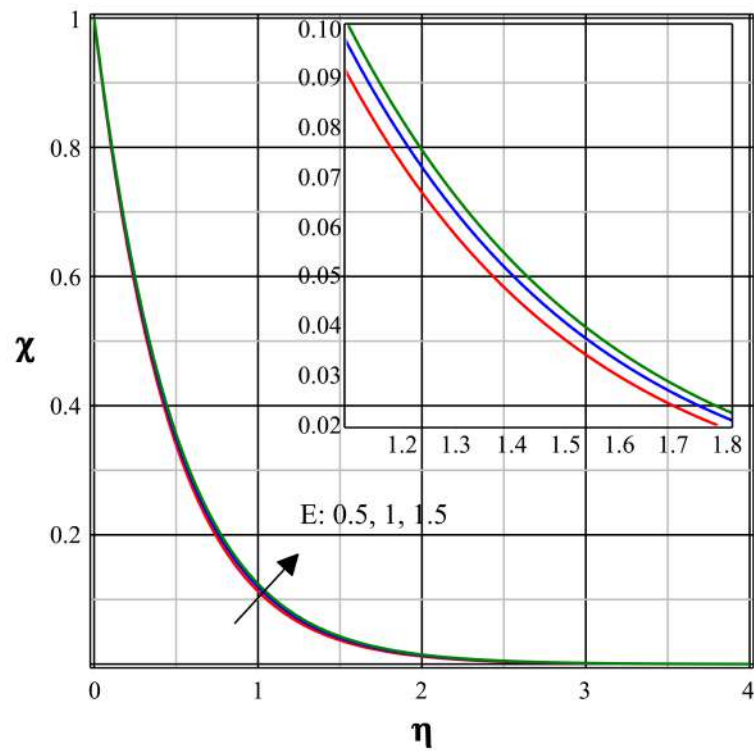


Figure 2.7: Impact of E on χ .

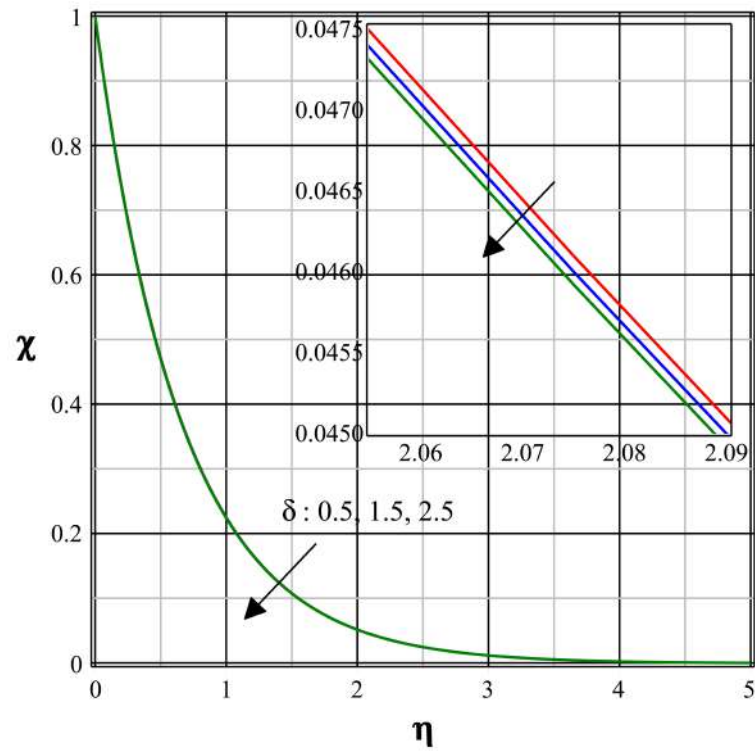


Figure 2.8: Impact of δ on χ .

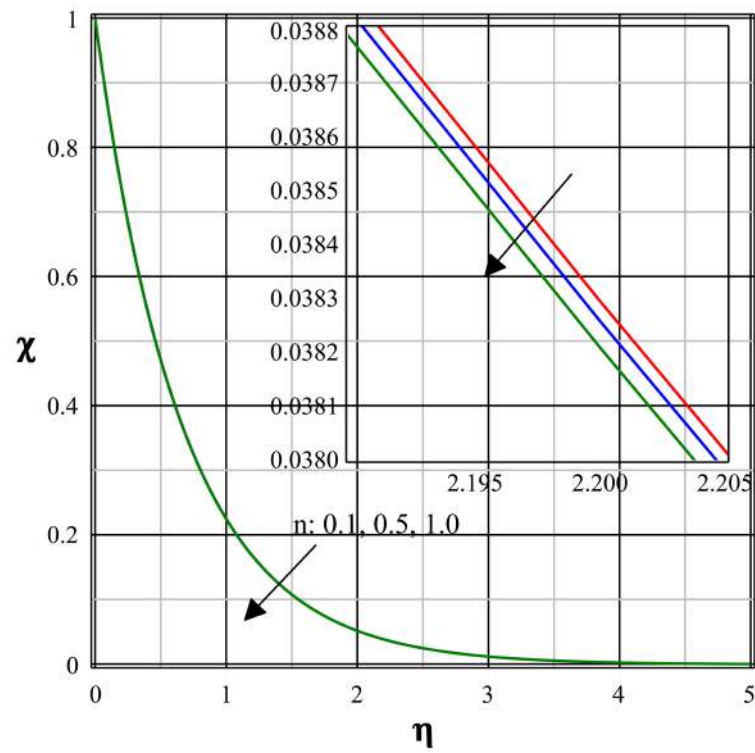


Figure 2.9: Impact of n on χ .

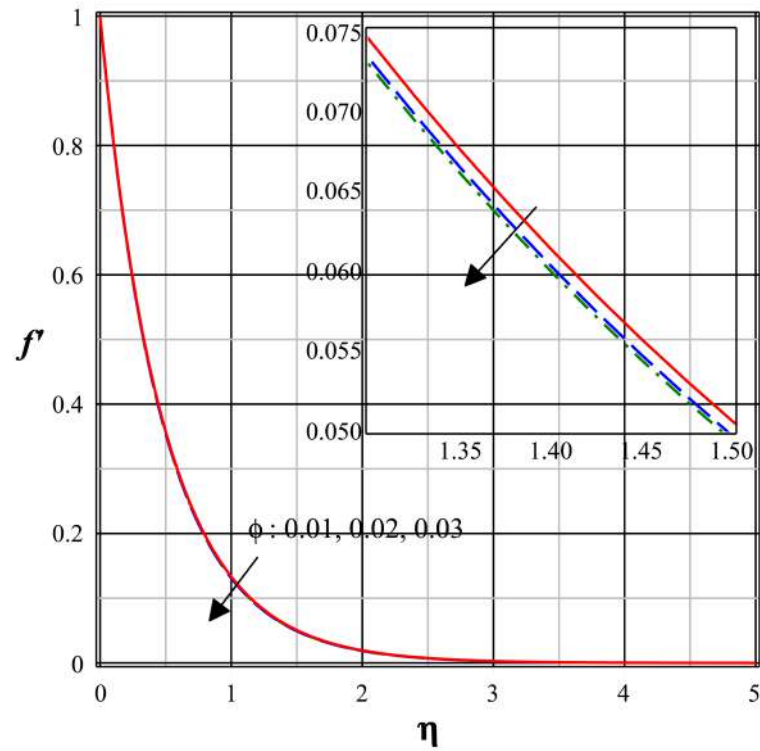


Figure 2.10: Impact of ϕ on f'

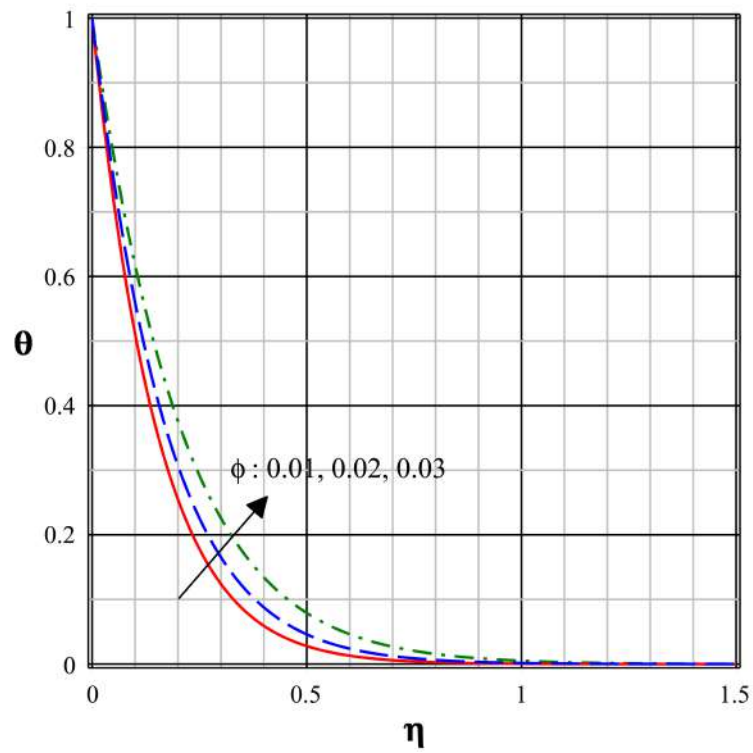


Figure 2.11: Impact of ϕ on θ

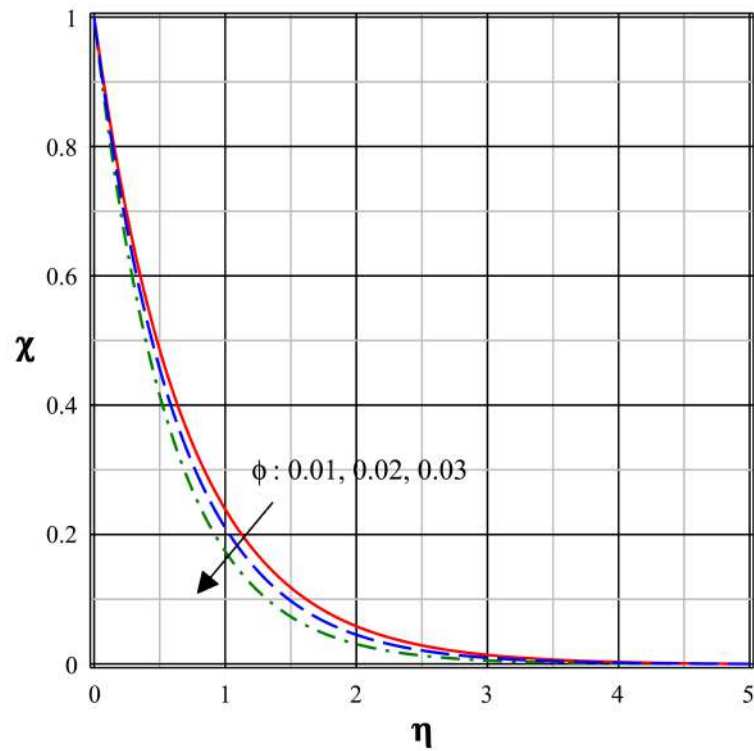


Figure 2.12: Impact of ϕ on χ .

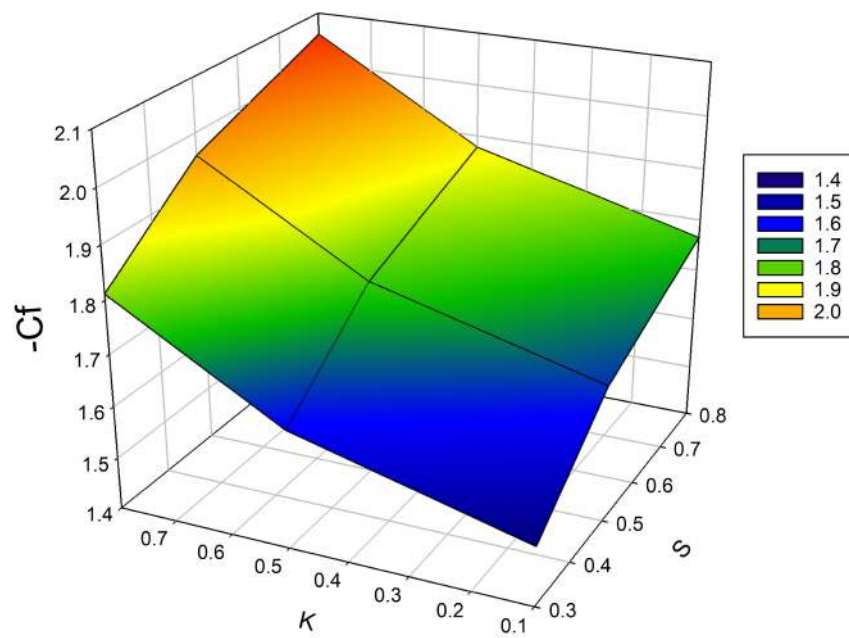


Figure 2.13: Impact of K and S on skin friction coefficient

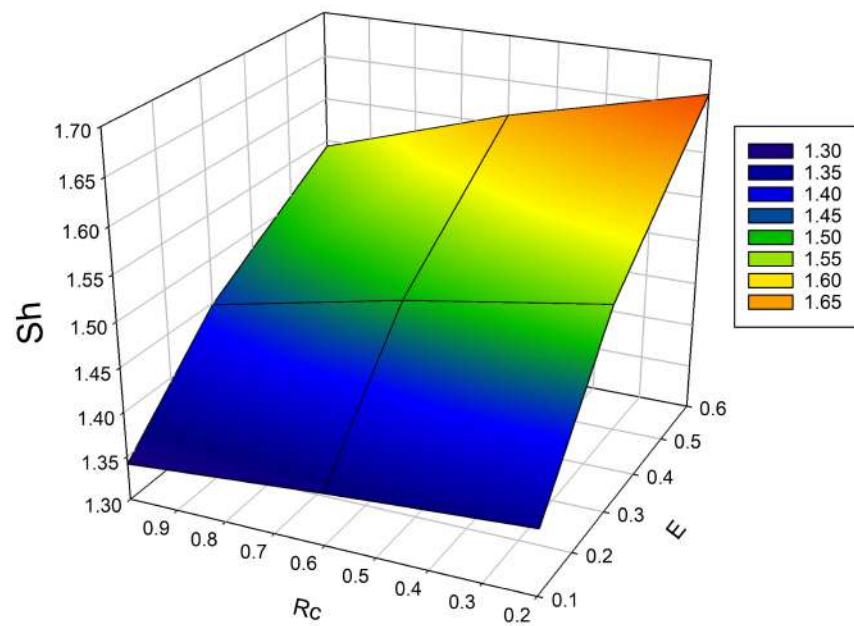


Figure 2.14: Impact of Rc and E on Sherwood number.

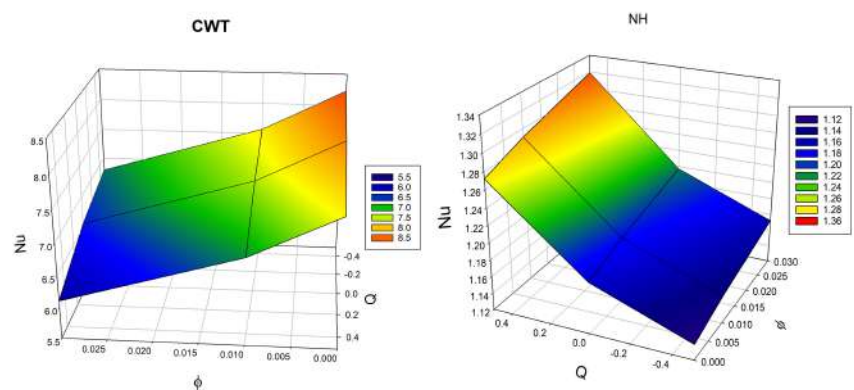


Figure 2.15: impact of Q and ϕ on Nusselt number for CWT case and (b) Impact of Q and ϕ on Nusselt number for NH case.

Chapter 3

The impact of Cattaneo-Christov double diffusion on Oldroyd-B fluid flow over a stretching sheet with thermophoretic particle deposition and relaxation chemical reaction

3.1 Prelude:

The present chapter emphasizes on the properties of flow, heat, and mass transport in relation to their applications. The use of non-Newtonian fluids in biological and technological areas has sparked a lot of curiosity in recent years. Having such potential interests, our objective is to investigate the flow of Oldroyd-B fluid (OBF) on a stretching sheet using Cattaneo-Christove double diffusion and a heat source/sink (HSS). In addition, the modelling takes into account of relaxation chemical reactions and thermophoretic particle deposition (TPD). By selecting relevant similarity variables, the equations that represent the suggested flow are transformed to ordinary differential equations (ODEs). The RK45 and a shooting system are used to solve the reduced equations. The findings show that, when the rotation parameter is increased, the fluid velocity decreases. The thermal and concentration profiles are reduced when the values of relaxation times parameters of temperature and concentration increase.

3.2 Mathematical Elucidation:

Consider a three-dimensional incompressible steady OBF flow caused through the linearly stretching sheet with $U_w(x) = ax$. The fluid flow is considered in the domain $z > 0$ and surface is associated in xy -plane. With constant angular velocity Ω , the fluid is rotating about the z -axis as shown in Fig.3.1. The mass and heat transfer components are inspected in the existence of concentration and thermal diffusions with the relaxation of mass and heat fluxes, respectively. In the presence of heat production or absorption, boundary layer flow is also taken into account. Considering the above assumptions, the governing equations of the flow model can be written as follow (see refs. [57], [58] and [59]):

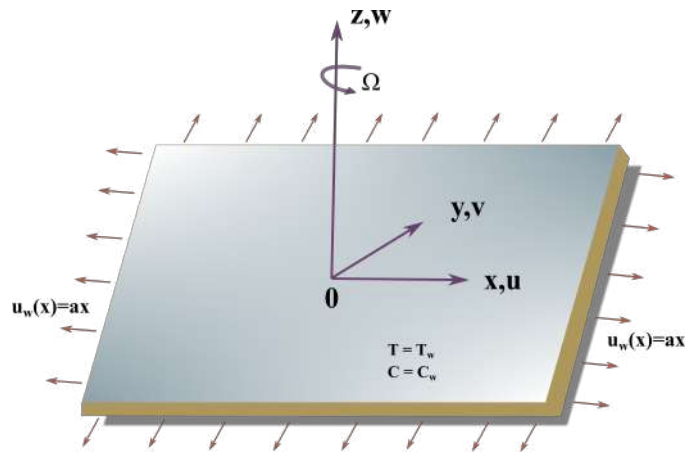


Figure 3.1: Flow Geometry

$$\frac{\partial u}{\partial x} + \frac{\partial v}{\partial y} + \frac{\partial w}{\partial z} = 0, \quad (3.2.1)$$

$$\begin{aligned} & u \frac{\partial u}{\partial x} + v \frac{\partial u}{\partial y} + w \frac{\partial u}{\partial z} + \lambda_1 \left(u^2 \frac{\partial^2 u}{\partial x^2} + v^2 \frac{\partial^2 u}{\partial y^2} + w^2 \frac{\partial^2 u}{\partial z^2} + 2uv \frac{\partial^2 u}{\partial x \partial y} + 2vw \frac{\partial^2 u}{\partial z \partial y} \right) \\ & + \lambda_1 \left(2uw \frac{\partial^2 u}{\partial x \partial z} - 2\Omega \left(u \frac{\partial v}{\partial x} + v \frac{\partial v}{\partial y} + w \frac{\partial v}{\partial z} \right) + 2\Omega \left(v \frac{\partial u}{\partial x} - u \frac{\partial u}{\partial y} \right) \right) \\ & - 2\Omega v = \nu \left(\frac{\partial^2 u}{\partial z^2} \right) + \nu \lambda_2 \left[u \frac{\partial^3 u}{\partial x \partial z^2} + v \frac{\partial^3 u}{\partial y \partial z^2} + w \frac{\partial^3 u}{\partial z^3} - \frac{\partial u}{\partial x} \frac{\partial^2 u}{\partial z^2} \right] \\ & + \nu \lambda_2 \left[-\frac{\partial u}{\partial y} \frac{\partial^2 v}{\partial z^2} - \frac{\partial u}{\partial z} \frac{\partial^2 w}{\partial z^2} \right], \end{aligned} \quad (3.2.2)$$

$$\begin{aligned} & u \frac{\partial v}{\partial x} + v \frac{\partial v}{\partial y} + w \frac{\partial v}{\partial z} + \lambda_1 \left(u^2 \frac{\partial^2 v}{\partial x^2} + v^2 \frac{\partial^2 v}{\partial y^2} + w^2 \frac{\partial^2 v}{\partial z^2} + 2uv \frac{\partial^2 v}{\partial x \partial y} + 2vw \frac{\partial^2 v}{\partial z \partial y} \right) \\ & + \lambda_1 \left(2uw \frac{\partial^2 v}{\partial x \partial z} + 2\Omega \left(u \frac{\partial u}{\partial x} + v \frac{\partial u}{\partial y} + w \frac{\partial u}{\partial z} \right) + 2\Omega \left(v \frac{\partial v}{\partial x} - u \frac{\partial v}{\partial y} \right) \right) \\ & + 2\Omega u = \nu \left(\frac{\partial^2 v}{\partial z^2} \right) + \nu \lambda_2 \left[u \frac{\partial^3 v}{\partial x \partial z^2} + v \frac{\partial^3 v}{\partial y \partial z^2} + w \frac{\partial^3 v}{\partial z^3} - \frac{\partial v}{\partial x} \frac{\partial^2 u}{\partial z^2} - \frac{\partial v}{\partial y} \frac{\partial^2 v}{\partial z^2} \right] \\ & + \nu \lambda_2 \left[-\frac{\partial v}{\partial z} \frac{\partial^2 w}{\partial z^2} \right] \end{aligned} \quad (3.2.3)$$

$$u \frac{\partial T}{\partial x} + v \frac{\partial T}{\partial y} + w \frac{\partial T}{\partial z} + \Omega_e \Gamma_e = \frac{k}{(\rho C_p)} \left(\frac{\partial^2 T}{\partial z^2} \right) + \frac{\widehat{Q}}{(\rho C_p)} (T - T_\infty) \quad (3.2.4)$$

$$\begin{aligned} & u \frac{\partial C}{\partial x} + v \frac{\partial C}{\partial y} + w \frac{\partial C}{\partial z} + \Omega_c \Gamma_c = D \left(\frac{\partial^2 C}{\partial z^2} \right) - \frac{\partial (V_T (C - C_\infty))}{\partial z} \\ & + k_r \left[\Gamma_c \left(u \frac{\partial C}{\partial x} + v \frac{\partial C}{\partial y} + w \frac{\partial C}{\partial z} \right) + (C - C_\infty) \right], \end{aligned} \quad (3.2.5)$$

where,

$$\begin{aligned}\Omega_e = & u^2 \frac{\partial^2 T}{\partial x^2} + v^2 \frac{\partial^2 T}{\partial y^2} + w^2 \frac{\partial^2 T}{\partial z^2} + 2uv \frac{\partial^2 T}{\partial x \partial y} + 2vw \frac{\partial^2 T}{\partial z \partial y} + 2uw \frac{\partial^2 T}{\partial z \partial x} \\ & + \left(u \frac{\partial u}{\partial x} + v \frac{\partial u}{\partial y} + w \frac{\partial u}{\partial z} \right) \frac{\partial T}{\partial x} + \left(u \frac{\partial v}{\partial x} + v \frac{\partial v}{\partial y} + w \frac{\partial v}{\partial z} \right) \frac{\partial T}{\partial y} \\ & + \left(u \frac{\partial w}{\partial x} + v \frac{\partial w}{\partial y} + w \frac{\partial w}{\partial z} \right) \frac{\partial T}{\partial z},\end{aligned}\quad (3.2.6)$$

$$\begin{aligned}\Omega_c = & u^2 \frac{\partial^2 C}{\partial x^2} + v^2 \frac{\partial^2 C}{\partial y^2} + w^2 \frac{\partial^2 C}{\partial z^2} + 2uv \frac{\partial^2 C}{\partial x \partial y} + 2vw \frac{\partial^2 C}{\partial z \partial y} + 2uw \frac{\partial^2 C}{\partial z \partial x} \\ & + \left(u \frac{\partial u}{\partial x} + v \frac{\partial u}{\partial y} + w \frac{\partial u}{\partial z} \right) \frac{\partial C}{\partial x} + \left(u \frac{\partial v}{\partial x} + v \frac{\partial v}{\partial y} + w \frac{\partial v}{\partial z} \right) \frac{\partial C}{\partial y} \\ & + \left(u \frac{\partial w}{\partial x} + v \frac{\partial w}{\partial y} + w \frac{\partial w}{\partial z} \right) \frac{\partial C}{\partial z},\end{aligned}\quad (3.2.7)$$

The thermophoretic velocity V_T can be defined in the form (ref. [60]):

$$V_T = -\frac{k^* \nu}{T_r} \frac{\partial T}{\partial Z} \quad (3.2.8)$$

where the k^* for which their values are from 0.2 to 1.2 as specified by Batchelor and Shen [61] and k^* is well-defined from the Talbot et al [62] is given by

$$k^* = \frac{2C_s \left(\frac{\lambda_g}{\lambda_p} + C_t \text{Kn} \right) \left[1 + \text{Kn} \left(C_1 + C_2 e^{-\frac{C_3}{\text{Kn}}} \right) \right]}{(1 + 3C_m \text{Kn}) \left(1 + \frac{\lambda_g}{\lambda_p} + 2C_t \text{Kn} \right)}, \quad (3.2.9)$$

where, the thermal conductivities of fluid and diffused particles are represented by λ_g and λ_p respectively and $C_t = 2.20$, $C_s = 1.147$, $C_m = 1.146$, $C_1 = 1.2$, $C_2 = 0.41$ & $C_3 = 0.88$.

The flow is subjected to the related boundary constraints (refs. [57-59]):

$$\left. \begin{aligned} Z = 0 : & u = U_w(x) = ax, v = 0, w = 0, T = T_w, C = C_w, \\ \\ Z \rightarrow \infty : & u \rightarrow 0, v \rightarrow 0, T \rightarrow T_\infty, C \rightarrow C_\infty \end{aligned} \right\} \quad (3.2.10)$$

Considering the following suitable transformations, the governing equations can be simplified into the dimensionless form :

$$u = axf'(\eta), v = axg(\eta), w = -f(\eta)\sqrt{a\nu}, \eta = \sqrt{\frac{a}{\nu}}z, \theta(\eta) = \frac{T - T_\infty}{T_w - T_\infty}, \chi(\eta) = \frac{C - C_\infty}{C_w - C_\infty}.$$

(3.2.11)

Using above similarity transformations, the continuity 3.2.1 is satisfied identically. Further, the remaining Eqs. 3.2.2 –3.2.5 are reduced to the following boundary value problems:

$$f''' + ff'' - f'^2 + 2\lambda g - 2\lambda\beta_1 fg' - \beta_1 (f^2 f''' - 2ff'f'') + \beta_2 (-ff^{iv} + f''^2) = 0, \quad (3.2.12)$$

$$g'' + fg' - f'g - 2\lambda [f' + \beta_1 (f'^2 - ff'' + g^2)] + \beta_1 (2ff'g' - f^2g'') + \beta_2 (f'g'' + f''g' - fg''' - gf''') = 0, \quad (3.2.13)$$

$$\theta'' + Pr f\theta' - Pr \lambda_E (ff'\theta' + f^2\theta'') + Pr Q\theta = 0, \quad (3.2.14)$$

$$\chi'' + Scf\chi' - \lambda_C Sc (ff'\chi' + f^2\chi'') + Sc\sigma\chi - Sc\sigma\lambda_C f\chi' + ScN_t(\chi\theta'' + x'\theta') = 0 \quad (3.2.15)$$

The corresponding boundary conditions are transformed as:

$$\left. \begin{aligned} \eta = 0 : f = 0, f' = 1, g = 0, \theta = 1, \chi = 1, \\ \eta \rightarrow \infty : f' \rightarrow 0, g \rightarrow 0, f'' \rightarrow 0, \theta \rightarrow 0, \chi \rightarrow 0, \end{aligned} \right\} \quad (3.2.16)$$

where, $\lambda = \frac{\Omega}{a}$, $\beta_1 = \lambda_1 a$, $\beta_2 = \lambda_2 a$, $Q = \frac{\hat{Q}}{\sigma} C_p$, $\lambda_E = a\Gamma_e$, $\lambda_C = a\Gamma_c$, $Sc = \frac{\nu}{D}$, $Pr = \frac{\nu}{\alpha}$, $N_t^* = \frac{k^*(T_w - T_\infty)}{T_r}$, $\sigma = \frac{k_r}{a}$.

3.3 Method of Numerical Extraction:

It does not seem that achieving the numerical solution of the existing model, which is very non-linear in nature is feasible. As a result, we use an efficient traditional $RKF - 45$ approach combined with shooting methodology to analyse the flow model for the aforementioned coupled $ODEs$ 3.2.12 - 3.2.15 as well as the boundary conditions equation 3.2.16 for various values of the governing parameters. It's vital to memo that, the convergence is not guaranteed, specifically if missing beginning values are incorrectly predicted. When one of the domain end points is at infinity, another conflict occurs due to the instability of boundary value problems. As a result, the most important step in this strategy is to choose the appropriate finite value of η_∞ . We hand-picked an appropriate finite value of η_∞ to satisfy the far field boundary conditions asymptotically. Once convergence is achieved, we use the $RKF - 45$ method to integrate the resulting ordinary differential equations with the supplied set of parameters to find the desired solution. Finally, in order to meet the convergence condition, the procedure is repeated until the findings are accurate to the specified degree of precision of 10^{-6} level. The step size is selected as $\Delta\eta = 0.0001$ along with the comparative error tolerance to 10^{-6} is well-organized for convergence criteria. The results for the $-f''(0)$ and $-\theta'(0)$ are compared to the existing publications to verify the present technique (see Table 3.1 and Table 3.2.)

3.4 Deliberation of Results:

The graphical effects of the physical dimensionless quantities on involved profiles are discussed in this section. The equations that reflect the stated flow are changed to ODEs by picking apt similarity variables. A numerical scheme ($RKF - 45$) with a shooting

Table 3.1: **An assessment $-f''(0)$ for some reduced cases.**

β_1	0	0.2	0.4	0.6	0.8	1.2
Abel et al. [63]	0.999996	1.051948	1.101850	1.150163	1.196692	1.285257
Megahed [64]	0.999978	1.051945	1.101848	1.150160	1.196690	1.285253
Sadeghy et al. [65]	1.00000	1.05490	1.10084	1.15016	1.19872	-----
Mustafa et al. [66]	1.000000	1.051890	1.101903	1.150137	1.196711	1.285363
Khan et al. [58]	1.000000	1.051889	1.101903	1.150137	1.196711	1.285363
Present results	1.000000	1.051890	1.101903	1.150137	1.196711	1.285363

Table 3.2: **An assessment $-\theta'(0)$ for some reduced cases.**

Pr.	0.7	2.0	7.0
Khan and Pop [67]	0.4539	0.9113	1.8954
Wang [68]	0.4539	0.9114	1.8954
Gorla and Sidawi [69]	0.4539	0.9114	1.8954
Khan et al. [58]	0.454374	0.911155	1.822020
Present results	0.454369	0.911148	1.822015

scheme is used to clearly understand the behaviour of flow profiles, which are strategized and debated using graphs. Fig.3.2 shows the influence of λ on $f'(\eta)$. The rise in values of λ decays the $f'(\eta)$. Fig.3.3 shows the impact of λ on $g(\eta)$. The upsurge in values of λ drops the $g(\eta)$. In physical terms, the λ is the ratio of stretching rate and rotation rate. The velocity in the x-direction seen to decrease when the Ω around the z-axis increases as the λ values are increased. Due to this, both $f'(\eta)$ and $g(\eta)$ decreases. The impact of β_1 on $f'(\eta)$ is shown in Fig.3.4. The upward β_1 values drops the $f'(\eta)$. Physically, β_1 depends on the λ_1 . So, with the escalation in β_1 also augments λ_1 which offers extra resistance to the fluid motion which upsurses the $f'(\eta)$. The influence of β_2 on $f'(\eta)$ is shown in Fig.3.5. The increasing values of β_2 improves the $f'(\eta)$. Physically, β_2 depends on the λ_2 . So, with the rise in β_2 also augments λ_2 which offers supplementary struggle

to the fluid motion which upsurges the $f'(\eta)$.

The consequence of Q on $\theta(\eta)$ is shown in Fig.3.6. The escalating values of Q improve the $\theta(\eta)$. Growth in the Q thickens the layer related to $\theta(\eta)$. The existence of the heat source restrictions in the flow state provides more excellent heat in this case. The presence of a heat source energizes the fluid. Consequently, as heat is consumed, the buoyancy force accelerates the flow and improves the heat transfer. Fig.3.7 shows the effect of λ_E on $\theta(\eta)$. The rising values of λ_E drops down the $\theta(\eta)$. Physically, we may state that with higher values of the λ_E , the system exhibits a nonconducting characteristic that results in a narrowing of the thermal distribution. Furthermore when $\lambda_E = 0$, the temperature distribution in Fourier's law is more significant than in the Cattaneo-Christov heat flow model.

Fig.3.8 displays the impact of Sc on $\chi(\eta)$. The increase in values of Sc drops the $\chi(\eta)$. The smallest Sc correlates to the highest concentration of nanoparticles. For an upsurge in the Sc , there is a decay in the concentration field owing to mass diffusion. The effect of λ_C on $\chi(\eta)$ is shown in Fig.3.9. The escalating values of λ_C declines the $\chi(\eta)$. In reality, a greater λ_C generates a weaker mass diffusivity, resulting in a narrower concentration distribution. A lower concentration field is produced by a higher value of λ_C . The effect of σ on $\chi(\eta)$ is shown in Fig.3.10. The rising values of σ declines the $\chi(\eta)$. The fact that strong chemical reactions ($\sigma > 0$) have a tendency to reduce diffusion, which is consequential in a decrease in chemical molecular diffusivity of the species concentration. Due to this retarded concentration of species, the $\chi(\eta)$ is decreased. Fig.3.11 portrays the impact of N_t^* on $\chi(\eta)$. The growing values of N_t^* upsurges the $\chi(\eta)$. When the thermophoresis parameter is superior then the thermophoretic force increases, which pushes more particles nearer to the surface for a greater temperature differential,

the concentration profiles on the cold surface are reduced as temperature ratios are raised.

Table 3.3 portrays the numerical values of f'' with respect to pertinent varied parameters. The upsurge in values of λ and β_2 drops the f'' but the contrary tendency is detected for upward β_1 values. The numerical values of θ' with respect to pertinent varied parameters are shown in Table 3.4. The escalation in values of λ and β_2 declines the θ' but the inverse trend is detected for upward values of Q , β_1 and λ_E . The numerical values of χ' with respect to pertinent varied parameters is presented in Table 3.5. The escalation in Sc , σ and N_t^* values declines the χ' but the reverse trend is detected for upward values of λ_C .

3.5 Inference:

The OBF flow analysis, in combination with mass and heat transfer initiated by a stretching sheet is utilized in the polymer industry and numerous industrial activities such as glass blowing and metallic sheet cooling. In context to these applications, the current research explores the flow of Oldroyd-B fluid on a stretching sheet by considering Cattaneo-Christov double diffusion and heat source/sink. TPD is also considered in the modelling and it is one of the most fundamental mechanisms for carrying microscopic particles over a thermal gradient, and it is crucial in electronics and aeronautics. The equations that represent the indicated flow are changed to ODEs by electing relevant similarity variables. The ODEs are then solved using RKF-45 and shooting schemes. The behaviour of dimensionless parameters on dimensionless velocity, concentration, and temperature profiles are analyzed graphically. The following are the key findings of the present study:

- The rise in values of λ declines the $f'(\eta)$ and $g(\eta)$

- The increasing values of β_1 declines the $f'(\eta)$ but converse trend is seen for enhanced β_2 values.
- The rising values of Q improve the $\theta(\eta)$.
- The rising values of λ_E drops down the $\theta(\eta)$.
- The escalating values of λ_C and Sc declines the $\chi(\eta)$.
- The increasing values of σ declines the $\chi(\eta)$ but reverse trend is seen for enhanced N_t^* values.
- The rise in values of λ and β_2 declines the θ' but the opposite trend is detected for upward values of Q , β_1 and λ_E .
- The growth in values of Sc , σ and N_t^* declines the χ' but the conflicting trend is detected for upward values of λ_C .

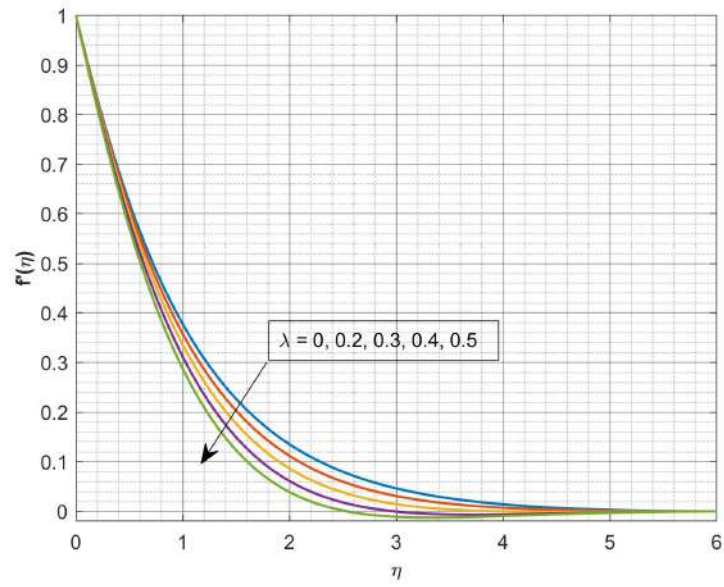


Figure 3.2: Influence of λ on $f'(\eta)$.

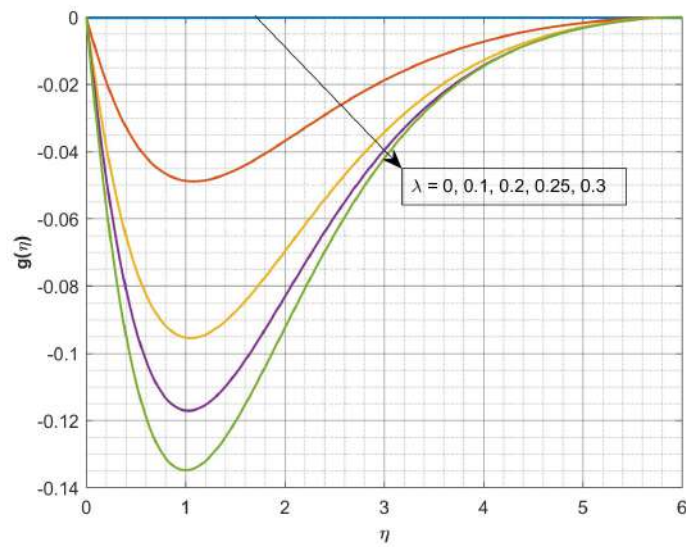


Figure 3.3: Influence of λ on $g(\eta)$.

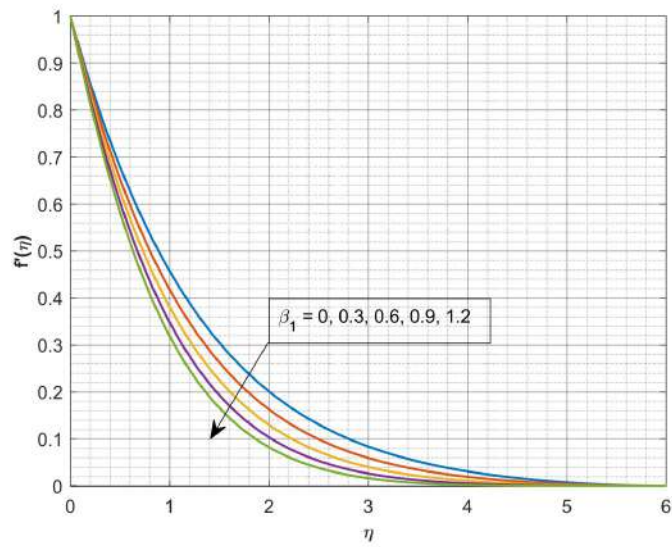


Figure 3.4: Influence of β_1 on $f'(\eta)$.

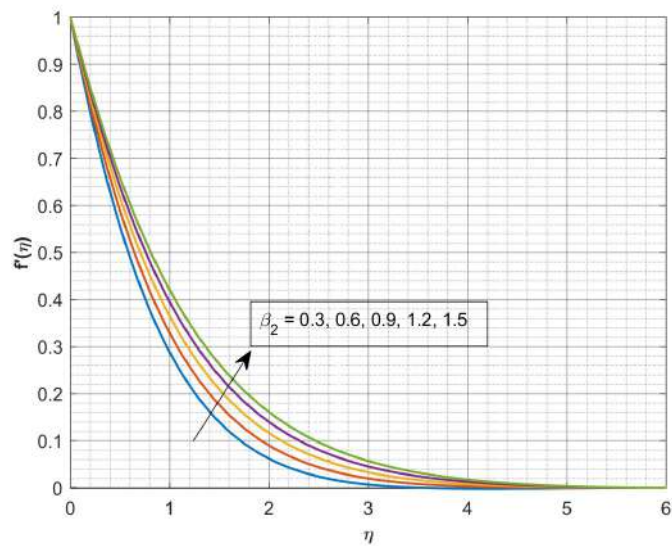


Figure 3.5: Influence of β_2 on $f'(\eta)$.

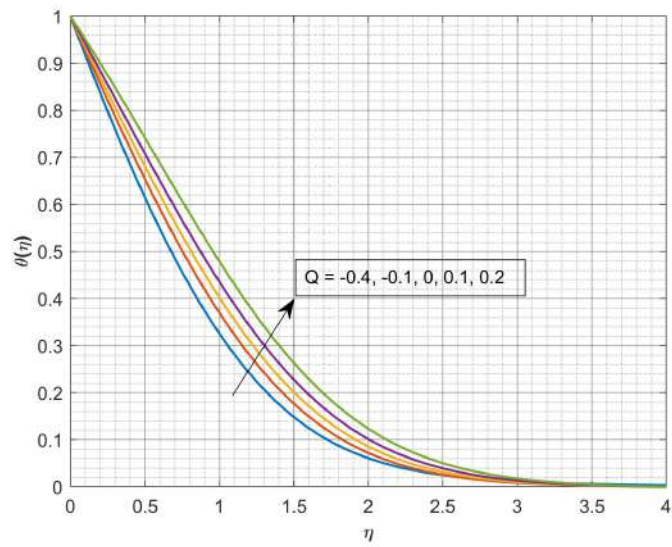


Figure 3.6: Influence of Q on $\theta(\eta)$.

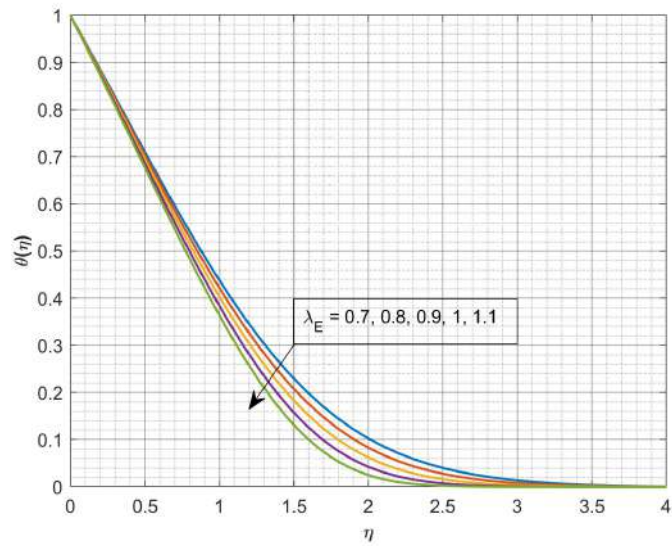


Figure 3.7: Influence of λ_E on $\theta(\eta)$

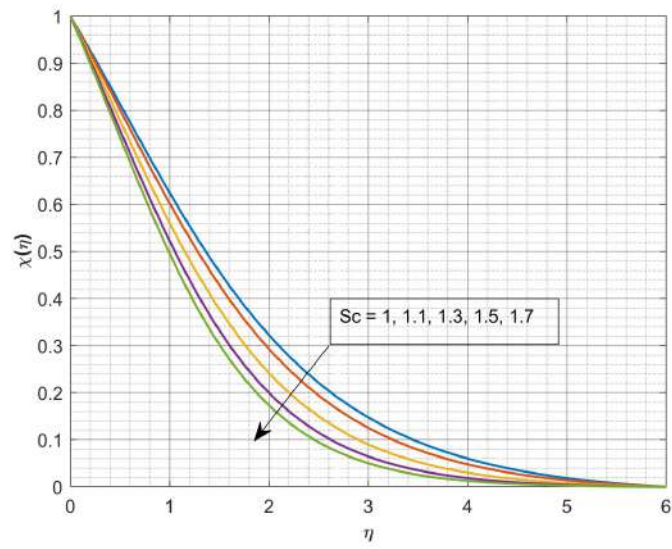


Figure 3.8: Influence of Sc on $\chi(\eta)$.

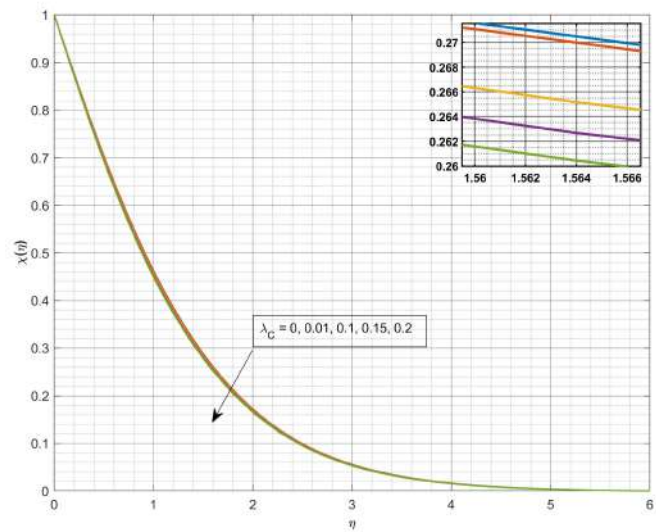


Figure 3.9: Influence of λ_C on $\chi(\eta)$.

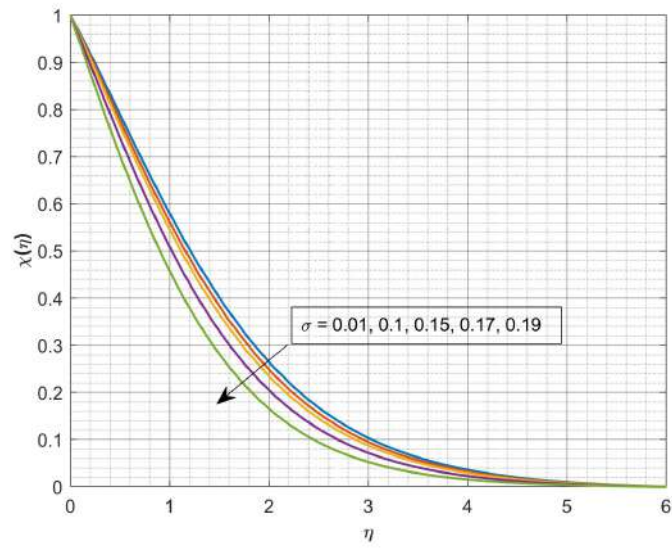


Figure 3.10: Influence of σ on $\chi(\eta)$.

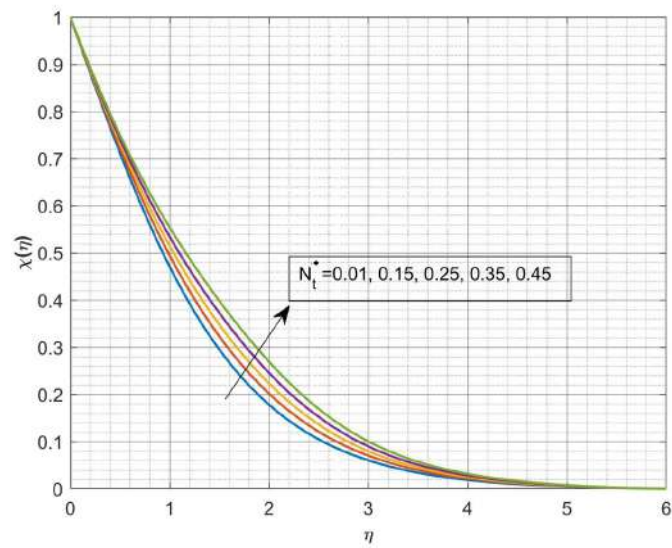


Figure 3.11: Influence of N_t^* on $\chi(\eta)$.

Table 3.3: The numerical values of f'' with respect to pertinent varied parameters:

λ	β_1	β_2	f''
0.2	0.8	1.1	-0.8484
0			-0.8395
0.1			-0.8418
0.11			-0.8422
0.12			-0.8427
	0.1		-0.7431
	0.15		-0.7508
	0.2		-0.7585
		0.1	-1.1745
		0.13	-1.1578
		0.15	-1.1593
		0.18	-1.6316

Table 3.4: The numerical values of θ' with respect to pertinent varied parameters::

λ	β_1	β_2	Q	λ_E	θ'
0.2	0.8	1.1	0.5	0.7	-0.1544
0					-0.1652
0.1					-0.1625
0.11					-0.1619
0.12					-0.1615
	0.1				-0.2587
	0.13				-0.2537
	0.15				-0.2504
	0.18				-0.2455
		0.1			0.0022
		0.13			-0.0045
		0.15			-0.0089
		0.18			-0.0153
			0.1		-0.5847
			0.2		-0.4995
			0.3		-0.4028
			0.4		-0.2902
				0.1	-0.1371
				0.2	-0.1331
				0.3	-0.1307
				0.4	-0.1306

Table 3.5: The numerical values of χ' with respect to pertinent varied parameters:

Sc	λ_C	σ	N_t^*	χ'
1.2	0.2	0.01	0.01	-0.6562
0.8				-0.5464
0.9				-0.574
1				-0.6016
1.1				-0.6276
	0.1			-0.671
	0.13			-0.6665
	0.15			-0.6636
	0.18			-0.6592
		0.1		-0.569
		0.13		-0.5379
		0.15		-0.5166
		0.18		-0.4834
			0.1	-0.6498
			0.13	-0.6477
			0.15	-0.6464
			0.18	-0.6445

Chapter 4

Darcy-Forchheimer flow of dusty tangent hyperbolic fluid over a stretching sheet with Cattaneo-Christov heat flux

4.1 Prelude:

The influence of Darcy-Forchheimer flow and Cattaneo-Christov heat transfer of dusty tangent hyperbolic fluid (THF) across a stretching sheet (SS) is investigated in this chapter. The model's issue is represented by highly nonlinear partial differential equations that were determined with the use of appropriate approximations. Using correct similarity variables, the governing equations in the present situation are changed into nonlinear coupled ordinary differential equations. The Runge-Kutta-Fehlberg-45 technique is used to solve these equations numerically. The effects of different factors on velocity and temperature profiles have been shown using graphs, and the key aspects have been explained in depth. Graphs and tables are also used to display the numerical values of the skin friction coefficient and the local Nusselt number. The temperature profile for both fluid and dust phases is reported to be reduced when the Prandtl number increases.

4.2 Mathematical Elucidation:

Let us consider a steady flow of an incompressible THF over a stretching sheet. As illustrated in Fig. 4.1, it is assumed that the flow is restricted to the region $y > 0$. The flow is generated by the action of two equal and opposite forces along the x -axis and y -axis being normal to the flow. The number density is assumed to be constant and volume fraction of dust particle is neglected. The fluid and dust particles motion are coupled only through drag and heat transfer between them. The drag force is modeled using Stokes linear drag theory. Other interaction forces such as the virtual force, the shear lift force and the spin-lift force will be neglected compared to the drag force. The term T_w represents the temperature of fluid at the sheet, whereas T_∞ denotes the ambient fluid temperature.

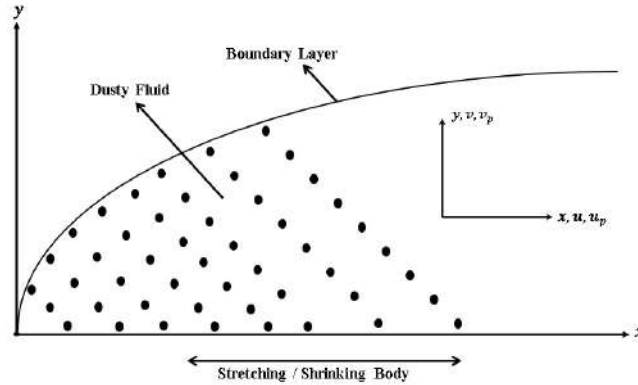


Figure 4.1: Flow Geometry

The constitutive equation of THF is

$$\bar{\tau} = [\mu_0 + (\mu_0 + \mu_\infty) \tanh(\Gamma \bar{\gamma})^n] \bar{\gamma}, \quad (4.2.1)$$

in which, $\bar{\tau}$ is the extra stress tensor, μ_∞ is the infinite shear rate viscosity, μ_0 is the

zero-shear rate viscosity, Γ is the time-dependent material constant, n is the power law index i.e flow behavior index and $\bar{\gamma}$ is defined as,

$$\bar{\gamma} = \sqrt{\frac{1}{2} \sum_i \sum_j \bar{\gamma}_{ij} \bar{\gamma}_{ji}} = \sqrt{\frac{1}{2} \Pi},$$

Consider the equation (4.2.1), for the case when $\mu_\infty = 0$, because it is not possible to discuss the problem for infinite shear rate viscosity and since we have considered tangent hyperbolic fluid that describes shear thinning effects so $\Gamma^* \bar{\gamma} < 1$. Then equation (4.2.1) takes the form,

$$\begin{aligned} \bar{\tau} &= \mu_0 [(\Gamma^* \bar{\gamma})^n] \\ &= \mu_0 [1 + n(\Gamma^* \bar{\gamma} - 1)] \bar{\gamma}. \end{aligned}$$

Governing equations for THF model after applying the boundary layer approximations can be defined as follows,

$$\frac{\partial u}{\partial x} + \frac{\partial v}{\partial y} = 0, \quad (4.2.2)$$

$$u \frac{\partial u}{\partial x} + v \frac{\partial u}{\partial y} = \nu(1-n) \frac{\partial^2 u}{\partial y^2} + \sqrt{2} \nu n \Gamma \frac{\partial u}{\partial y} \frac{\partial^2 u}{\partial y^2} + \frac{K_2 N}{\rho} (u_p - u) - \frac{\nu}{K_1} u - \frac{C_F \sqrt{K_1}}{\nu} u^2, \quad (4.2.3)$$

$$\frac{\partial u_p}{\partial x} + \frac{\partial v_p}{\partial y} = 0, \quad (4.2.4)$$

$$\rho_p (u_p \frac{\partial u_p}{\partial x} + v_p \frac{\partial u_p}{\partial y}) = K_2 N (u - u_p), \quad (4.2.5)$$

Consider the appropriate boundary conditions applicable to the present problem as;

$$\left. \begin{aligned} u = u_w(x), \quad v = 0, \quad \text{at } y = 0, \\ u \rightarrow 0, \quad u_p \rightarrow 0, \quad v_p \rightarrow v, \quad y \rightarrow \infty. \end{aligned} \right\} \quad (4.2.6)$$

where $u_w(x) = bx$ is the stretching sheet velocity with ($b > 0$) as the stretching rate.

Now, introduce the following similarity transformations;

$$\left. \begin{aligned} u &= bx f'(\eta), \quad v = -\sqrt{\nu b} f(\eta), \quad \eta = \sqrt{\frac{b}{\nu}} y, \\ u_p &= bx F'(\eta), \quad v_p = -\sqrt{\nu b} F(\eta), \end{aligned} \right\} \quad (4.2.7)$$

The equations (4.2.2) and (4.2.4) are identically satisfied, in terms of relations(4.2.7). In addition, the equation (4.2.3) and (4.2.5) are reduced to the following set of non-linear ordinary differential equations;

$$\begin{aligned} (1 - n) f'''(\eta) - [f'(\eta)]^2 + f''(\eta) f(\eta) + n W_e f'''(\eta) f''(\eta) \\ + l \beta_v [F'(\eta) - f'(\eta)] - K_p f'(\eta) - Fr [f'(\eta)]^2 = 0, \end{aligned} \quad (4.2.8)$$

$$F(\eta) F''(\eta) - [F'(\eta)]^2 + \beta_v [f'(\eta) - F'(\eta)] = 0, \quad (4.2.9)$$

Transformed boundary conditions are;

$$\left. \begin{aligned} f'(\eta) = 1, \quad f(\eta) = 0 \text{ at } \eta = 0 \\ f'(\eta) \rightarrow 0, \quad F'(\eta) \rightarrow 0, \quad F(\eta) \rightarrow f(\eta) \text{ as } \eta \rightarrow \infty \end{aligned} \right\} \quad (4.2.10)$$

where $l = \frac{Nm}{\rho}$ is the mass concentration parameter of dust particles, $\tau_v = \frac{m}{K_2}$ is the relaxation time of the dust particles, $\beta_v = \frac{1}{b\tau_v}$ is the fluid-particle interaction parameter for velocity, $K = \frac{\nu}{K_2 b}$ is the porosity parameter, $Fr = \frac{C_F u_w}{b\sqrt{K_1}}$ is the local inertia parameter, $W_e = \frac{\sqrt{2b}\Gamma u_w}{\sqrt{\nu}}$ is the Weissenberg number and n is the power law index parameter.

4.3 Heat Transfer Analysis:

The governing boundary layer heat transport equations for both fluid and dust phase are given by

$$\begin{aligned}
c_p \rho \left(u \frac{\partial T}{\partial x} + v \frac{\partial T}{\partial y} \right) + \lambda \left(u \frac{\partial u}{\partial x} \frac{\partial T}{\partial x} + v \frac{\partial v}{\partial y} \frac{\partial T}{\partial y} + u \frac{\partial v}{\partial x} \frac{\partial T}{\partial y} + v \frac{\partial u}{\partial y} \frac{\partial T}{\partial x} \right) \\
+ \lambda \left(2uv \frac{\partial^2 T}{\partial x \partial y} + u^2 \frac{\partial^2 T}{\partial x^2} + v^2 \frac{\partial^2 T}{\partial y^2} \right) = k \frac{\partial^2 T}{\partial y^2} + \frac{\rho_p C_p}{\tau_T} (T_p - T) \\
+ \frac{\rho_p}{\tau_v} (u_p - u)^2 - \frac{\partial q_r}{\partial y}
\end{aligned} \tag{4.3.1}$$

$$u_p \frac{\partial T_p}{\partial x} + v_p \frac{\partial T_p}{\partial y} = - \frac{C_p}{c_m \tau_T} (T_p - T), \tag{4.3.2}$$

where, T and T_p are the temperature of the fluid and dust particles respectively, c_p and c_m are the specific heat of fluid and dust particles respectively, τ_T is the thermal equilibrium time i.e., the time required by the dust cloud to adjust its temperature to that of fluid, λ is the relaxation time of heat flux, k is the thermal conductivity of the fluid, and q_r is the radiative heat flux.

The radiative heat flux expression in equation 4.3.1 is given by

$$q_r = - \frac{16\sigma^{**}}{3k^{**}} T^3 \frac{\partial T}{\partial y}, \tag{4.3.3}$$

where, σ^{**} and k^{**} are the Stefan-Boltzman constant and the mean absorption coefficient respectively,

In view of the equation 4.3.6, the energy equation 4.3.1 becomes;

$$\begin{aligned}
 c_p \rho \left(u \frac{\partial T}{\partial x} + v \frac{\partial T}{\partial y} \right) + \lambda \left(u \frac{\partial u}{\partial x} \frac{\partial T}{\partial x} + v \frac{\partial v}{\partial y} \frac{\partial T}{\partial y} + u \frac{\partial v}{\partial x} \frac{\partial T}{\partial y} + v \frac{\partial u}{\partial y} \frac{\partial T}{\partial x} \right) \\
 + \lambda \left(2uv \frac{\partial^2 T}{\partial x \partial y} + u^2 \frac{\partial^2 T}{\partial x^2} + v^2 \frac{\partial^2 T}{\partial y^2} \right) = k \frac{\partial^2 T}{\partial y^2} + \frac{\rho_p c_p}{\tau_T} (T_p - T) \\
 + \frac{\rho_p}{\tau_v} (u_p - u)^2 + \frac{16\sigma^{**}}{3(\rho c_p)_{nf} k^{**}} \left[T^3 \frac{\partial^2 T}{\partial y^2} + 3T^2 \left(\frac{\partial T}{\partial y} \right)^2 \right]. \quad (4.3.4)
 \end{aligned}$$

The corresponding boundary conditions for the temperature are considered as follows.

$$\left. \begin{aligned}
 T = T_w \text{ at } y = 0, \\
 T \rightarrow T_\infty, \quad T_p \rightarrow T_\infty \text{ as } y \rightarrow \infty
 \end{aligned} \right\} \quad (4.3.5)$$

The dimensionless fluid phase temperature $\theta(\eta)$ and dust phase temperature $\theta_p(\eta)$ are defined as;

$$T = T_\infty(1 + (\theta_w - 1)\theta(\eta)), \quad T_p = T_\infty(1 + (\theta_w - 1)\theta_p(\eta)). \quad (4.3.6)$$

Using 4.3.6 into 4.3.4 and 4.3.2, one can get the following non-linear ordinary differential equations

$$\begin{aligned}
 \theta''(\eta) + R \left[(1 + (\theta_w - 1)\theta)^3 \theta''(\eta) + 3(\theta_w - 1)\theta'^2(\eta)(1 + (\theta_w - 1)\theta(\eta))^2 \right] \\
 + Pr \theta'(\eta)f(\eta) + lPr\beta_t(\theta_p(\eta) - \theta(\eta)) - Pr\Gamma \left[f(\eta)f'(\eta)\theta'(\eta) \right] \\
 - Pr\Gamma \left[f(\eta)^2 \theta''(\eta) \right] + \beta_v lEcPr [F'(\eta) - f'(\eta)]^2 = 0, \quad (4.3.7)
 \end{aligned}$$

$$\theta'_p(\eta)F(\eta) - \gamma_2\beta_t[\theta_p(\eta) - \theta(\eta)] = 0 \quad (4.3.8)$$

The reduced boundary constraints are;

$$\left. \begin{aligned}
 \theta(\eta) = 1 \text{ at } \eta = 0, \\
 \theta(\eta) \rightarrow 0, \quad \theta_p(\eta) \rightarrow 0 \text{ as } \eta \rightarrow \infty.
 \end{aligned} \right\} \quad (4.3.9)$$

where $Pr = \frac{\mu C_p}{k}$ is Prandtl number, the prime denotes the differentiation with respect to η and $R = \frac{4\sigma^* T_\infty^3}{k^* k}$ is the radiation parameter, $Ec = \frac{u_w^2}{c_p(T_w - T_\infty)}$ is the Eckert number, $\gamma_2 = \frac{c_p}{c_m}$ is the specific heat ratio, $\Gamma = \lambda b$ is the relaxation time parameter, $\beta_t = \frac{1}{b\tau_T}$ is the fluid-particle interaction parameter for temperature, $\theta_w = \frac{T_w}{T_\infty} (> 1)$ is the temperature ratio parameter.

The physical quantities of interest, such as skin friction coefficient (C_f) and local Nusselt number (Nu_x) are defined as;

$$C_f = \frac{\tau_w}{\rho u_w^2}, \quad Nu_x = \frac{u_w q_w}{ak(T_\infty - T_w)}$$

where the shear stress (τ_w) and surface heat flux (q_w) are given by;

$$\tau_w = \mu_0 \left((1-n) \frac{\partial u}{\partial y} + \frac{n\Gamma}{\sqrt{2}} \left(\frac{\partial u}{\partial y} \right)^2 \right) \quad \text{and} \quad q_w = -k \frac{\partial T}{\partial y} + q_r.$$

Using the non-dimensional variables, one can get;

$$\sqrt{Re_x} C_f = [(1-n)f''(\eta) + \frac{n}{2} W_e (f''(\eta))^2]_{\eta=0} \quad \text{and} \quad \frac{Nu_x}{\sqrt{Re_x}} = -[1 + R\theta_w^3] \theta'(0),$$

Table 4.1: **Comparison of $-\theta'(0)$ for $R = \Gamma = \beta_v = l = E_c = \beta_t = 0$.**

P_r	0.01	0.72	1	3	10
Grubka and Bobba [70]	0.0099	0.4631	0.5820	1.1652	2.3080
Chen [71]	0.00991	0.46315	0.58199	1.16523	2.30796
Present Work	0.00993	0.46318	0.58231	1.16528	2.30799

4.4 Method of Numerical Extraction:

A set of nonlinear ordinary differential equations 4.2.8, 4.2.9, 4.3.7 and 4.3.8 along with the boundary conditions 4.2.10 and 4.3.9 are solved numerically using Runge-Kutta based

shooting method. Initially, the set of nonlinear ordinary differential equations 4.2.8, 4.2.9, 4.3.7 and 4.3.8 are converted to first-order ordinary differential equations, by using the following procedure:

$$f = y_1, f' = y_2, f'' = y_3, F = y_4, F' = y_5.$$

$$y_3' = \frac{1}{(1-n) + nWe y_3} [y_2^2 - y_1 y_3 - l\beta_\nu(y_5 - y_2) + (Fr y_2 + k)y_2], \quad (4.4.1)$$

$$y_5' = \frac{1}{y_4} [y_5^2 + \beta_\nu(y_2 - y_5)] \quad (4.4.2)$$

$$\theta = y_6, \theta' = y_7, \theta_p = y_8.$$

$$y_7' = \frac{1}{1 + R[(1 + (\theta_w - 1)y_6)]^3 - Pr\Gamma y_1^2} Pr \left\{ [(-y_1 y_7) + \Gamma y_1 y_2 y_7 - l\beta_t(y_8 - y_6)] - l\beta_\nu Ec(y_5 - y_2)^2 \right\} - 3R(\theta_w - 1)y_7^2(1 + (\theta_w - 1)y_6)^2, \quad (4.4.3)$$

$$y_8' = \frac{1}{y_4} [\gamma_2 \beta_t(y_8 - y_6)] \quad (4.4.4)$$

with the corresponding boundary conditions;

$$\left. \begin{aligned} y_1 = 0, \quad y_2 = 1, \quad y_6 = 1 \quad \text{at } \eta = 0 \\ y_2 = 0, \quad y_5 \longrightarrow y_1, \quad y_6 \longrightarrow 0, \quad y_8 \longrightarrow 0 \quad \text{as } \eta \longrightarrow \infty. \end{aligned} \right\} \quad (4.4.5)$$

To solve the equations 4.4.1 - 4.4.4, we guess the values of y_3, y_5, y_7 which are not given at the initial conditions. After finding all the initial conditions, the equations 4.4.1 - 4.4.4 are integrated by using Runge-Kutta-Fehlberg-45 method with the successive iterative step length 0.001. For check, comparison Table 4.1 is inserted for - $\theta'(0)$ and it is found that , the current numerical technique has a fair agreement with previously published results.

4.5 Deliberation of Results:

The technical problem has been mathematically formulated by a set of PDEs, which are, in turn, reduced into a set of ODEs on adaptation of similarity variables. The resultant equations are approximated numerically by Runge-Kutta-Fehlberg-45 method with an aid of shooting technique. We have considered the values of dimensionless parameters as $W_e = 0.8$, $K_p = 0.5$, $Fr = 0.8$, $\beta_v = 0.5$, $l = 0.5$, $R = 0.5$, $\theta_w = 1.2$, $\beta_t = 0.5$, $Pr = 5$, $Ec = 0.5$, $n = 1.2$, $\gamma = 0.5$ and $\Gamma = 0.6$. These values have been taken as common for the complete study unless otherwise specified in the figures and tables. In this section, we focus on the physical behaviors of the involved parameters on the velocity and temperature profiles.

Fig. 4.2 and Fig. 4.3 elucidate the effect of porosity parameter (K) on velocity profile and temperature profile for both fluid and dust phase $f'(\eta)$ and $F'(\eta)$. From the Fig. 4.2 it can be perceived that, the higher values of porosity parameter scale back the velocity profile for both fluid and dusty phases. Correspondingly, the momentum boundary layer thickness decreases for rising values of porosity parameter. Physically it justifies that, the porous media is to increase the resistance to the fluid flow which causes a reduction in velocity profiles. From the Fig. 4.3, it is evaluated that, the temperature profiles for both fluid and dust phase increase for larger values of K and thermal boundary layer thickness also shows the same behavior of temperature profiles for higher values of K .

Fig. 4.4 shows the nature of local inertia parameter (Fr) on velocity profile for both fluid and dust phases. It is executed from this figure that the velocity profiles for both the phases get decreased for increasing values of local inertia parameter. Physically, the inertia coefficient is directly proportional to the porosity of the medium and drag coefficient.

Hence, for higher values of C_b , both porosity of the medium and drag coefficient increase. Consequently, the resistive force is improved for the liquid. Therefore, lower velocity that is obtained corresponds to larger local inertia parameter.

Fig. 4.5 and Fig. 4.6 are illustrated for multiple values of Weissenberg number (W_e) on velocity and temperature profiles for both fluid and dust phases. Weissenberg number is the quantitative relation of the relaxation time of the fluid and a particular process time. This ratio will increase the thickness of the fluid. Thus, velocity profile and also the associated boundary layer thickness decreases with increase in W_e , as shown in Fig. 4.5. From the Fig. 4.6, it is executed that, the temperature profile for both the phases gets increased for increasing values of W_e . Furthermore, the thermal boundary layer thickness also enhances for booming values of W_e .

Fig. 4.7 and Fig. 4.8 illustrate the variation of mass concentration of dust particle parameter l on velocity and temperature profiles of both fluid and dust phases. It is evaluated that, the velocity and temperature profiles of fluid and dust phase decay as the values of l go up. In fact, the particle density is decreased due to enhancement in mass concentration of dust particles that responds to decay in velocity and temperature profiles. Furthermore, this parameter has a key role to measure the mass and dust particle number per unit volume within the flow.

The variation of velocity and temperature profile for both the phases are illustrated in the Fig. 4.9 and Fig. 4.10 for various values of β_v and β_t respectively. An uplifted value of β_v can decrease the fluid phase velocity and increase the dust phase velocity. While, evidently, an increase in β_t (Fig. 4.10) can increase the temperature profile of the dust phase and reduce that of the fluid phase. This is because of the presence of dust particles, which produce friction force in the fluid, which retards the fluid flow.

Fig. 4.11 is prepared for the visualization of temperature profile of both the fluid and dust phases by the consideration of different values of Prandtl number Pr . From this figure it is noticed that, the thermal boundary layer thickness minimizes by maximizing the values of Pr . The significant reason for reduction in temperature is, higher Pr has relatively lower thermal conductivity, which causes low heat penetration. Thus, the thermal boundary layer thickness of fluid and dust particles decrease with the rise in Pr . Hence, the suitable value of Pr is quite essential to control the heat transfer rate in industrial and engineering processes.

Fig. 4.12 and Fig. 4.13 depicted to show the effect of radiation R and temperature ratio parameter θ_w on $\theta(\eta)$ and $\theta_p(\eta)$ profiles respectively. One can reveal that, the temperature profile and corresponding boundary layer thickness rises by increasing the values of R and θ_w . Generally, higher values of R produce additional heat to operating fluid that shows associate enhancement within the temperature field. The variation of temperature profile for both the fluid and dust phases is illustrated in Fig. 4.14 for varying values of Eckert number (Ec). It is noticed that, the decrease in temperature profile for both fluid and dust phases with the increasing values of Eckert number. Consequently, the increase in Eckert number decreases the thermal boundary layer thickness.

Fig. 4.15 illustrates the variation of temperature profile with different values of the relaxation time parameter Γ . From this figure, it is observed that the thermal boundary layer decreases by the increasing values of Γ . It is due to the fact that, the elements of the material demand extra time to transport heat to its adjacent particles when larger thermal relaxation time is accounted. Thus, the temperature profile for both the phases decays for enhancing values of Γ .

The profile of local skin friction coefficient (Cf_x) for distinct values of Fr and K is

shown in Fig. 4.16, which illustrates that the greater values of Fr decrease the skin friction coefficient. Furthermore, the enhancing values of K raise the skin friction coefficient. The representation of (Cf_x) for various values of l and β_v is displayed in Fig. 4.17. Here, it is observed that, (Cf_x) is scaled back for increasing values of l and β_v . Fig. 4.18 discusses the variation of the local Nusselt number for different values of non-dimensional parameter R and Ec . Here, increasing values of both R and Ec , declined the local Nusselt number.

Fig. 4.19 discusses the variation of the local Nusselt number for different values of non-dimensional parameters β_t and l . Here, one can see that the increasing values of both β_t and l , increase the local Nusselt number.

Influences of various embedded parameters on skin friction coefficient and Nusselt number are demonstrated in Table 4.2 and Table 4.3 respectively. From the Table 4.2 it is observed that, the local skin friction coefficient enhances for increasing values of K , Fr , β_v and l , but an opposite behavior is observed for increasing values of W_e . Furthermore, from the Table 4.3 it is noticed that, the higher values of R , θ_w , l , β_t , Pr and Γ enhance the local Nusselt number, but a quite reverse situation can be observed for the increasing values of Ec .

4.6 Inference:

The flow and heat transfer of dusty fluid by considering the Darcy-Forchheimer medium has been studied. On using the suitable boundary layer approximations, the present physical problem was described by highly nonlinear partial differential equations. Furthermore, on applying the appropriate similarity transformations, these equations have been converted into five combined ordinary differential equations. The Runge-Kutta-Fehlberg 45-order scheme has been then employed to solve the resulting equations. The

main results are summarized as follows.

- velocity profile decreases for rising values of K and Fr .
- the momentum boundary layer thickness decreases for higher estimation of W_e .
- higher values of Pr reduce the temperature profile and thermal boundary layer thickness for both fluid and dust phases.
- higher values of R enhance the temperature profile for both the phases.
- the temperature profile accelerates with accelerating values of K , W_e and decelerates with l .
- thermal boundary layer thickness enhances for rising values of θ_w .

Table 4.2: Numerica data for skin friction coefficient for different physical parameters.

w_e	K	Fr	β_v	l	$\sqrt{Re_x}C_f$
0.2					1.193156
0.4					1.175613
0.6					1.156921
	0.1				1.070776
	0.3				1.135475
	0.5				1.196525
		0.01			1.166425
		0.1			1.196525
		0.15			1.225829
			0.1		1.112968
			0.2		1.127512
			0.3		1.139657
				0.1	1.107479
				0.2	1.131470
				0.3	1.154905

Table 4.3: Numerical data for local Nusselt number for different physical parameters.

R	θ_w	l	β_t	Pr	τ	Ec	$\frac{Nu_x}{\sqrt{Re_x}}$
0.1							1.497882
0.3							1.651679
0.5							1.788386
	0.6						1.732059
	1.2						1.788386
	1.8						2.240571
		0.1					1.398669
		0.3					1.565647
		0.5					1.717260
			0.6				1.788386
			1.2				2.132679
			1.8				2.384279
				0.5			0.792638
				1.0			1.018604
				1.5			1.230786
					0.01		1.788386
					0.1		1.793728
					0.15		1.796883
						0.1	1.820003
						0.2	1.809464
						0.3	1.798925

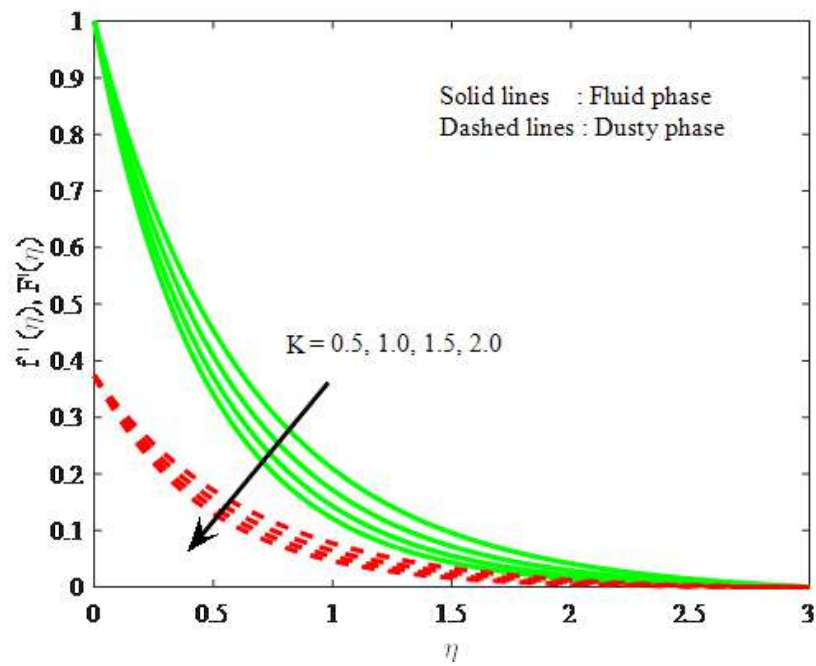


Figure 4.2: Effect of porosity parameter on velocity profile for both fluid and dusty phases

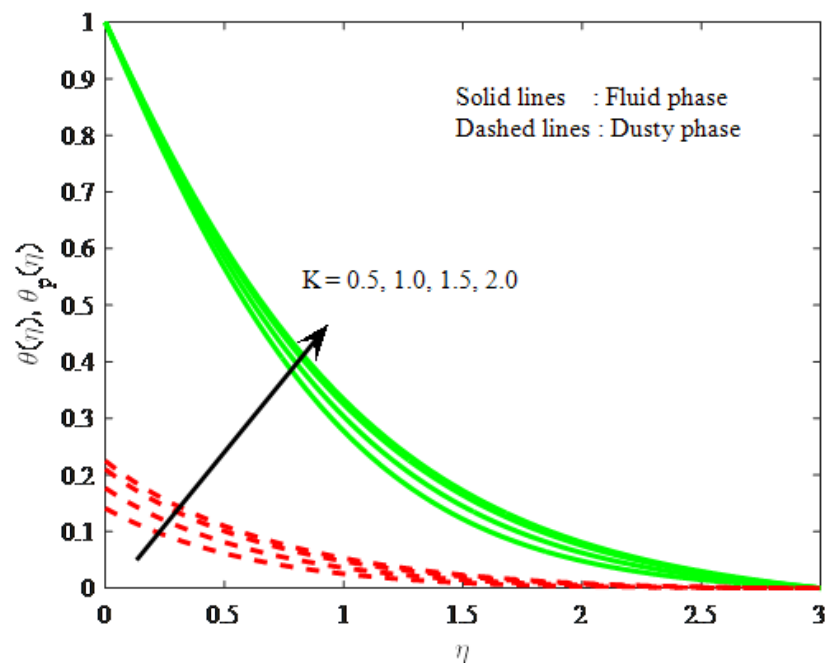


Figure 4.3: Effect of porosity parameter on temperature profile for both fluid and dusty phases.

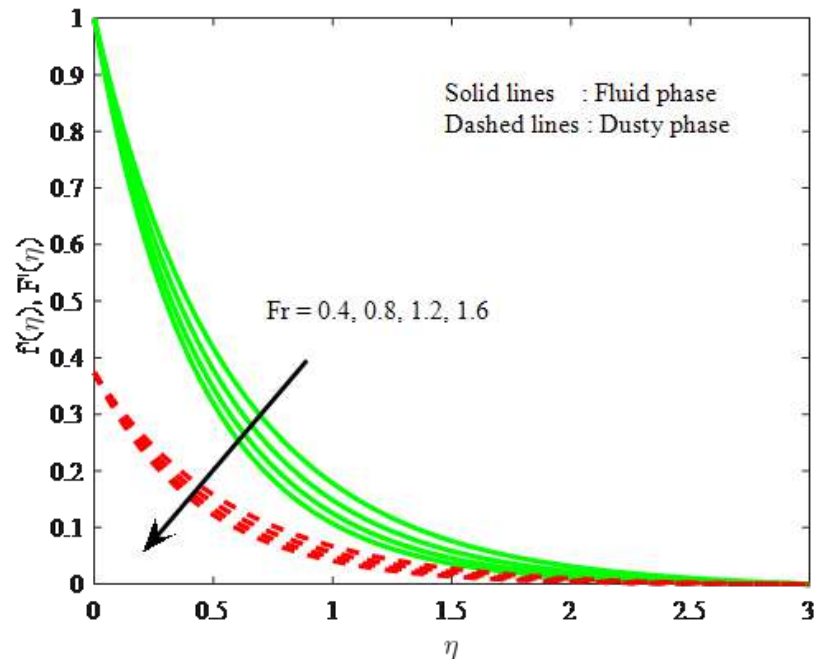


Figure 4.4: Effect of local inertia parameter on velocity profile for both fluid and dust phases.

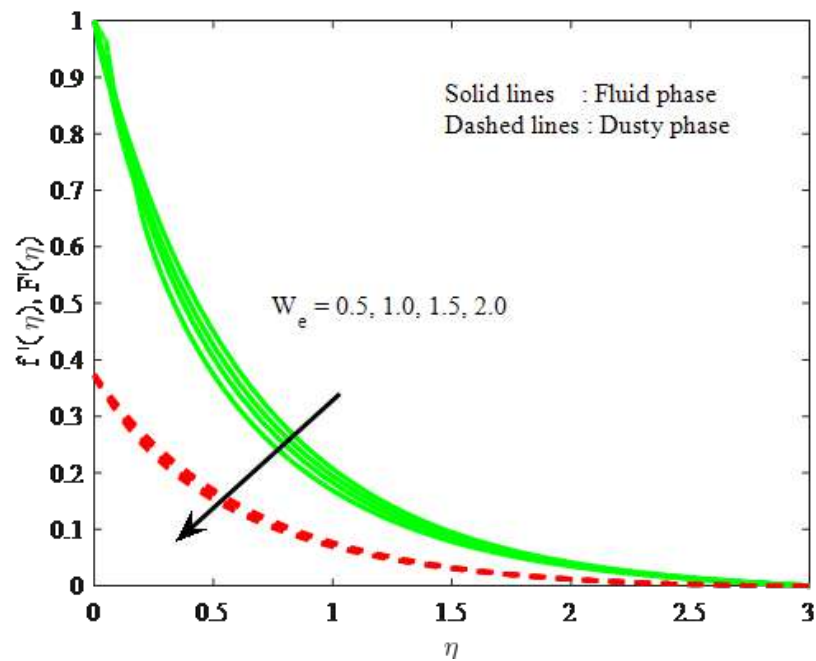


Figure 4.5: Effect of Weissenberg number on velocity profile for both fluid and dusty phases.

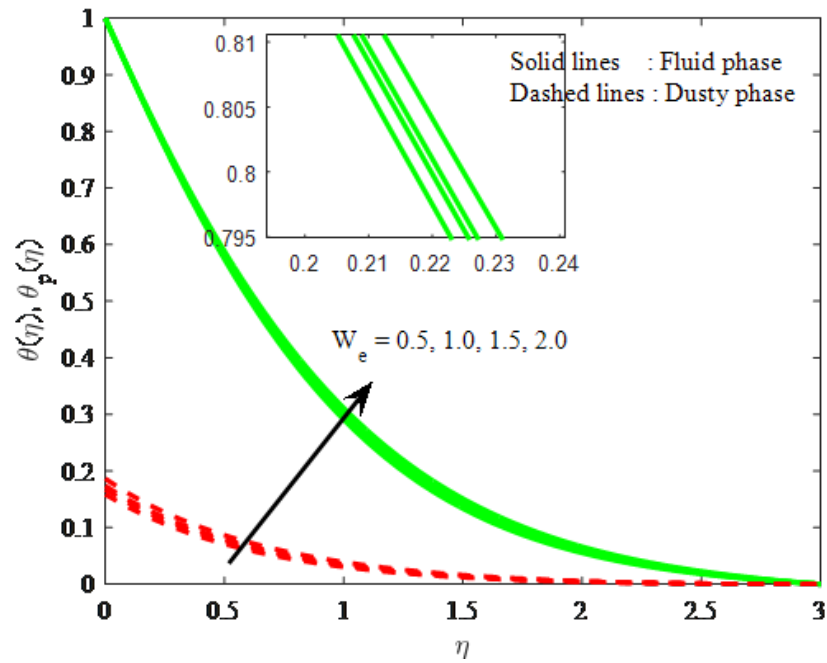


Figure 4.6: Effect of Weissenberg number on temperature profile for both fluid and dusty phases.

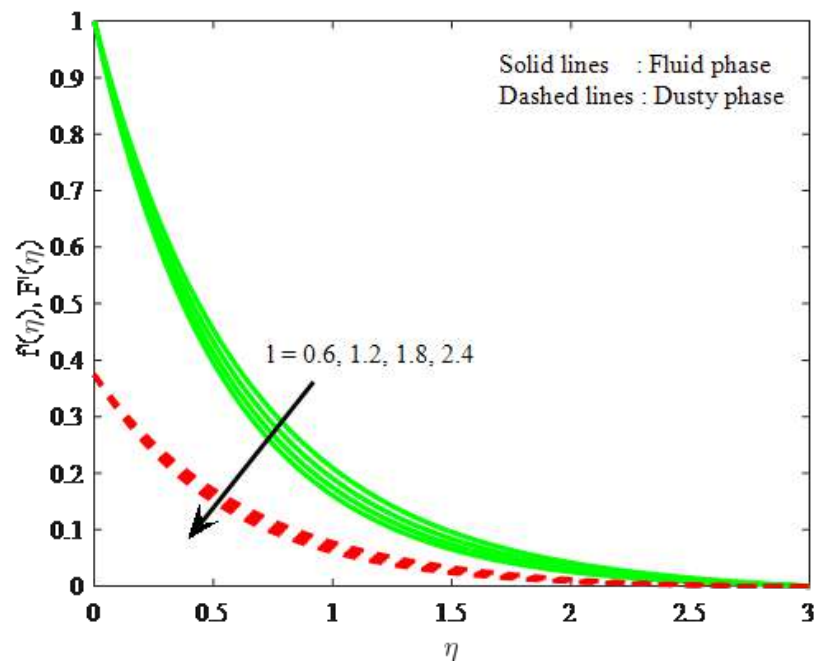


Figure 4.7: Effect of mass concentration parameter on velocity profile for both fluid and dusty phases.

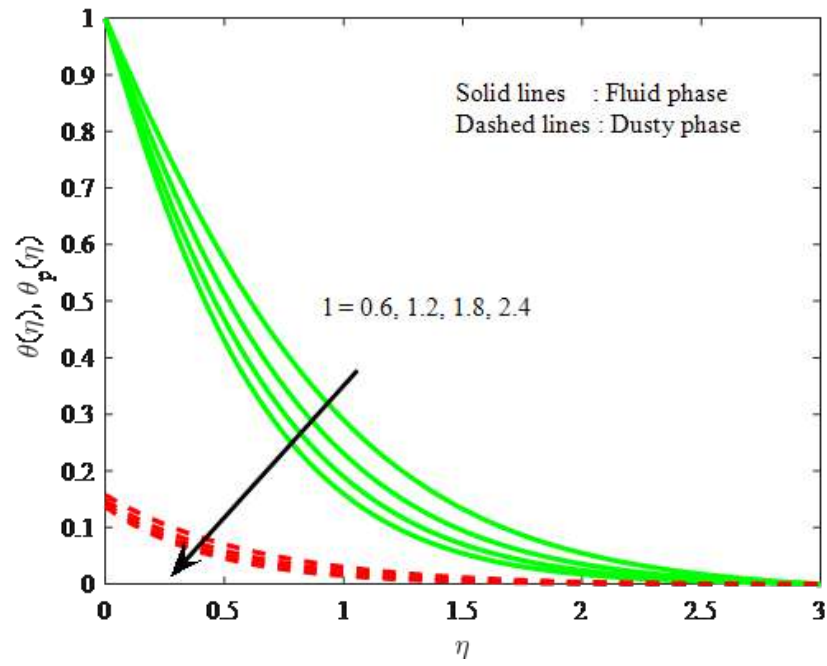


Figure 4.8: Effect of mass concentration parameter on temperature profile for both fluid and dusty phases.

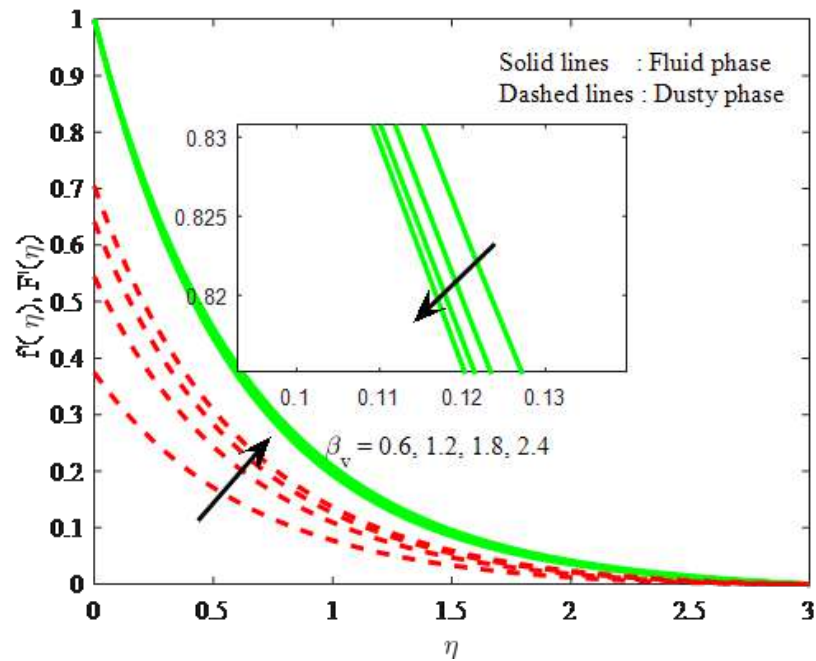


Figure 4.9: Effect of fluid-particle interaction parameter on velocity profile for both fluid and dusty phases.

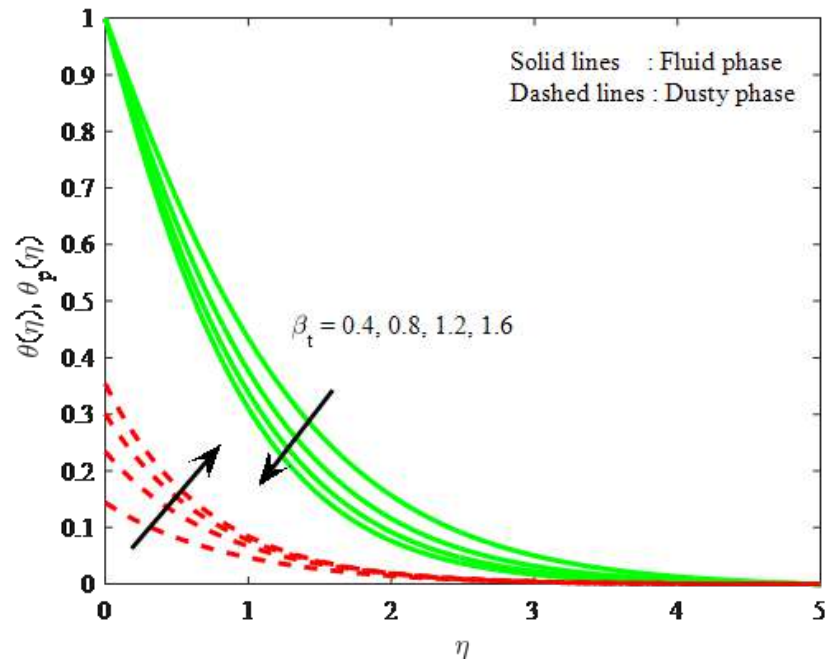


Figure 4.10: Effect of fluid-particle interaction parameter on temperature profile for both fluid and dusty phases.

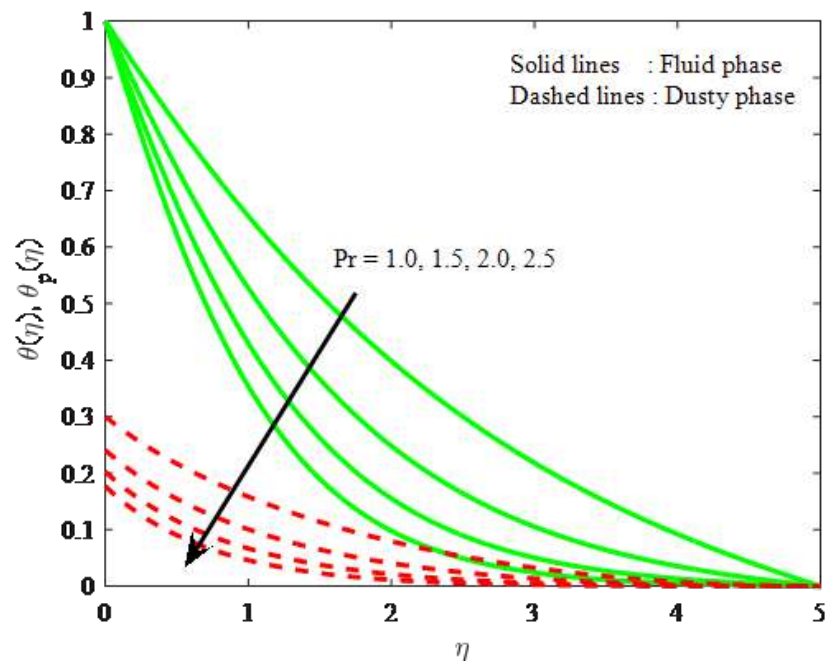


Figure 4.11: Effect of Prandtl number on temperature profile for both fluid and dusty phases.

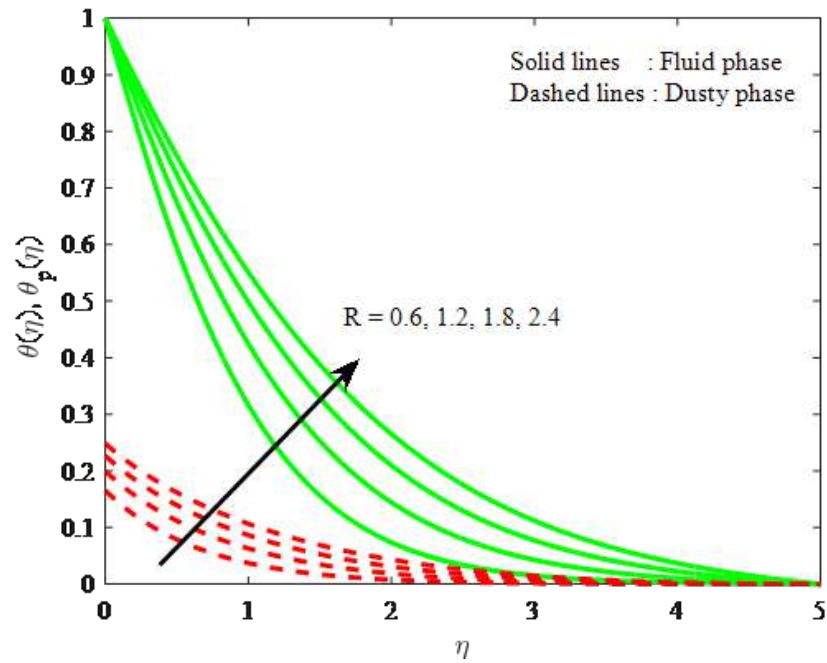


Figure 4.12: Effect of radiation parameter on temperature profile for both fluid and dusty phases.

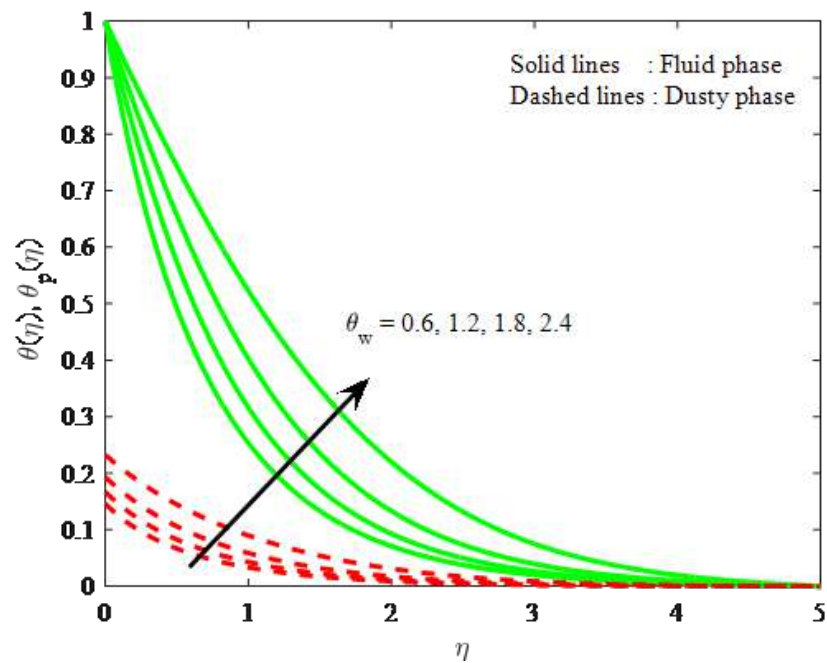


Figure 4.13: Effect of temperature ratio parameter on temperature profile for both fluid and dusty phases.

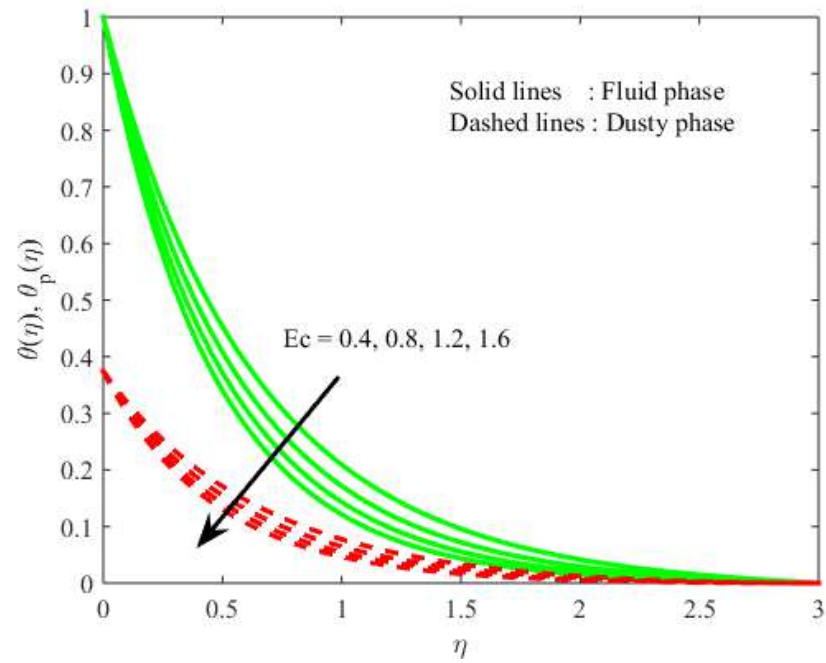


Figure 4.14: Effect of Eckert number on temperature profile for both fluid and dusty phases.

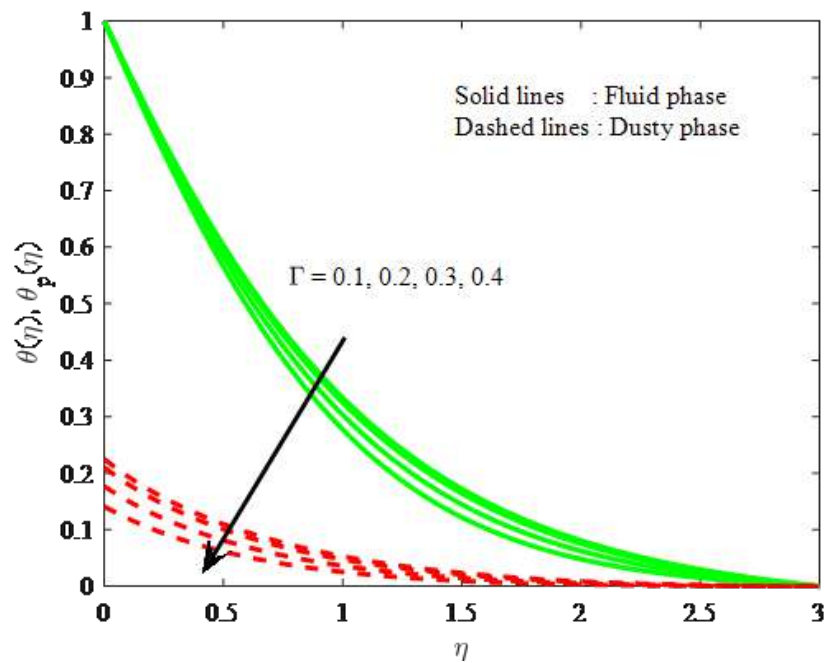


Figure 4.15: Effect of relaxation time parameter on temperature profile for both fluid and dusty phases.

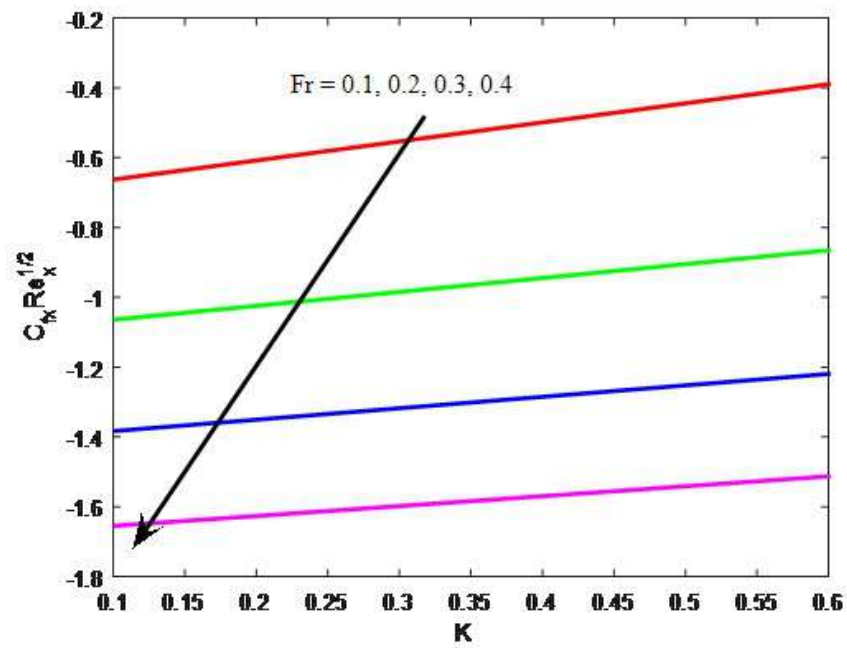


Figure 4.16: Effect of K and Fr on local skin friction coefficient.

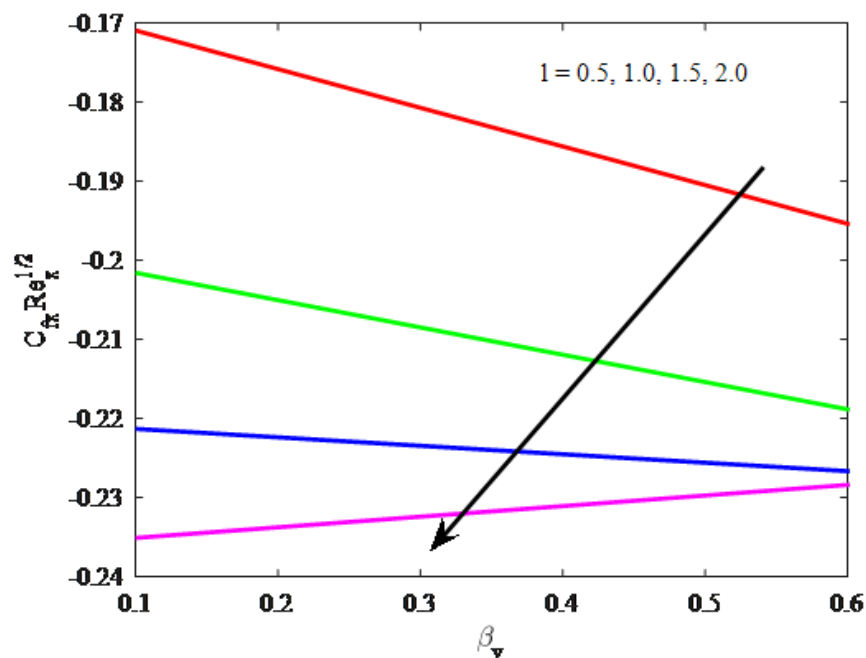


Figure 4.17: Effect of β_v and l on local skin friction coefficient.

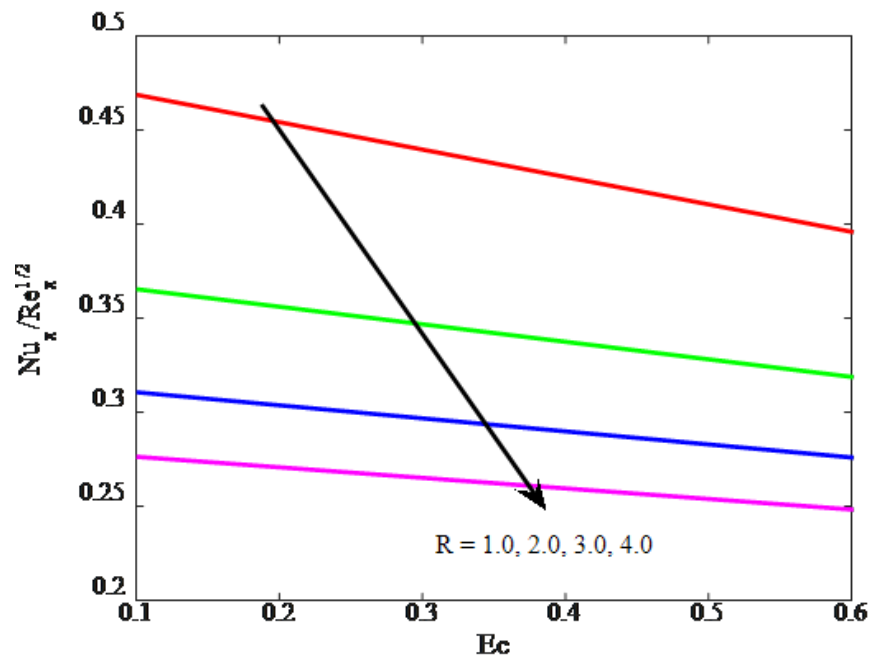


Figure 4.18: Effect of Ec and R on local Nusselt number.

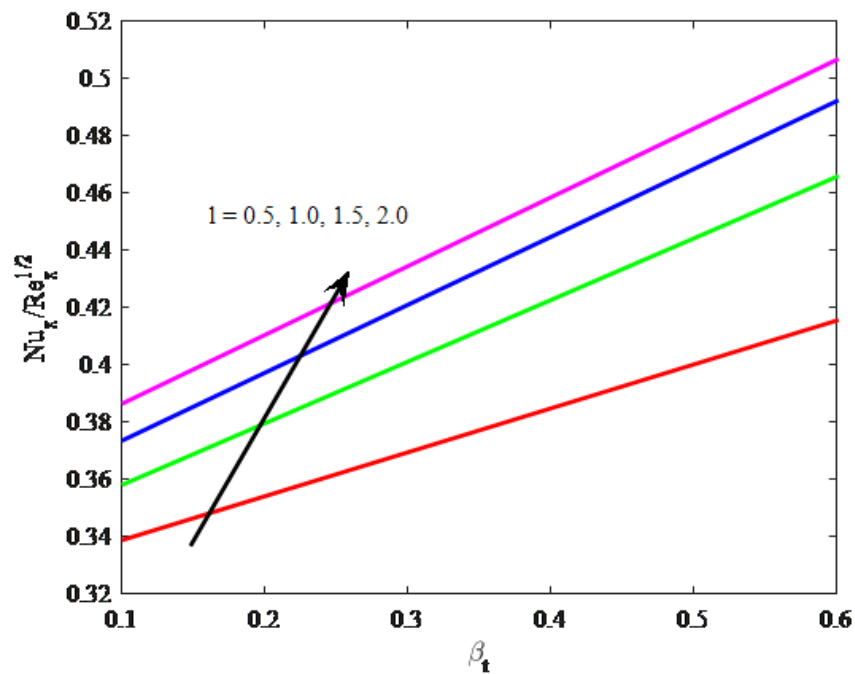


Figure 4.19: Effect of β_t and l on local Nusselt number..

Chapter 5

Influence of thermophoretic particle deposition on the 3D flow of Sodium alginate-based Casson nanofluid over a stretching sheet

5.1 Prelude:

The flow of Casson nanofluid with thermophoretic particle deposition (TPD) impact over a non-linear stretching sheet is explored in this chapter. The governing equations are framed with appropriate assumptions, and then appropriate similarity transformations are used to turn the collection of partial differential equations (PDEs) into ordinary differential equations (ODEs). The RKF-45 approach (Runge Kutta Fehlberg 4th 5th order) is used to solve the reduced equations with the use of a shooting strategy. The numerical findings for linear and non-linear cases are derived, and graphs for different dimensionless restrictions are generated. Results reveals that, improved Casson parameter values reduce axial velocities while improving heat distribution. The concentration profile will decrease as the thermophoretic parameter increases. With enhanced power law index values, the rate of mass transfer and surface drag force will decrease.

5.2 Mathematical Elucidation:

Consider an incompressible, laminar 3D flow of a Casson nanoliquid in the presence of TPD over a non-linearly stretching sheet. The sheet is moving with uniform velocity $u_w = v_w = (x + y)^n a$ in x and y directions respectively with $a, n > 0$. T_w and C_w represents the wall temperature, and concentration as well as T_∞ and C_∞ denotes ambient temperature and concentration. Both T_w and C_w are assumed to be constant on the stretching surface. The ambient values of temperature and concentration are denoted by T_∞ and C_∞ as the value of $z \rightarrow \infty$. Further, temperature and concentration at the wall are more significant than the ambient temperature and concentration. The geometry of the described problem is illustrated in Fig.5.2. Based on the above assumptions, the governing equations and boundary conditions are given by (see Epstein et al. [72], Butt et al. [73], Raju et al. [74], Khan et al. [75]).

$$u_x + v_y + w_z = 0, \quad (5.2.1)$$

$$uu_x + vv_y + ww_z = \left(1 + \frac{1}{\beta}\right) v_{nf} u_{zz} \quad (5.2.2)$$

$$uv_x + vv_y + wv_z = \left(1 + \frac{1}{\beta}\right) v_{nf} v_{zz} \quad (5.2.3)$$

$$uT_x + vT_y + wT_z = \frac{k_{nf}}{(\rho C_p)_{nf}} T_{zz} \quad (5.2.4)$$

$$uC_x + vC_y + wC_z = D_{nf} C_{zz} - ((V_T (C - C_\infty)))_z \quad (5.2.5)$$

Boundary conditions (see Raju et al.[74], Khan et al. [75])

$$\left. \begin{aligned} u = u_w, T = T_w, v = v_w, C = C_w, w = 0 \text{ at } z = 0, \\ C \rightarrow C_\infty, u \rightarrow 0, v \rightarrow 0, T \rightarrow T_\infty \quad \text{as } z \rightarrow \infty. \end{aligned} \right\} \quad (5.2.6)$$

where, u , v , and $w(m s^{-1})$ are the velocity components along the x , y , and $z(m)$ directions respectively. β is the Casson parameter, $\nu = \left(\frac{\mu}{\rho}\right) (m^2 s^{-1})$ signifies the kinematic viscosity, $\mu(kgm^{-1}s^{-1})$ signifies dynamic viscosity, $\rho(kgm^{-3})$ is the density, $k(kgms^{-3}K^{-1})$ signifies thermal conductivity, $Cp(m^2s^{-2}K^{-1})$ signifies specific heat, $D(m^2s^{-1})$ is diffusivity, and $V_T(m s^{-1})$ is the thermophoretic velocity.

The term V_T is defined as

$$V_T = - \left(\frac{k^* v_{nf}}{T_y} \right) T_z \quad (5.2.7)$$

(see Epstein et al. [72]).

Here k^* is the thermophoretic coefficient and T_r is the reference temperature.

The below-mentioned similarity variables are introduced. (see Raju et al. [74], Khan et al. [75])

$$\left. \begin{aligned} v &= a(x+y)^n g'(\eta), \quad w = - \left((f'(\eta) + g'(\eta)) \left(\frac{n-1}{2} \right) \eta + (f(\eta) + g(\eta)) \left(\frac{n+1}{2} \right) \right) (x+y)^{\frac{n-1}{2}} \sqrt{av_f}, \\ u &= a(x+y)^n f'(\eta), \quad \eta = (x+y)^{\frac{n-1}{2}} \sqrt{\frac{a}{v_f}} z, \\ T - T_\infty &= \theta(\eta)(T_w - T_\infty), \quad C = C_\infty + \chi(\eta)(C_w - C_\infty). \end{aligned} \right\} \quad (5.2.8)$$

Substituting equation (5.2.7) and (5.2.8) into (5.2.1-5.2.6) and after simplifying, the following equations are obtained.

$$\left(1 + \frac{1}{\beta} \right) f''' + \zeta_1 \zeta_2 \left((f+g) \left(\frac{n+1}{2} \right) f'' - n f'(f'+g') \right) = 0 \quad (5.2.9)$$

$$\left(1 + \frac{1}{\beta} \right) g''' + \zeta_1 \zeta_2 \left((f+g) \left(\frac{n+1}{2} \right) g'' - n g'(f'+g') \right) = 0 \quad (5.2.10)$$

$$\frac{k_{nf}}{k_f} \theta'' + Pr \zeta_3 \left(\theta' \left(\frac{n+1}{2} \right) (f+g) \right) = 0 \quad (5.2.11)$$

$$\zeta_1 \chi'' + Sc \chi' \left(\frac{n+1}{2} \right) (f+g) - (\theta'' \chi + \chi' \theta') N_t^* Sc = 0 \quad (5.2.12)$$

with

$$\left. \begin{aligned} (f', g', f, g, \theta, \chi)(0) &= (1, 1, 0, 0, 1, 1) \text{ at } \eta = 0 \\ (f', g', \theta, \chi)(\infty) &= (0, 0, 0, 0) \text{ as } \eta \rightarrow \infty \end{aligned} \right\} \quad (5.2.13)$$

where,

$$\zeta_1 = (1 - \phi)^{2.5}, \quad \zeta_2 = (1 - \phi + \phi \frac{\rho_s}{\rho_f}), \quad \zeta_3 = (1 - \phi + \phi \frac{(\rho Cp)_s}{(\rho Cp)_f}), \quad Sc = \frac{\nu_f}{D_f},$$

$$Pr = \frac{\mu_f Cp_f}{k_f}, \quad N_t^* = -\frac{k^*(T_w - T_\infty)}{T_f}$$

The thermophysical properties of nanofluid are given by: (see Khan et al. [76], Devi and Devi [77])

$$\left. \begin{aligned} k_{nf} &= \frac{-2\phi(-k_s+k_f)+2k_f+k_s}{2\phi(-k_s+k_f)+2k_f+k_s} k_f, \\ (\rho Cp)_{nf} &= \left((1 - \phi + \frac{(\rho Cp)_s}{(\rho Cp)_f} \phi) \right) (\rho Cp)_f, \\ \mu_{nf} &= \frac{\mu_f}{(1-\phi)^{2.5}}, \\ \rho_{nf} &= \rho_f \left(1 - \phi + \phi \frac{\rho_s}{\rho_f} \right), \\ D_{nf} &= D_f (1 - \phi)^{2.5}, \end{aligned} \right\} \quad (5.2.14)$$

Engineering coefficients:

The expressions and reduced forms of skin friction along x and y direction is given as follows (see Raju et al. [74], Khan et al. [75])

Table 5.1: Nanoliquid and base liquid thermophysical characteristics:(see Khan et al.[76])

Property	$C_6H_9NaO_7(SA)$	Al_2O_3
Pr	6.45	-
ρ	989	3970
C_p	4175	765
k	0.613	40

a. Along x direction:

$$C_{fx} = \frac{\mu_{nf} \left(1 + \frac{1}{\beta}\right) (u_z + w_x)_{z=0}}{\rho_f u_w^2} \rightarrow \sqrt{Re} C_{fx} = \left(1 + \frac{1}{\beta}\right) \frac{f''(0)}{\zeta_1} \quad (5.2.15)$$

b. Along y direction:

$$C_{fy} = \frac{\mu_{nf} \left(1 + \frac{1}{\beta}\right) (v_z + w_y)_{z=0}}{\rho_f u_w^2} \rightarrow \sqrt{Re} C_{fy} = \left(1 + \frac{1}{\beta}\right) \frac{g''(0)}{\zeta_1} \quad (5.2.16)$$

Nusselt number:

$$Nu = \frac{-k_{nf}(x+y)(T_z)_{z=0}}{k_f(T_w - T_\infty)} \rightarrow \frac{Nu}{\sqrt{Re_x}} = \frac{-k_{nf}\theta'(0)}{k_f} \quad (5.2.17)$$

Sherwood number:

$$Sh = \frac{-D_{nf}(x+y)(C_z)_{z=0}}{D_f(C_w - C_\infty)} \rightarrow \frac{Sh}{\sqrt{Re_x}} = -\zeta_1 \chi'(0) \quad (5.2.18)$$

where, $Re_x = \frac{u_w \nu_f^{-1}}{(x+y)^{-1}}$ is local Reynold number.

5.3 Method of Numerical Extraction:

The set of reduced equations stated in equations (5.2.9-5.2.12) and boundary constraints (5.2.13) are solved using RKF-45 method and the shooting scheme. The competence

of this technique is hightened due to the depletion of computational time. To get the solution, we reduce the system of ODEs and boundary conditions into a first-order system by substituting

$$a_1 = f, a_2 = f', a_3 = f'', a_4 = g, a_5 = g', a_6 = g'', a_7 = \theta, a_8 = \theta', a_9 = \chi, a_{10} = \chi' \quad (5.3.1)$$

we get

$$\begin{bmatrix} a_1' \\ a_2' \\ a_3' \\ a_4' \\ a_5' \\ a_6' \\ a_7' \\ a_8' \\ a_9' \\ a_{10}' \end{bmatrix} = \begin{bmatrix} a_2 \\ a_3 \\ \frac{-1}{\left(1 + \frac{1}{\beta}\right)} \zeta_1 \zeta_2 \left(\left(\frac{n+1}{2}\right) (f+g)f'' - nf'(f'+g') \right) \\ a_5 \\ a_6 \\ \frac{-1}{\left(1 + \frac{1}{\beta}\right)} \zeta_1 \zeta_2 \left(\left(\frac{n+1}{2}\right) (f+g)g'' - ng'(f'+g') \right) \\ -\frac{k_f}{k_{nf}} Pr \zeta_3 \left(\left(\frac{n+1}{2}\right) (f+g)\theta' \right) \\ a_{10} \\ \frac{1}{\zeta_1} \left((a_8\chi' + \chi'\theta') N_t^* Sc - Sc \left(\frac{n+1}{2}\right) \chi'(f+g) \right) \end{bmatrix} \quad (5.3.2)$$

with

$$\begin{bmatrix} a_1(0) \\ a_2(0) \\ a_3(0) \\ a_4(0) \\ a_5(0) \\ a_6(0) \\ a_7(\infty) \\ a_8(\infty) \\ a_9(\infty) \\ a_{10}(\infty) \end{bmatrix} = \begin{bmatrix} 0 \\ 1 \\ \lambda_1 \\ 0 \\ 1 \\ \lambda_2 \\ 1 \\ \lambda_3 \\ 1 \\ \lambda_4 \end{bmatrix} \quad (5.3.3)$$

The IVP stated in equations 5.3.2 and 5.3.3 are solved by the RKF-45 method and unknown values are obtained by shooting scheme by setting step size $h = 0.01$ and error

tolerance 10^{-6} , which satisfy the boundary condition at infinity. The numerical solutions are obtained by setting the constraints' values $\phi = 0.01$, $\beta = 0.5$, $Pr = 6.45$, $Sc = 0.8$ and $N_t^* = 0.1$. Fig.5.1 shows the flow chart for numerical scheme. The solutions are compared with the existing works and they best match each other (see Table 5.2 and Table 5.3).

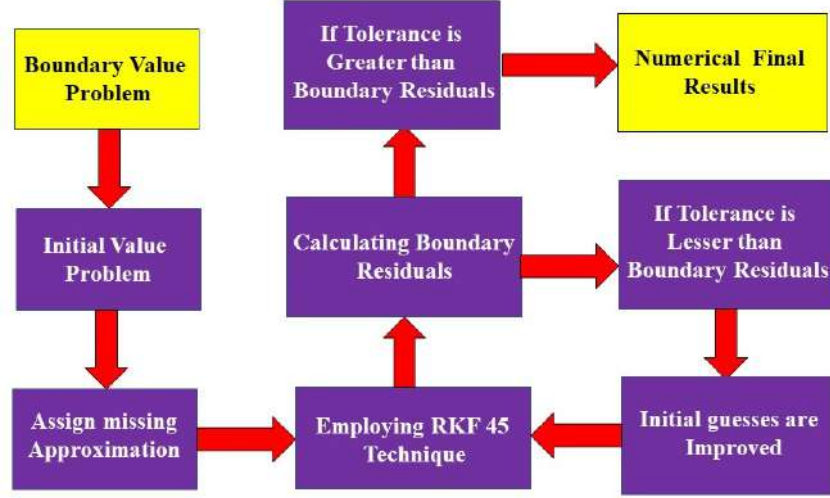


Figure 5.1: Flow chart for Numerical scheme.

Table 5.2: Comparison of the model for $f''(0)$ in the absence of ϕ and $\left(1 + \frac{1}{\beta} = 1\right)$

n	Khan et al. [75]	Raju et al. [74]	Present Result
1	-1.414214	-1.4142141	-1.41592
3	-2.297186	-2.2971860	-2.297297

5.4 Deliberation of Results:

The fundamental goal of the present section is to analyse the influence of various dimensionless constraints on their respective profiles. The reduced ODEs (5.2.9-5.2.12) and

Table 5.3: Comparison of the model for $g''(0)$ in the absence of ϕ and $\left(1 + \frac{1}{\beta} = 1\right)$

n	Khan et al. [75]	Raju et al. [74]	Present Result
1	-1.414214	-1.4142141	-1.41592
3	-2.297186	-2.2971860	-2.297297

boundary conditions (5.2.13) are numerically solved with RK-45 and shooting schemes. Since we convert the ODEs into IVP and shooting scheme is adopted to obtain the missing boundary conditions. The numerical procedure is validated with the previous existing works. The obtained results show the influence of the dimensionless parameters, i.e., Casson parameter (β), power-law index (n), Schmidt number (Sc), thermophoretic parameter N_t^* on the axial velocity profiles, thermal and concentration profiles. Throughout the analysis, computations are made for the power-law index $n = 1$ and $n = 3$.

Fig. 5.3 estimates the influence of the β on axial velocity $f'(\eta)$. The rise in the values of the β will diminish $f'(\eta)$. From the physical point of view, increased β ($= 0.1, 0.2, 0.3$) values reduce fluid flow because the flow is subjected to a higher viscous force. It is further observed that axial velocity is diminished more in the case of $n = 3$ than $n = 1$. The influence of the β on axial velocity $g'(\eta)$ is displayed in Fig. 5.4. A similar trend is observed as seen in the axial velocity profile $f'(\eta)$. The variation of the thermal distribution profile $\theta(\eta)$ for the rise in the values of the Casson parameter (β) is portrayed in Fig. 5.5. The rise in the values of β will enrich the thermal distribution in the system. In physical view, increasing the Casson parameter β increases the fluid's boundary layer thickness, resulting in increased thermal distribution. Thermal distribution is more in the case of $n = 3$ than $n = 1$. Fig. 5.6 is drawn to show the influence of the β on the mass transfer profile $\chi(\eta)$. The Casson parameter's rise will enhance the accumulation of particles results

in the enrichment of boundary layer thickness. As a result, the mass transfer enhances. Enhancement in concentration is more in the case of $n = 1$ than $n = 3$.

The variation of N_t^* on $\chi(\eta)$ is revealed in Fig. 5.7. The enhancement in N_t^* values will reduce concentration $\chi(\eta)$. The mobility of the particles increases as the temperature gradient grows, resulting in a decrease in fluid concentration. The influence of the Sc on the $\chi(\eta)$ is drawn in Fig. 5.8. The concentration profile decreases as the Schmidt number increases. Schmidt number is the physical definition of the kinematic viscosity to molecular diffusion coefficient ratio. As a result, the enhanced values of Sc declines $\chi(\eta)$. The significant concentration diminishes in the case $n = 3$ than $n = 1$ for N_t^* and Sc . Fig.5.9(a) represents the variation of surface drag force in x direction on n for various values of β . The rise in the values of β will weaken the surface drag force. This is due to improvement in the values of β , and n values will improve the thermal boundary layer and the liquid distribution. As a result, the surface drag will reduce. Similar behaviour is seen in surface drag force along y direction (see Fig.5.9(b)). The variation of rate of thermal distribution on n for numerous values of ϕ is shown in Fig. 5.10(a). The rise in the solid volume fraction will improve the boundary layer thickness and improve the thermal distribution rate. Fig. 5.10 (b) illustrates the consequence of the rate of mass transfer on Sc for numerous values of N_t^* . The rate of mass transfer will enhance with the increase in the thermophoretic parameter.

Table 5.4 is drawn to show the computational values of $f''(0)$, $g''(0)$, $\theta'(0)$, and $\chi'(0)$ over various dimensionless constraints. From the table, it is clear that increased values of n will diminish the surface drag coefficients $f''(0)$ and $g''(0)$ along x and y directions and mass transfer rate but improves the rate of thermal distribution. The addition of solid volume fraction will diminish the $f''(0)$, $g''(0)$, $\theta'(0)$ and $\chi'(0)$ profiles. The increase

in the values of β will reduce $f''(0)$ and $g''(0)$, but a reverse trend is seen for $\theta'(0)$ and $\chi(0)$ profiles. Improvement in the values of Sc and N_t^* will decrease the $\theta'(0)$ and $\chi'(0)$ profiles.

5.5 Inference:

An incompressible, laminar 3D flow of a Casson nanoliquid in the presence of TPD over a non-linearly stretching sheet is examined. To convert the collection of PDEs into ODEs, the governing equations are constructed with appropriate assumptions, and acceptable similarity variables are employed. The simplified equations are solved using software by applying the RKF-45 method with shooting scheme. The graphs are drawn for various constraints, and important engineering factors are discussed in detail. The significant findings of the current study are as follows:

- Improvement in the Casson parameter will decline the axial velocity in x and y directions.
- The thermal distribution is improved when the Casson parameter values are increased.
- Improved values of Schmidt number will decline the concentration.
- An increase in the values of the thermophoretic parameter affects the concentration profiles.
- The rate of mass transfer will decrease with an upsurge in the values of the thermophoretic parameter.

- The rate of thermal distribution will improve with an increment in the Casson parameter.
- The axial velocity and thermal distribution will be more in case of $n = 3$ but, a reverse trend is perceived in case of concentration profile.

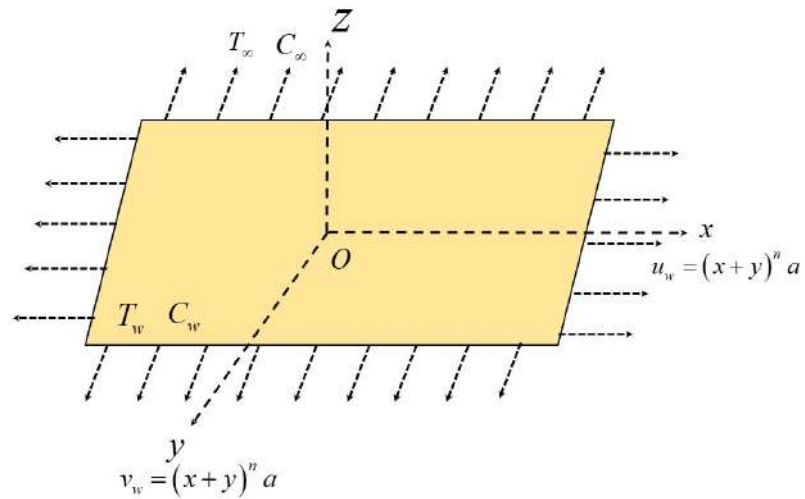


Figure 5.2: Flow Geometry.

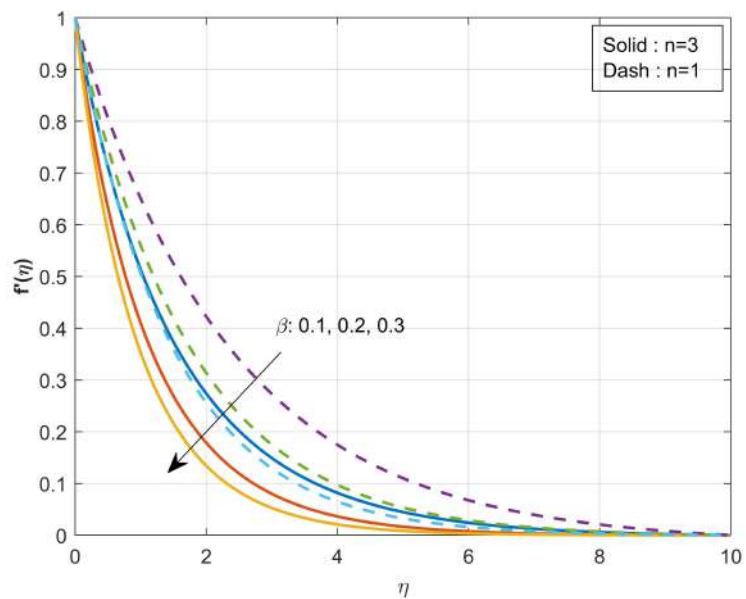


Figure 5.3: Influence of β over axial velocity $f'(\eta)$

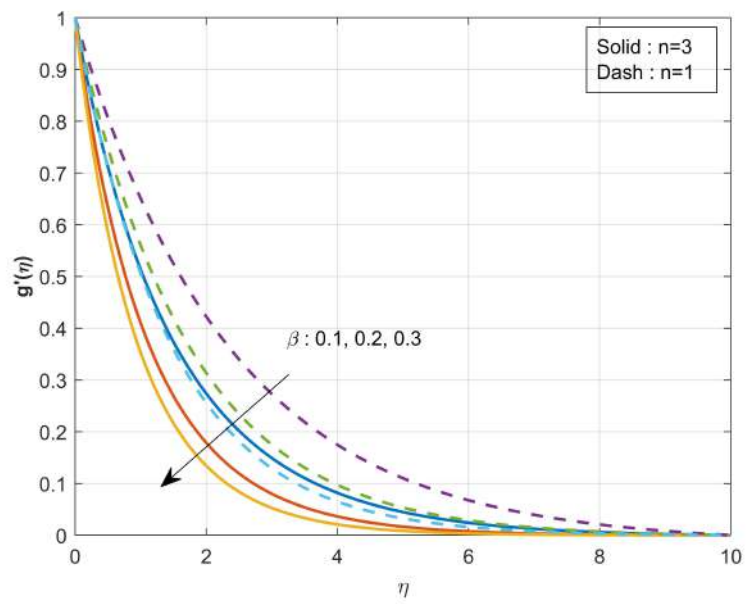


Figure 5.4: Influence of β over axial velocity $g'(\eta)$

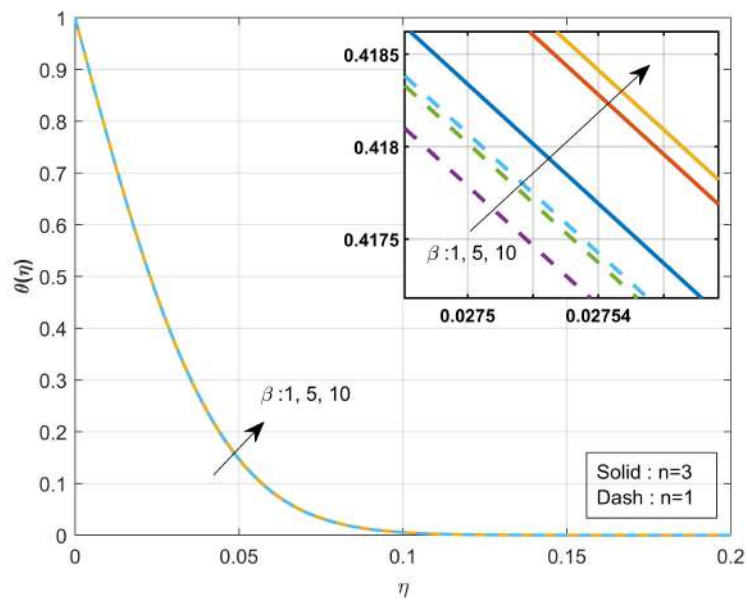


Figure 5.5: Influence of β over thermal profile $\theta(\eta)$

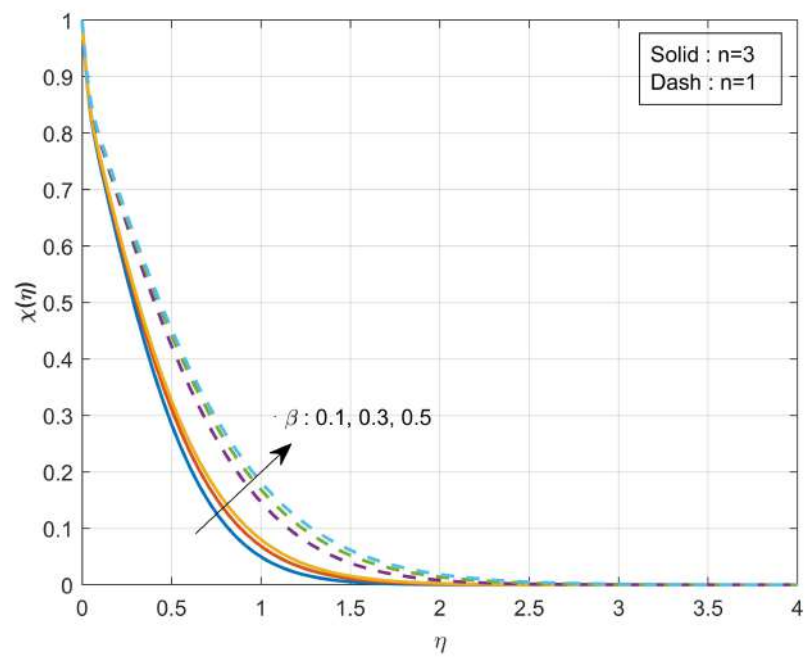


Figure 5.6: Influence of β over concentration $\chi(\eta)$

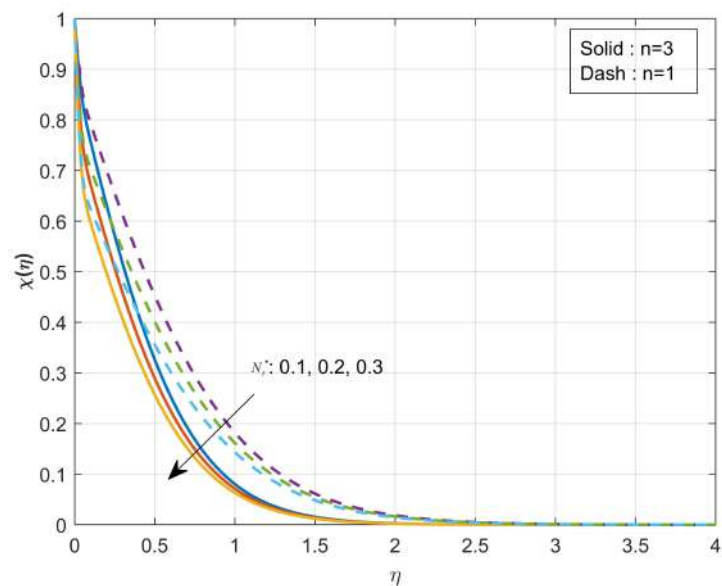


Figure 5.7: Influence of N_t^* over concentration $\chi(\eta)$.

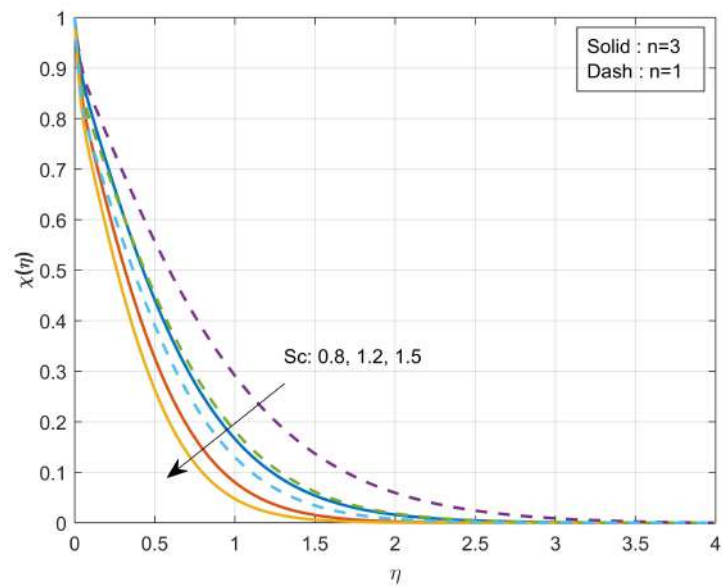


Figure 5.8: Influence of Sc over concentration $\chi(\eta)$

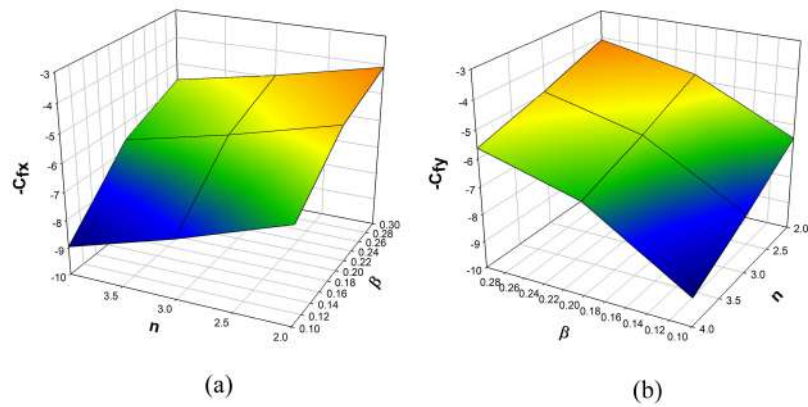


Figure 5.9: (a) Consequence of n and β over C_{fx} , (b) Consequences of n and β over C_{fy}

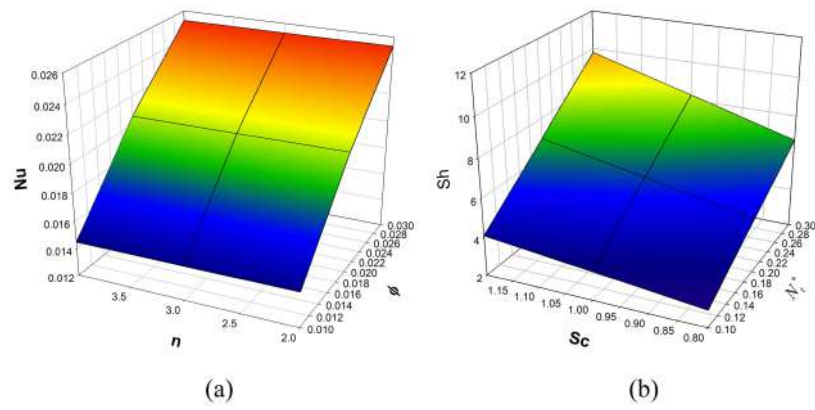


Figure 5.10: (a) Consequence of n and ϕ over Nu , (b) Consequences of Sc and N_t^* over Sh

Table 5.4: Computational values of $f''(0)$, $g''(0)$, $\theta'(0)$ and $\zeta'(0)$ for various dimensionless constraints

n	ϕ	β	Sc	N_t^*	$-f''(0)$	$-g''(0)$	$\theta'(0)$	$-\chi'(0)$
1					0.428707	0.428707	23.723047	2.883644
2					0.576782	0.576782	23.720796	3.072287
3	0.01	0.1	0.8	0.1	0.694439	0.694439	23.718549	3.231165
	0.01				0.694439	0.694439	23.718549	3.231092
	0.02				0.695638	0.695638	34.085641	4.164654
	0.03				0.696469	0.696469	42.056350	4.941831
		0.1			0.694439	0.694469	23.718549	3.231092
		0.2			0.940005	0.940005	23.712475	3.182007
		0.3			1.106068	1.106068	23.707350	3.148383
			0.8		0.694439	0.694439	23.718549	3.231092
			1.0		0.694439	0.694439	23.718549	3.873363
			1.2		0.694439	0.694439	23.718549	4.496217
				0.1	0.694439	0.694439	23.718549	3.231092
				0.2	0.694439	0.694439	23.718549	5.174942
				0.3	0.694439	0.694439	23.718549	7.125058

Chapter 6

MHD flow and melting heat transfer of dusty Casson fluid over a stretching sheet with Cattaneo Christov heat flux model

6.1 Prelude:

This chapter describes the characteristics of magnetohydrodynamics (MHD) flow and melting heat transfer of dusty Casson fluid across a stretching sheet(SS). Through the Cattaneo-Christov heat flux, a modified form of Fourier's law is used. Partial differential equations (PDEs) are used to express the mathematical formulation. The resulting coupled system was examined using the Runge-Kutta-Fehlberg 45 order approach as well as shooting methodology. The coefficients of the Runge-Kutta scheme are required to provide precision and refinement in the results. The influence of flow regulating factors on relevant profiles is analyzed quantitatively and qualitatively to have a thorough understanding of the present situation. The skin friction and heat transfer coefficient computations are shown graphically and tabulated. Because of the melting effect, the temperature and thickness of the thermal boundary layer are larger for the relaxation time parameter.

6.2 Mathematical Elucidation:

Consider a steady flow of an incompressible Casson fluid over a stretching sheet. The flow is assumed to be confined to the region $y > 0$. The flow is generated by the action of two equal and opposite forces along x -axis and y -axis being normal to the flow. A uniform magnetic field of strength B_0 is imposed along the y -axis and the sheet being stretched with the velocity $u_w(x)$ along the x -axis. The number density is assumed to be constant and volume fraction of dust particle is neglected. The fluid and dust particles motion are coupled only through drag and heat transfer between them. The drag force is modeled using Stoke's linear drag theory. Other interaction forces such as the virtual force, the shear lift force and the spin-lift force will be neglected when compared to the drag force. Let T_m be the temperature of the melting surface, while the temperature in the free-stream condition is T_∞ , where $T_\infty > T_m$.

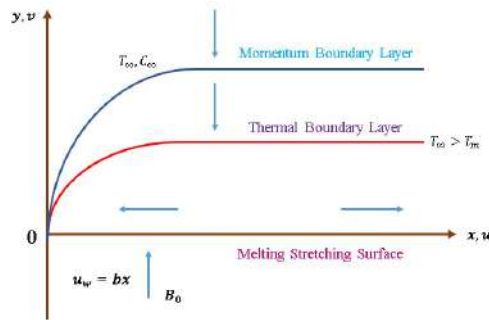


Figure 6.1: Flow Geometry

Governing equations for the defined problem are (See refs[42] and [43]);

$$\frac{\partial u}{\partial x} + \frac{\partial v}{\partial y} = 0, \quad (6.2.1)$$

$$u \frac{\partial u}{\partial x} + v \frac{\partial u}{\partial y} = \nu \left(1 + \frac{1}{\beta} \right) \frac{\partial^2 u}{\partial y^2} + \frac{K_2 N}{\rho} (u_p - u) - \frac{\sigma^* B_0^2}{\rho} u, \quad (6.2.2)$$

$$\frac{\partial u_p}{\partial x} + \frac{\partial v_p}{\partial y} = 0 \quad (6.2.3)$$

$$\rho_p \left(u_p \frac{\partial u_p}{\partial x} + v_p \frac{\partial u_p}{\partial y} \right) = K_2 N (u - u_p) \quad (6.2.4)$$

where $K_2 = 6\pi\mu r_1$ is the Stokes drag coefficient.

The appropriate boundary conditions applicable to the present problem are,

$$\left. \begin{aligned} u &= \left(1 + \frac{1}{\beta} \right) K_3 \frac{\partial u}{\partial y}, & v &= 0 & \text{at } y &= 0, \\ u &\rightarrow 0, & u_p &\rightarrow 0, & v_p &\rightarrow v \text{ as } y \rightarrow \infty \end{aligned} \right\} \quad (6.2.5)$$

where $u_w(x) = bx$ is a stretching sheet velocity with $b (> 0)$.

Introduce the following similarity transformations,

$$\left. \begin{aligned} u &= bx f'(\eta), & v &= -\sqrt{\nu b} f(\eta), & \eta &= \sqrt{\frac{b}{\nu}} y, \\ u_p &= bx F'(\eta), & v_p &= -\sqrt{\nu b} F(\eta), \end{aligned} \right\} \quad (6.2.6)$$

The equations (6.2.1) and (6.2.3) are identically satisfied, in terms of relations (6.2.6). In addition, the equation (6.2.2) and (6.2.4) are reduced into the following set of non-linear ordinary differential equations,

$$\left(1 + \frac{1}{\beta} \right) f''''(\eta) - [f'(\eta)]^2 + f''(\eta)f(\eta) + l \beta_v [F'(\eta) - f'(\eta)] - M f'(\eta) = 0, \quad (6.2.7)$$

$$F(\eta) F''(\eta) - [F'(\eta)]^2 + \beta_v [f'(\eta) - F'(\eta)] = 0. \quad (6.2.8)$$

Transformed boundary conditions are,

$$\left. \begin{aligned} f'(\eta) &= \left(1 + \frac{1}{\beta}\right) A f''(0), & f(\eta) &= 0 & \text{at } (\eta) &= 0, \\ f'(\eta) &\rightarrow 0, & F'(\eta) &\rightarrow 0, & F'(\eta) &\rightarrow f(\eta), & \text{as } \eta \rightarrow \infty \end{aligned} \right\} \quad (6.2.9)$$

where $l = \frac{Nm}{\rho}$ is the mass concentration parameter of dust particles, $M = \frac{\sigma B_0^2}{\rho b}$ is the magnetic parameter, $\beta_v = \frac{1}{b\tau_v}$ is the fluid-particle interaction parameter for velocity, $\tau_v = \frac{m}{K}$ is the relaxation time of the dust particles and $A = K_3 \sqrt{\frac{b}{\nu}}$ is the velocity slip parameter.

6.3 Heat Transfer Analysis

The governing boundary layer heat transport equations for both fluid and dust phase are given by

$$\begin{aligned} c_p \rho \left(u \frac{\partial T}{\partial x} + v \frac{\partial T}{\partial y} \right) + \lambda \left(u \frac{\partial u}{\partial x} \frac{\partial T}{\partial x} + v \frac{\partial v}{\partial y} \frac{\partial T}{\partial y} + u \frac{\partial v}{\partial x} \frac{\partial T}{\partial y} + v \frac{\partial u}{\partial y} \frac{\partial T}{\partial x} \right) \\ + \lambda \left(2uv \frac{\partial^2 T}{\partial x \partial y} + u^2 \frac{\partial^2 T}{\partial x^2} + v^2 \frac{\partial^2 T}{\partial y^2} \right) = k \frac{\partial^2 T}{\partial y^2} + \frac{\rho_p c_p}{\tau_T} (T_p - T) + \frac{\rho_p}{\tau_v} (u_p - u)^2 \end{aligned} \quad (6.3.1)$$

$$u_p \frac{\partial T_p}{\partial x} + v_p \frac{\partial T_p}{\partial y} = -\frac{C_p}{c_m \tau_T} (T_p - T), \quad (6.3.2)$$

Corresponding boundary conditions for the temperature are considered as follows:

$$\left. \begin{aligned} T &= T_m, & k \left(\frac{\partial T}{\partial y} \right)_{y=0} &= \rho [E + C_s (T_m - T_0)] v(x, 0) & \text{at } y &= 0 \\ T &\rightarrow T_\infty, & T_p &\rightarrow T_\infty, & & \text{as } y \rightarrow \infty \end{aligned} \right\} \quad (6.3.3)$$

Equation (6.3.3) states that the heat conducted to the melting surface is equal to the heat of melting plus the sensible heat required to raise the solid temperature T_0 to its melting temperature T_m .

The dimension of fluid phase temperature $\theta(\eta)$ and dust phase temperature $\theta_p(\eta)$ are defined as;

$$\theta(\eta) = \frac{T - T_m}{T_\infty - T_m}, \quad \theta_p(\eta) = \frac{T_p - T_m}{T_\infty - T_m} \quad (6.3.4)$$

Using (6.3.4) in (6.3.1) and (6.3.2), one can get the following non-linear ordinary differential equations,

$$\begin{aligned} \theta''(\eta) + Pr\theta'(\eta)f(\eta) + lPr\beta_t(\theta_p(\eta) - \theta(\eta)) - Pr\Gamma \left[\begin{array}{l} f(\eta)f'(\eta)\theta'(\eta) \\ + f(\eta)^2\theta''(\eta) \end{array} \right] \\ + \beta_v l EcPr [F'(\eta) - f'(\eta)]^2 = 0, \end{aligned} \quad (6.3.5)$$

$$\theta'_p(\eta)F(\eta) - \gamma_2\beta_t[\theta_p(\eta) - \theta(\eta)] = 0 \quad (6.3.6)$$

The corresponding boundary conditions becomes;

$$\left. \begin{array}{l} Prf(0) + M_E\theta'(0) = 0, \quad \theta(\eta) = 0 \quad \text{at} \quad \eta = 0, \\ \theta(\eta) \rightarrow 1, \quad \theta_p(\eta) \rightarrow 1 \quad \text{as} \quad \eta \rightarrow \infty, \end{array} \right\} \quad (6.3.7)$$

where, $Pr = \frac{\mu C_p}{k}$, $Ec = \frac{u_w^2}{C_p(T_w - T_\infty)}$, $\gamma_2 = \frac{C_p}{C_m}$, $\Gamma = \lambda b$, $\beta_t = \frac{1}{b\tau_T}$.

The dimensionless melting parameter which is defined as

$$M_E = \frac{C_f(T_\infty - T_m)}{\lambda + C_s(T_m - T_0)}$$

which is a combination of the Stefan numbers $\frac{C_f(T_\infty - T_m)}{\lambda}$ and $\frac{C_s(T_m - T_0)}{\lambda}$ for the liquid and solid phases respectively.

The physical quantities of interest like skin friction coefficient (C_{fx}) and local Nusselt number (Nu_x) are defined as,

$$C_{fx} = \frac{\tau_w}{\rho u_w^2} \quad \text{and} \quad Nu_x = \frac{u_w q_w}{ak(T_\infty - T_w)}$$

where the shear stress (τ_w) and surface heat flux (q_w) are given by;

$$\tau_w = \left(\mu_0 \left(1 + \frac{1}{\beta} \right) \frac{\partial u}{\partial y} \right)_{y=0} \quad \text{and} \quad q_w = (q_r)_{y=0}.$$

Using the non-dimensional variables, one can get;

$$\sqrt{Re_x} C_f = \left[1 + \frac{1}{\beta} \right] f''(0) \quad \text{and} \quad \frac{Nu_x}{\sqrt{Re_x}} = -\theta'(0).$$

6.4 Method of Numerical Extraction:

The set of nonlinear ordinary differential equations (6.2.7), (6.2.8), (6.3.5) and (6.3.6) along with the boundary conditions (6.2.9) and (6.3.7) are solved numerically using Runge-Kutta based shooting method. Initially, the set of nonlinear ordinary differential equations are converted to first order differential equations, by using the following procedure;

$$f = y_1, \quad f' = y_2, \quad f'' = y_3, \quad F = y_4, \quad F' = y_5.$$

$$y_3' = \frac{1}{\left(1 + \frac{1}{\beta} \right)} \left[y_2^2 - y_1 y_3 - l \beta_v (y_5 - y_2) + M y_2 \right], \quad (6.4.1)$$

$$y_5' = \frac{1}{y_4} \left[y_5^2 - \beta_v (y_2 - y_5) \right], \quad (6.4.2)$$

$$\theta = y_6, \quad \theta' = y_7, \quad \theta_p = y_8.$$

$$y_7' = \frac{1}{1 - Pr \Gamma y_1^2} \left[[Pr \Gamma y_1 y_2 y_7 - Pr y_1 y_7 - Pr l \beta_t (y_8 - y_6) + Pr l \beta_v Ec (y_5 - y_2)^2] \right], \quad (6.4.3)$$

$$y_8' = \frac{1}{y_4} \left[\gamma_2 \beta_t (y_8 - y_6) \right], \quad (6.4.4)$$

with the corresponding boundary conditions;

$$\left. \begin{aligned} Pr y_1 + M_E y_7 = 0, \quad y_2 = \left(1 + \frac{1}{\beta} \right) A y_3, \quad y_6 = 0 \quad \text{and} \quad y_1 = 0 \quad \text{at} \quad \eta = 0, \\ y_2 = 0, \quad y_5 \rightarrow 0, \quad y_4 \rightarrow y_1 \quad y_6 \rightarrow 1, \quad y_8 \rightarrow 0 \quad \text{as} \quad \eta \rightarrow \infty, \end{aligned} \right\} \quad (6.4.5)$$

To solve the equations (6.4.1) - (6.4.4), we guess the values of y_3 , y_5 , y_7 and y_8 which are not given as the initial conditions. Once all initial conditions are found then we solve the equations (6.4.1) - (6.4.4) by using Runge-Kutta fourth order method with the successive iterative step length of 0.01. The non-dimensional velocity and temperature profiles are shown in Figs. 6.2-6.15 for several values of different physical parameters. To validate the employed method, the authors have compared the results of $f''(0)$ with published work. These comparisons are given in Table 6.1 and it shows that the results are in very good agreement.

Table 6.1: **Comparison values of skin friction co-efficient** ($\beta = 0$)

M	<i>Akbar et al.</i> [80]	<i>Present Result</i>
1	-1.41421	-1.41421
5	-2.44948	-2.44949
10	-3.31662	-3.31662
50	-7.14142	-7.14143
500	-22.3830	-22.38302
1000	-31.6386	-31.63858

6.5 Deliberation of Results:

The main goal of this work is to initiate the study of boundary layer flow and melting heat transfer of Casson fluid over a stretching surface in the presence of fluid particles suspension, melting effect, Cattaneo-Christov heat flux and Slip effect. We have considered the values of dimensionless parameters as $\beta = 0.5$, $M = 0.5$, $\beta_v = 0.5$, $l = 0.5$, $\beta_t = 0.5$, $\gamma = 0.8$, $Pr = 5$, $Ec = 0.5$, $M_E = 0.5$, $A = 0.5$ and $\Gamma = 0.6$. These values have been taken as common for the complete study in the figures and tables.

Fig. 6.2 is plotted to show the variations of velocity profile of both fluid and dust phases for different values of magnetic parameter (M). From this plot, it is observed that velocity profiles and their associated momentum boundary layer thickness reduce for the enhancement of magnetic parameter. This is due to the fact that the Lorentz force has the property to slow down the motion of the conducting fluid in the boundary layer.

Fig. 6.3 is portrayed to investigate the influence of the Casson parameter (β) on velocity distributions. It is found that an increase in the Casson parameter leads to decrease in velocity profile and momentum boundary layer thickness. This is due to the fact that an increase in β leads to an increase in dynamic viscosity that induces resistance in the flow of fluid and decrease in fluid velocity is observed.

Fig. 6.4 is plotted to examine the influence of slip parameter (A) on velocity profile for both fluid and dusty phases. From this figure it is observed that, the depreciation in the velocity profile and momentum boundary layer thickness for increasing values of slip parameter. This may happen due to frictional resistance between the surface and fluid particle increases and as a result the velocity of the fluid decreases.

Fig. 6.5 and Fig. 6.6 explain the effect of β_v and β_t on velocity and temperature profiles, respectively. An increase in β_v will decrease fluid phase velocity and increase dust phase velocity. As expected, increase in β_t will increase fluid phase temperature, and decrease the dust phase temperature. This is because increase in β_v results in decrease of τ_v , and it is obvious that the time required by dust particle to adjust its velocity relative to the fluid also decreases with decrease in τ_v .

The variation of velocity and temperature profiles for both the phases are illustrated for different values of mass concentration parameter (l), and are shown in Fig. 6.7 and Fig. 6.8 respectively. Here, the velocity profile for both the phases decreases for increasing values

of mass concentration parameter, and the opposite trend is observed for temperature profiles.

Fig. 6.9 illustrates the influence of melting parameter (M_E) on the temperature profile. An increase in the melting parameter reduces the temperature of both fluid and dust phases and also decreases the thermal boundary layer thickness. This is because an increase in M_E will increase the intensity of melting as well the melting progresses. Hence, the sheet gradually transforms to a liquid, causing the temperature of the fluid decreases rapidly.

Fig. 6.10 describes the impact of Prandtl number over the temperature profile. One can infer from this figure that, in the presence of melting parameter, an increase in Prandtl number increases the temperature of both fluid and dust phases.

Fig. 6.11 and Fig. 6.12 are plotted to understand the influence of Eckert number (Ec) and specific heat ratio parameter (γ_2) on temperature profile respectively. As anticipated, the temperature profile and thermal boundary layer thickness for both fluid and dust phases increase with increasing values of Ec , and this is shown in Fig. 6.11. From the Fig. 6.12, one can see that the thermal boundary layer thickness and temperature profile for both fluid and dust phase increases by increasing (γ_2).

Fig. 6.13 is illustrating the variation of relaxation time parameter (Γ) on temperature profile for both fluid and dusty phases. One can see from this figure that, the temperature profile and thermal boundary layer thickness increases by ascent values of relaxation time parameter. Physically, it confirms that incremental nature of thermal relaxation time parameter requires more time to shift the heat from intensively packed fluid particles to the low energetic fluid particles. Thus, an increment in temperature profile is noted in both fluid and dust phases.

Fig. 6.14 specifically plotted for variation in the skin friction coefficient against the incremental values of M and β . A mixed trend is noted as plotted in the respective figure. Here increase in the skin friction coefficient is noted for higher values of M , while a reverse trend is observed for higher values of β . The result is plotted in Fig. 6.15 shows the variation noted in Nusselt number for incremental values of Pr and Ec . From this figure it is clear that, a diminution in local Nusselt number is witnessed with incremental values of Pr and Ec .

Table 6.2 and Table 6.3 displayed the variation of skin friction coefficient and Nusselt number for different values of physical parameter. From the Table 6.2, it is reported that, the skin friction coefficient is a decreasing function of M_E and A . Additionally, the skin friction coefficient increases while M , β_v , l and β are enhancing. Table 6.3 shows the variation of Nusselt number on different physical parameter. From this table, we can observe that, the higher values of Pr , Ec , Γ and β_t decreases the Nusselt number, while an opposite trend is observed with higher values of M_E

6.6 Inference:

The two-dimensional flow of dusty Casson fluid over a stretching sheet with Cattaneo-Christov heat flux, slip and melting effect has been discussed. Firstly, the partial differential equations are transmuted in to ordinary differential equations by implementing similarity approach. Afterwards, the solutions of attained equations are solved by implementing Runge-Kutta-Fehlberg-45 method. The following points of conclusions have been derived;

- Increasing values of M and β shows reduction in the velocity profile for both fluid

and dust phases.

- Due to the melting effect, the larger Pr shows increment in temperature profile for both fluid and dusty phases.
- Larger values of Ec and γ_2 leads to higher temperature profile for both fluid and dusty phases.
- An increment in Γ leads to higher temperature profile for both fluid and dusty phases.
- Increasing strength of A causes decay in the velocity profile for both fluid and dust phases.
- Increasing values of β_v leads to higher dust phase velocity while opposite trend is noticed for fluid phase velocity.
- Increment in l results in declination of the velocity and temperature profiles for both the phases.

Table 6.2: Numerical values of skin friction coefficient for different physical parameters

M	β_v	l	β	M_E	A	$-\sqrt{Re_x}C_{fx}$
0.1						0.410932
0.3						0.427367
0.5						0.435748
	0.1					0.421977
	0.2					0.427819
	0.3					0.431932
		0.2				0.801624
		0.4				0.810827
		0.6				0.811294
			0.2			0.318926
			0.4			0.365201
			0.6			0.389585
				0.5		1.091940
				1.0		1.060842
				1.5		1.041257
					0.3	0.811318
					0.5	0.680443
					0.7	0.587919

Table 6.3: Numerical values of Nusselt number for different physical parameters

Pr	E_c	Γ	β_t	M_E	$\frac{Nu_x}{\sqrt{Re_x}}$
0.5					0.621143
1.0					0.904414
1.5					1.128768
	0.2				0.148970
	0.4				0.156271
	0.6				0.159942
		0.01			1.640947
		0.1			1.758423
		0.2			1.824231
			0.1		0.914002
			0.3		0.994512
			0.5		1.023451
				0.5	1.394821
				1.0	1.148760
				1.5	1.063482

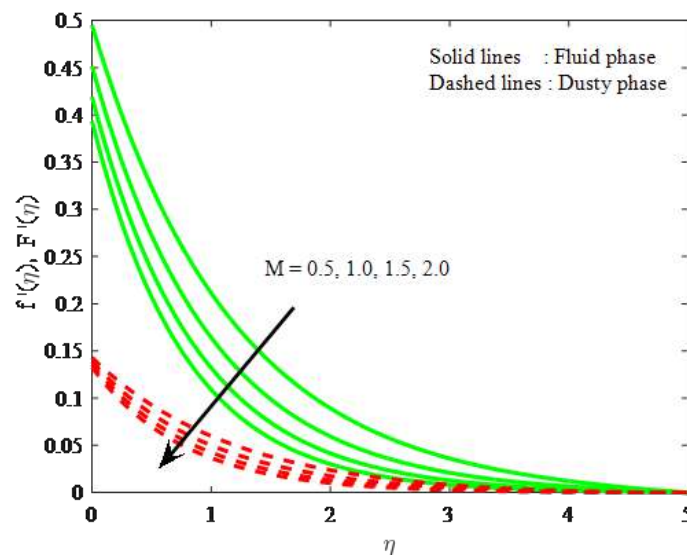


Figure 6.2: Effect of magnetic parameter on velocity profile for both fluid and dust phases

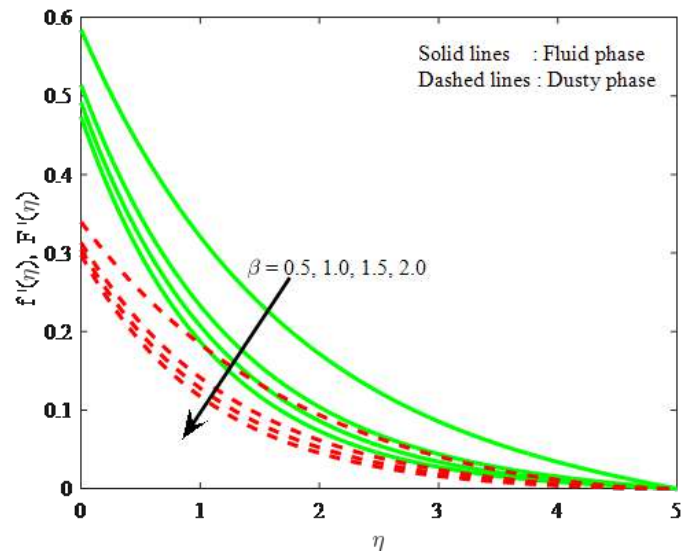


Figure 6.3: Effect of Casson parameter on velocity profiles for both fluid and dust phases

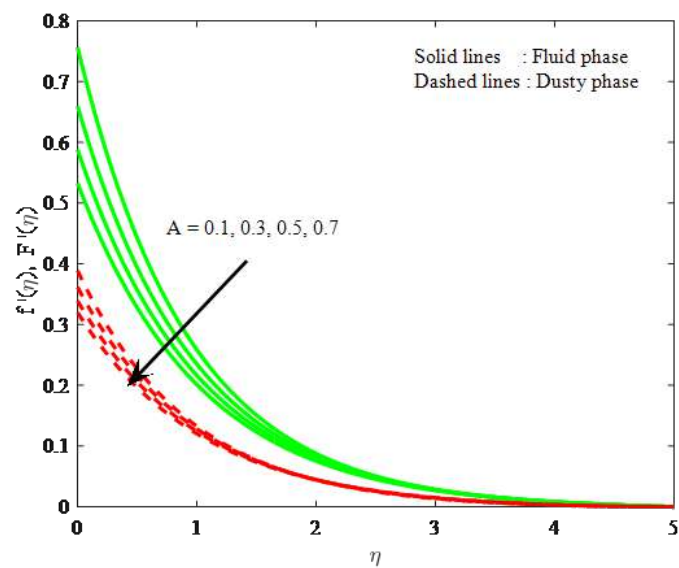


Figure 6.4: Effect of velocity slip parameter on velocity profiles for both fluid and dust phases

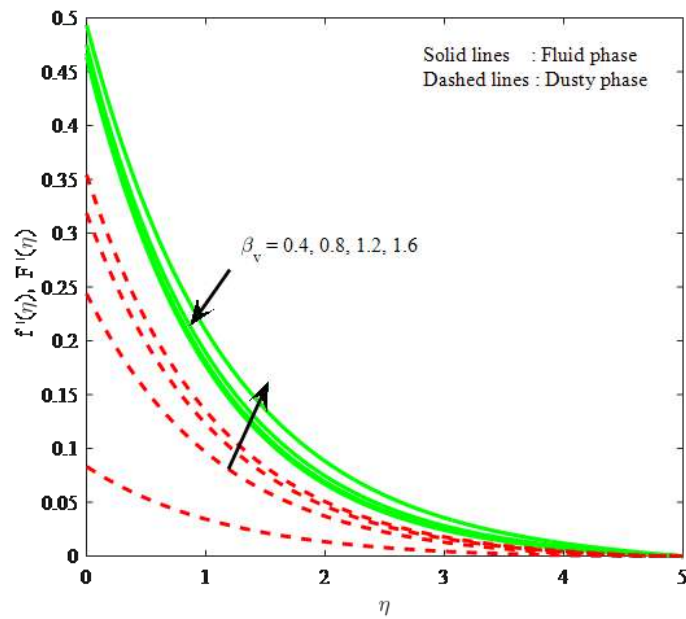


Figure 6.5: Effect of β_v on velocity profiles for both fluid and dust phases.

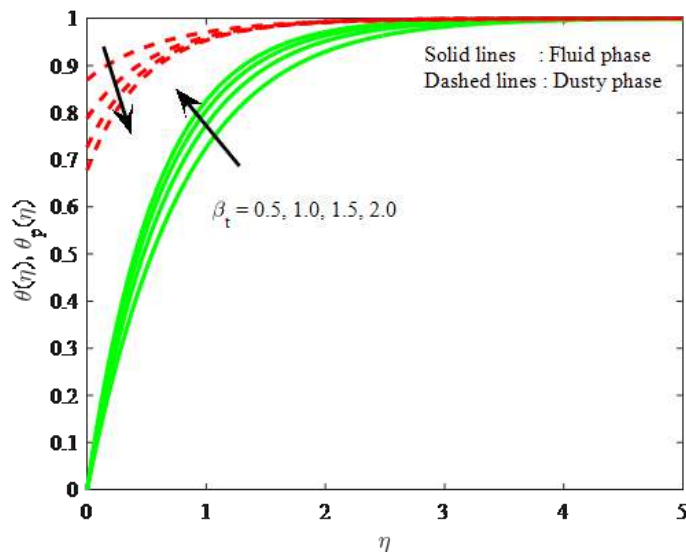


Figure 6.6: Effect of β_t on velocity profiles for both fluid and dust phases

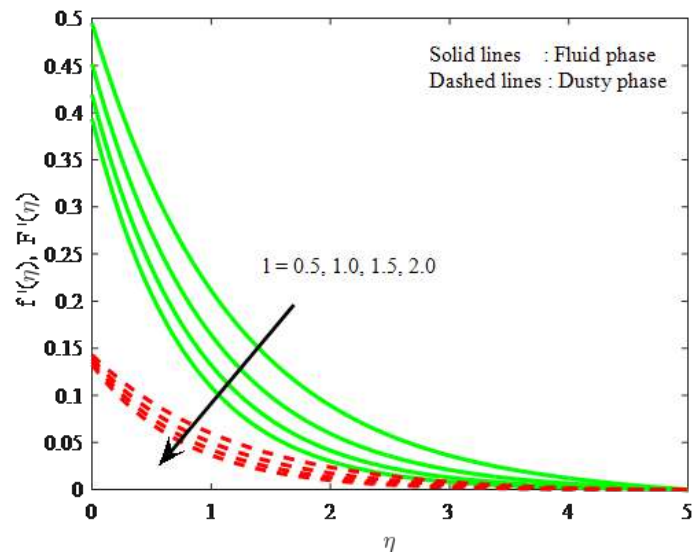


Figure 6.7: Effect of mass concentration parameter on velocity profiles for both fluid and dust phases

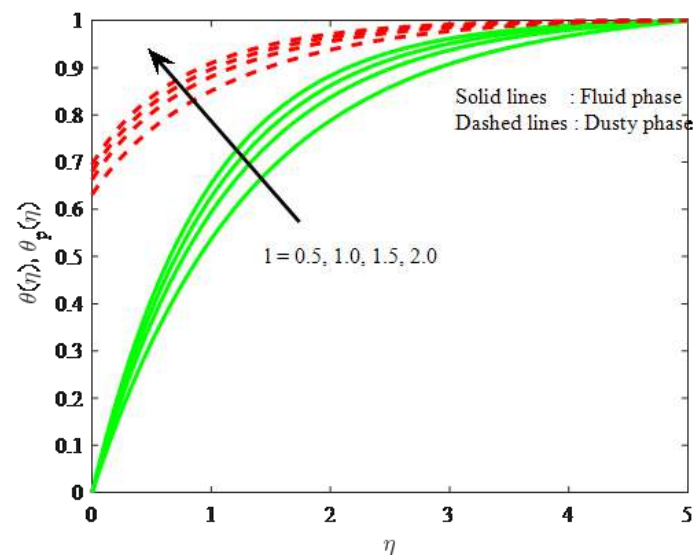


Figure 6.8: Effect of mass concentration parameter on temperature profiles for both fluid and dust phases

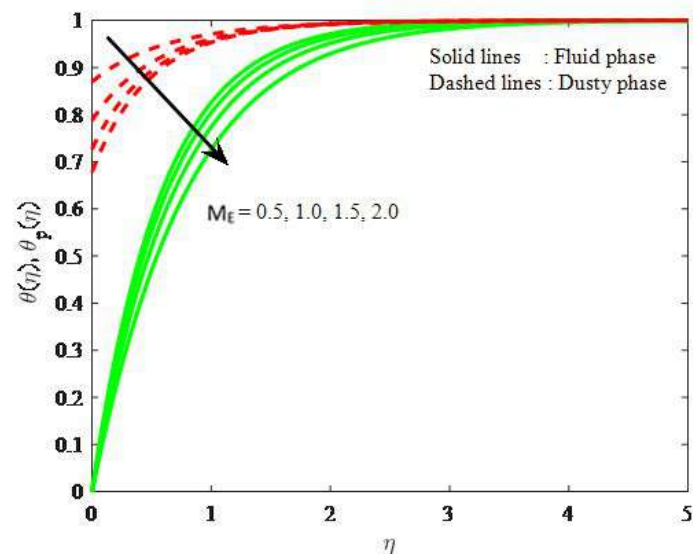


Figure 6.9: Effect of melting parameter on temperature profiles for both fluid and dust phases.

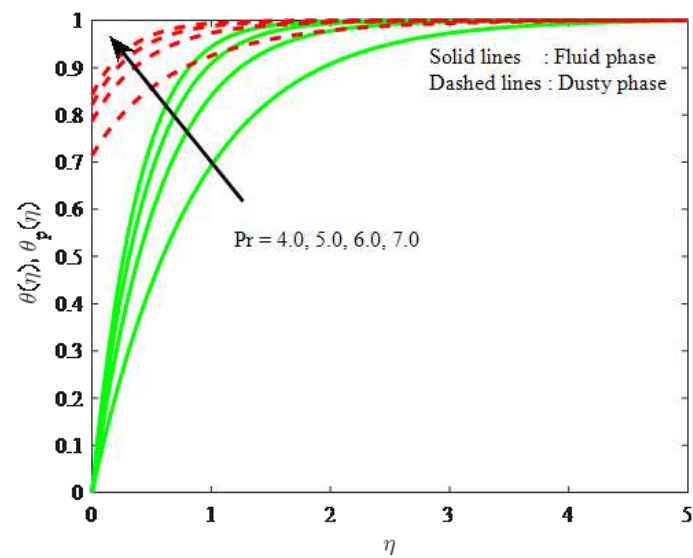


Figure 6.10: Effect of mass prandtl number on temperature profiles for both fluid and dust phases..

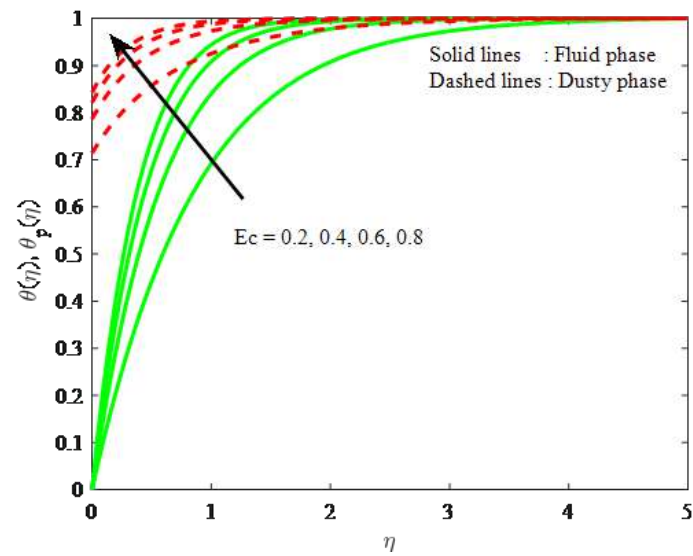


Figure 6.11: Effect of Eckert number on temperature profiles for both fluid and dust phases..

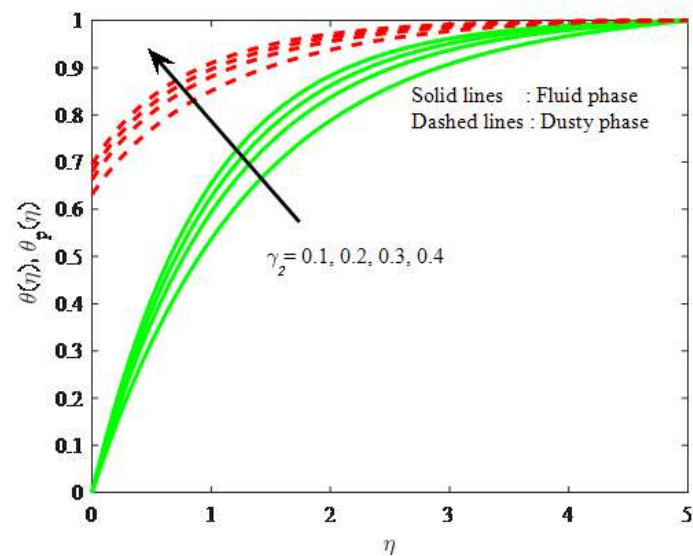


Figure 6.12: Effect of mass specific heat ratio parameter on temperature profiles for both fluid and dust phases.

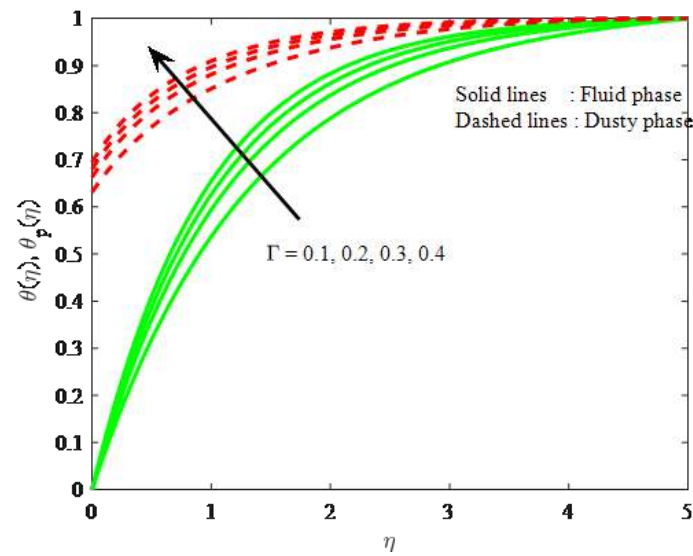


Figure 6.13: Effect of mass relaxation time parameter on temperature profiles for both fluid and dust phases..

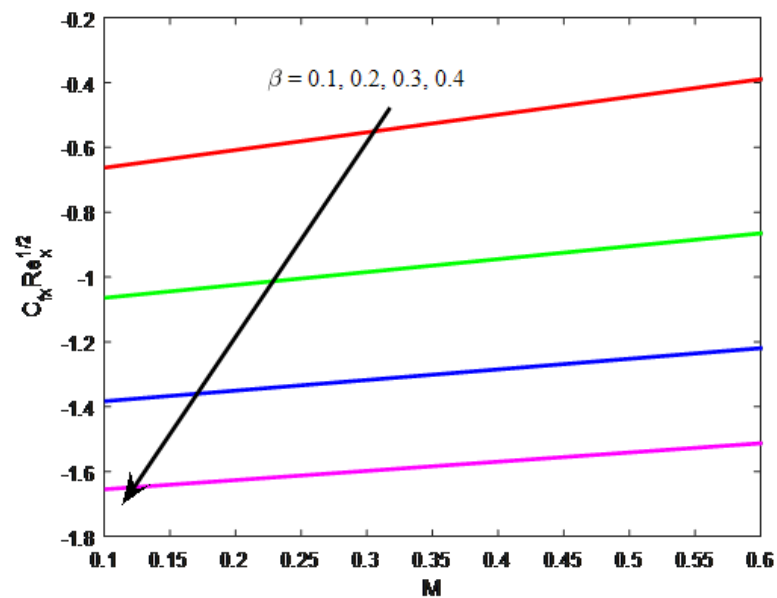


Figure 6.14: Effect of β and M on skin friction coefficient.

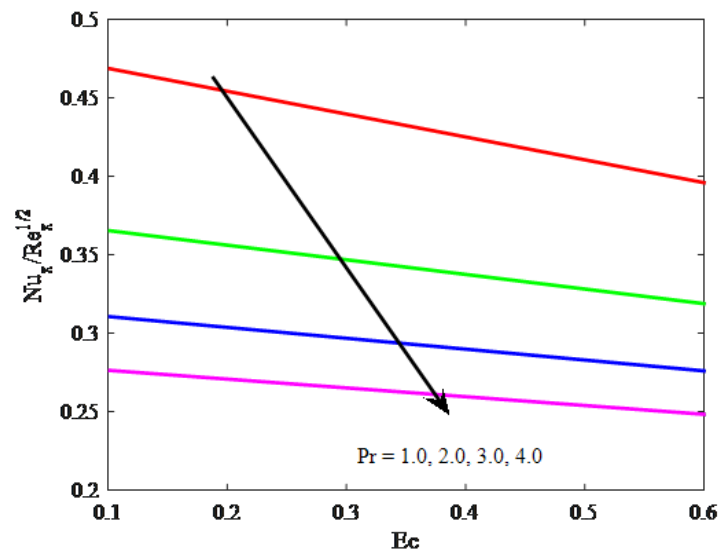


Figure 6.15: effect of Pr and Ec on local Nusselt number

Chapter 7

Particle shape effect on MHD Water Functionalized Al_2O_3 nanoparticles steady flow over Wedge

7.1 Prelude:

The goal of this chapter is to investigate the effects of Alumina (Al_2O_3) nanoparticle morphologies on magnetohydrodynamic (MHD) steady flow of Maxwell liquid via a wedge with nonlinear thermal radiation influence. A fluctuating magnetic field is supplied to the wedge surface in a normal direction. The influence of the Cattaneo-Christove heat flow is also taken into account in the modelling. The Runge Kutta Fehlberg fourth fifth order (RKF-45) numerical method is used in conjunction with the shooting approach to convert the basic equations into ordinary differential equations (ODEs). For increase in the values of the thermal relaxation time parameter, the copy of the output declares that platelet shaped nanoparticles have greater heat transfer enhancement and that the rate of decline in heat transport is quicker for the brick scenario.

7.2 Mathematical Elucidation:

Consider a two-dimensional flow of an incompressible Maxwell nanofluid suspended with Al_2O_3 nanoparticles of different shapes past a wedge with an included angle $\Omega = \beta_w \pi$. Flow geometry is displayed in Fig.7.1. Here β_w is the measure of pressure gradient. A negative value of β_w indicates the positive pressure gradient and pressure gradient is negative or favourable for positive value of β_w . Further, relation between wedge angle parameter and pressure gradient is given as $m = \frac{\beta_w}{2-\beta_w}$. Here the physical significance of the m values follow as (see refs. [81-82]). $m = 0$ for Blasius solution, $m > 0$ denote the pressure gradient, $m < 0$ denotes that the adverse pressure gradient, $m = 1$ corresponding to stagnation point flow. The governed equation under these assumptions can be written as follows (see refs. [83-84]):

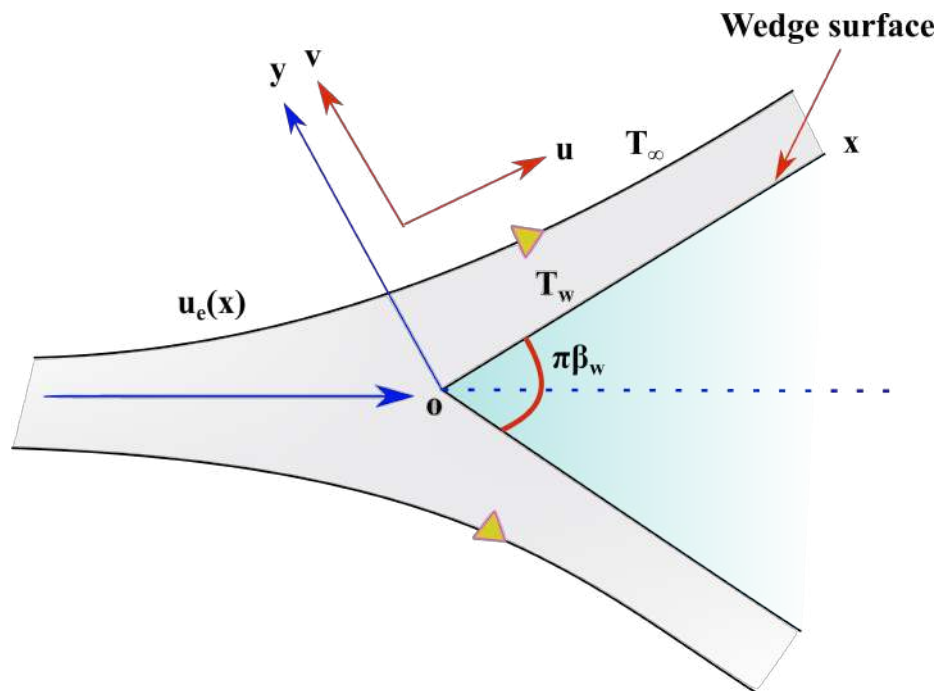


Figure 7.1: Flow Geometry

$$\frac{\partial u}{\partial x} + \frac{\partial v}{\partial y} = 0, \quad (7.2.1)$$

$$\begin{aligned} u \frac{\partial u}{\partial x} + v \frac{\partial u}{\partial y} &= \frac{\mu_{nf}}{\rho_{nf}} \left(\frac{\partial^2 u}{\partial y^2} \right) + u_e \frac{d\mu_e}{dx} - \frac{B_0^2 \sigma_{nf}^*}{\rho_{nf}} \left(u - u_e + \lambda_1 v \frac{\partial u}{\partial y} \right) \\ &\quad - \lambda_1 \left(u^2 \frac{\partial^2 u}{\partial x^2} + v^2 \frac{\partial^2 u}{\partial y^2} + 2uv \frac{\partial^2 u}{\partial x \partial y} \right) \end{aligned} \quad (7.2.2)$$

$$\begin{aligned} u \frac{\partial T}{\partial x} + v \frac{\partial T}{\partial y} &= \alpha_{nf} \frac{\partial^2 T}{\partial y^2} + \frac{16\sigma^{**} T_\infty^3}{(\rho C_p)_{nf} 3k^{**}} \frac{\partial^2 T}{\partial y^2} \\ &\quad - \lambda_1^* \left[\begin{aligned} &u^2 \frac{\partial^2 T}{\partial x^2} + v^2 \frac{\partial^2 T}{\partial y^2} + 2uv \frac{\partial^2 T}{\partial x \partial y} + \\ &\left(u \frac{\partial u}{\partial x} + v \frac{\partial v}{\partial y} \right) \frac{\partial T}{\partial x} + \left(u \frac{\partial v}{\partial x} + v \frac{\partial u}{\partial y} \right) \frac{\partial T}{\partial y} \end{aligned} \right] \end{aligned} \quad (7.2.3)$$

where the conditions are;

$$\left. \begin{aligned} &u = 0, \quad v = 0, \quad T = T_w, \quad \text{at } y = 0, \\ &u \rightarrow u_e, \quad T \rightarrow T_\infty, \quad \text{as } y \rightarrow \infty. \end{aligned} \right\} \quad (7.2.4)$$

The thermophysical properties of water and Al_2O_3 along with different shapes of nanoparticles are tabulated in Table 7.1 and Table 7.2. The viscosity, electrical conductivity, density, heat capacity and the thermal conductivity of the nanofluid are defined as follows (see refs. [85]);

$$\mu_{nf} = \frac{\mu_f}{(1 - \phi)^{2.5}},$$

$$\sigma_{nf}^* = \sigma_f^* \left(1 + \frac{3 \left(\frac{\sigma_s^*}{\sigma_f^*} - 1 \right) \phi}{\left(\frac{\sigma_s^*}{\sigma_f^*} + 2 \right) - \left(\frac{\sigma_s^*}{\sigma_f^*} - 1 \right) \phi} \right),$$

$$\rho_{nf} = (1 - \phi)\rho_f + \phi\rho_s,$$

$$(\rho C_p)_{nf} = (1 - \phi) (\rho C_p)_f + \phi (\rho C_p)_s, \quad \text{and}$$

$$\frac{k_{nf}}{k_f} = \frac{k_s + (n - 1)k_f + (n - 1)(k_s - k_f)\phi}{k_s + (n - 1)k_f - (k_s - k_f)\phi}.$$

Table 7.1: **Thermophysical properties of water and Al_2O_3** (see refs. [86-87]):

Model	$\rho(kgm^{-3})$	$k(W/mk)$	$C_p(J/kgK)$	$\sigma^*(\Omega m)^{-1}$
water	997.1	0.613	4179	0.05
Al_2O_3	3970	25	765	1×10^{-10}

 Table 7.2: **Different shapes of nanoparticles** (see refs. [85] and [88]):

Nanoparticle shapes	Aspect ratio	Sphericity	Shape factor
Brick	1:1:1	0.81	3.7
platelet	1 : 1/18	0.52	5.7
Cylinder	1:8	0.62	4.9

where, the potential flow velocity can be written as $u_e = ax^m$. The following non-dimensional transformations will be introduced, making use of the stream function $\psi = \sqrt{\frac{2u_e\nu_f x}{m+1}} f(\eta)$, $\eta = y\sqrt{\frac{(m+1)u_e}{2\nu_f x}}$ and $\theta(\eta) = \frac{T-T_\infty}{T_w-T_\infty}$. then, the velocity components can be expressed as

$$u = \frac{\partial\psi}{\partial y}, \quad v = -\frac{\partial\psi}{\partial x}. \quad (7.2.5)$$

By using Eq. (7.2.5), the Eq.(7.2.1) is satisfied trivially, and the Eq.(7.2.2-7.2.3) reduced to the subsequent set of ODEs as;

$$\left. \begin{aligned} \varepsilon_1 f''' - \frac{2m}{m+1} (f'^2 - 1) + ff'' + 2\frac{\sigma_{nf}}{\sigma_f} \varepsilon_2 M (f' - 1 - \lambda_2 (\frac{m-1}{2} \eta f' f'' + \frac{m+1}{2} f f'')) + \\ \lambda_2 [-2m\frac{m-1}{m+1} (f'^3 - 1) - \frac{m+1}{2} f^2 f''' - (1 - 3m) f f' f'' - \frac{m-1}{2} \eta f'^2 f''] = 0 \end{aligned} \right\} (7.2.6)$$

$$\frac{1}{Pr} \left(\frac{k_{nf}}{k_f} + R \right) \varepsilon_3 \theta'' + f\theta' - \gamma_3 \left[\frac{m+1}{2} f^2 \theta'' - \frac{6}{m+1} \eta f'^2 \theta' + f f' \theta' \right] \quad (7.2.7)$$

where,

$$\varepsilon_1 = \left\{ \frac{1}{(1-\phi)^{2.5}} \right\} \left\{ \frac{1}{(1-\phi) + \phi \frac{\rho_s}{\rho_f}} \right\}, \quad \varepsilon_2 = \left\{ \frac{1}{(1-\phi) + \phi \frac{\rho_s}{\rho_f}} \right\}, \quad \varepsilon_3 = \left\{ \frac{1}{(1-\phi) + \phi \frac{(\rho C_p)_s}{(\rho C_p)_f}} \right\}.$$

along with boundary conditions

$$f'(0) = 0, f'(\infty) \rightarrow 1, f(0) = 0, \theta(0) = 1, \theta(\infty) \rightarrow 0, \quad (7.2.8)$$

where,

$$M = \frac{B_0^2 \sigma_f}{\rho_f a x^{m-1}}, \quad \lambda_2 = a \lambda_1 x^{m-1}, \quad \text{Pr} = \frac{\mu_f C_p}{k_f}, \quad R = \frac{16 \sigma^{**} T_\infty^3}{3 k^{**} k_f}, \quad \text{Re}_x = \frac{u_e x}{\nu_f}.$$

The expression for local skin-friction coefficient and local Nusselt number (see ref [83]):

$$C_f \text{Re}_x^{\frac{1}{2}} = \left\{ \frac{1}{(1-\phi)^{2.5}} \right\} \sqrt{\frac{m+1}{2}} f''(0), \quad (7.2.9)$$

$$\text{NuRe}_x^{-\frac{1}{2}} = - \left(\frac{k_{nf}}{k_f} + R \right) \sqrt{\frac{m+1}{2}} \theta'(0). \quad (7.2.10)$$

7.3 Method of Numerical Extraction:

The approach of accompanied nonlinear ODEs (7.2.6) and (7.2.7) along with the boundary constraints (7.2.8) is resolved numerically via RKF45 Method through shooting procedure. The competence of this technique is heightened due to the depletion of computational time. Missed initial circumstances are estimated with the aid of shooting method. This method is an iterative procedure that tries to find appropriate beginning conditions for a relevant IVP that solves the original BVP. At a high but finite value of η , we considered the infinity condition. Integration is performed using the RKF-45 technique when a finite value for η_∞ is determined. If the right step size h is chosen, this approach includes a mechanism for determining an accurate answer. Two distinct approximations for the answer are created and compared at each stage. If the two outcomes are almost same, the estimates are acceptable; if not, the step size is adjusted until the desired precision is achieved. For the existing issue, we took step size $\Delta\eta = 0.001$, $\eta_\infty = 5$ and accurateness

to the sixth decimal place. Furthermore, the present study's numerical solutions are compared to previous research, and the results are quite similar (see Table 7.3)

Table 7.3: **Comparison for the value of $f''(0)$ for some reduced cases.**

m	0.0909	0.2000	0.3333
Yih[89]	0.654979	0.802125	0.927653
Khan and Pop [90]	0.655000	0.802100	0.927700
Kasmani et al.[91]	0.65498	0.80213	0.802897
Asmadi et al.[83]	0.655053	0.92765	0.927739
Present results	0.655054	0.92767	0.927740

7.4 Deliberation of Results:

The crucial theme of this study is to confer the paraphernalia of numerous developing constraints at involved fields for three shapes of nanoparticles in fluid flow. The flow structure is shown in a physical sense by numerical simulations of velocity and thermal distributions versus variations in physical restrictions. Figs.7.2-7.9 show the numerical conclusions. Fig.7.2 indicates impact of the M on $\theta(\eta)$ for three different nanoparticle shape effect factors namely, brick, cylinder and platelet. The rise in value of M advances the $\theta(\eta)$. This is for the Lorentz forces which upsurges with the aggrandizement of M . As a consequence, as the Lorentz force increases, more drag is added to the fluid's velocity, which enhances heat transmission. Also, it is viewed that more heat transfer enhancement is seen for platelet shaped nanoparticles. Moreover, the thermal profile for brick case improves slower than the remaining cases. Fig. 7.3 representing the impact of R on $\theta(\eta)$ for three different nanoparticle shape effect factors. Here, inflation of temperature component can be realized for the rising values of R . As a consequence of the increase

in radiative heat, the thermal state of the nanofluid improves, causing the $\theta(\eta)$ to rise. Also, brick shaped nanoparticles have less influence on increasing the temperature profile as compared with other two. Moreover, it is viewed that more heat transfer enhancement is seen for platelet shaped nanoparticles.

Consequence of γ_3 on $\theta(\eta)$ is shown in Fig.7.4 for three different nanoparticle shape effect factors. A declination of $\theta(\eta)$ is remarked for the upsurge in γ_3 values. The relaxation time of the fluid's heat transfer rises as γ_3 increases, delaying the time for the fluid to undergo heat conduction. As a consequence, the thermal boundary layer thins, allowing for quicker heat dissipation. Because the effect is minor, it can be assumed that, the changes in the value of γ_3 have no substantial impact on the thermal boundary layer. Also, brick shaped nanoparticles have less influence on the temperature profile as compared with other two. Moreover, it is viewed that more heat transfer enhancement is seen for platelet shaped nanoparticles and rate of decrease in heat transport is faster for brick case.

Fig. 7.5 representing the impact of λ_2 and M on skin friction. The ratio of fluid relaxation time to deformation time is the local Deborah number for fluid momentum. The fluid's relaxation time grows as λ_2 increases. As a consequence, the skin friction decreases. Variation of Nusselt number for increased values of M and R is exposed in Fig. 7.6 for three different nanoparticle shape effect factors. The growth in values of R improves the heat transport rate but opposite trend is seen for augmented values of M . Furthermore, fluid flow for platelet case shows better-quality heat transport rate for increased R values. The change in Nusselt number for increased values of M and γ_3 is shown in Fig.7.7 for three different nanoparticle shape effect factors. The escalation in values of γ_3 improves the heat transport rate but inverse trend is seen for augmented

values of M . Moreover, fluid flow for platelet case shows better-quality heat transport rate for increased γ_3 values. Fig.7.8 and Fig.7.9 shows the streamline patterns when $M = 0.1$ and $\lambda_2 = 0.03$ respectively. Table.7.4 displays the numerical values for $f''(0)$ with respect to varied λ_2 and M values. Here, the escalating values of λ_2 increases the $f''(0)$ but it declines for augmented M values. Table 7.5 portrays the numerical values for $\theta'(0)$ with respect to varied γ_3 , R and M values. Here, the mounting values of R and M values increases the $\theta'(0)$ but it declines for augmented γ_3 values.

7.5 Inference:

The review of above research includes the study of stream of the Maxwell fluid past a wedge containing platelet, brick and cylinder shaped Al_2O_3 nanoparticles with water as base fluid. Similarity transformation technique has been formulated to reduce the elementary equations into ODEs and are resolved with the assistance of RK4-5 numerical method accompanying shooting technique. The supremacy of nonlinear thermal radiation, magnetic field and other existing parameters are inquired and their out-turn are listed as follows;

- It is viewed that more heat transfer enhancement is seen for assumed fluid flow with the impact of platelet shaped nanoparticles. Moreover, the thermal profile for brick case improves slower than the remaining cases for rising values of M .
- An intensified thermal profile is remarked for the radiation variation.
- More heat transfer enhancement is seen for platelet shaped nanoparticles and rate of decrease in heat transport is faster for brick case for rise in values of γ_3 .

- The increase in R values improves the heat transport rate but inverse trend is seen for augmented values of M . Moreover, fluid flow for platelet case shows better-quality heat transport rate for increased R values.
- The upsurge in γ_3 values improves the heat transport rate but inverse trend is seen for augmented values of M . Moreover, fluid flow for platelet case shows better-quality heat transport rate for increased γ_3 values.

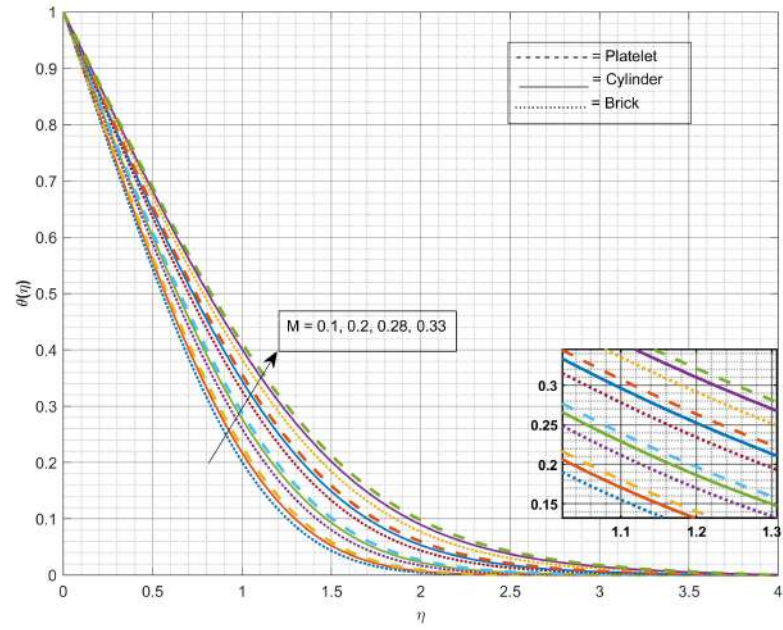


Figure 7.2: Variation of thermal profile for varied M .

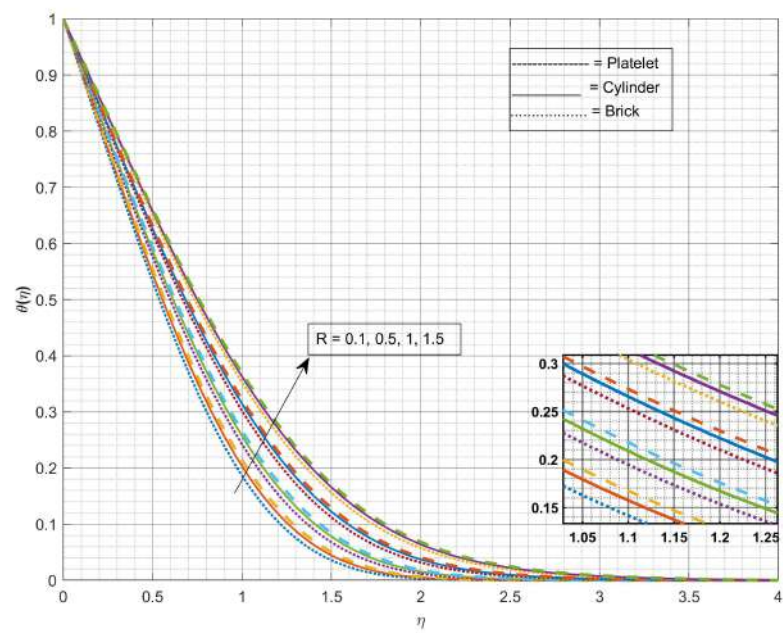


Figure 7.3: Variation of temperature profile for varied R .

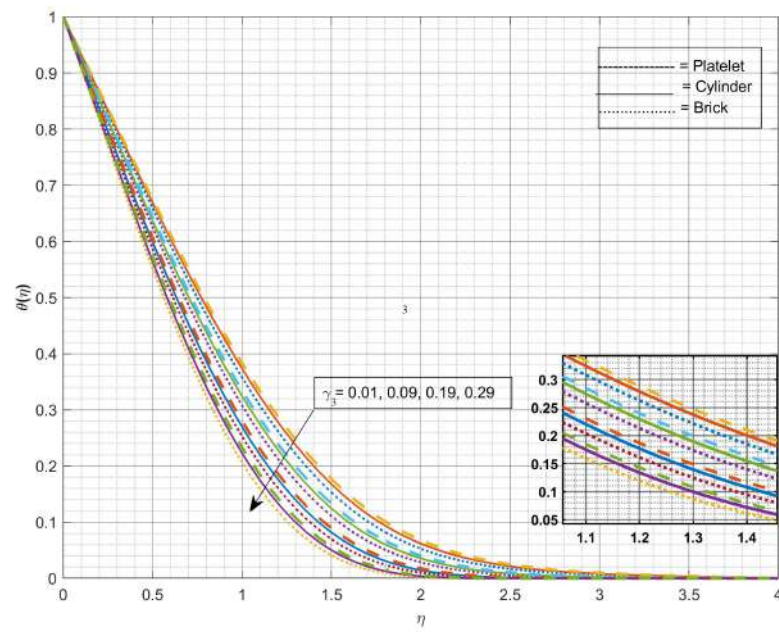


Figure 7.4: Variation of temperature profile for varied γ_3 .

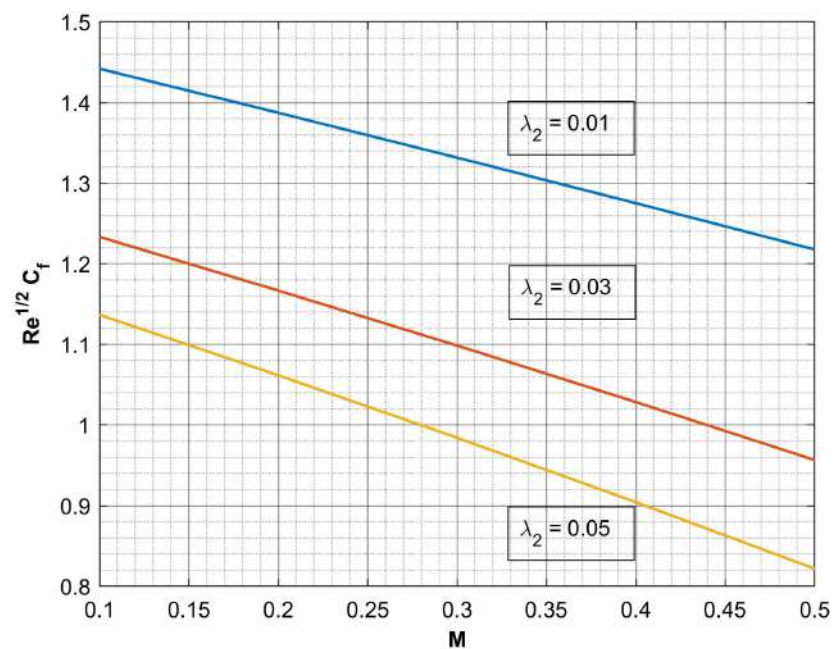


Figure 7.5: Variation of skin friction for varied M and λ_2

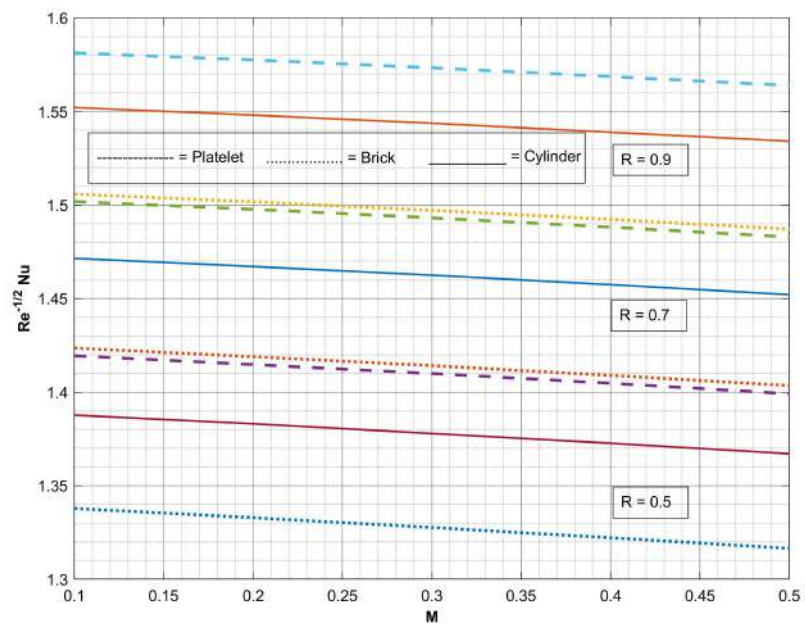


Figure 7.6: Variation of Nusselt number for varied M and R .

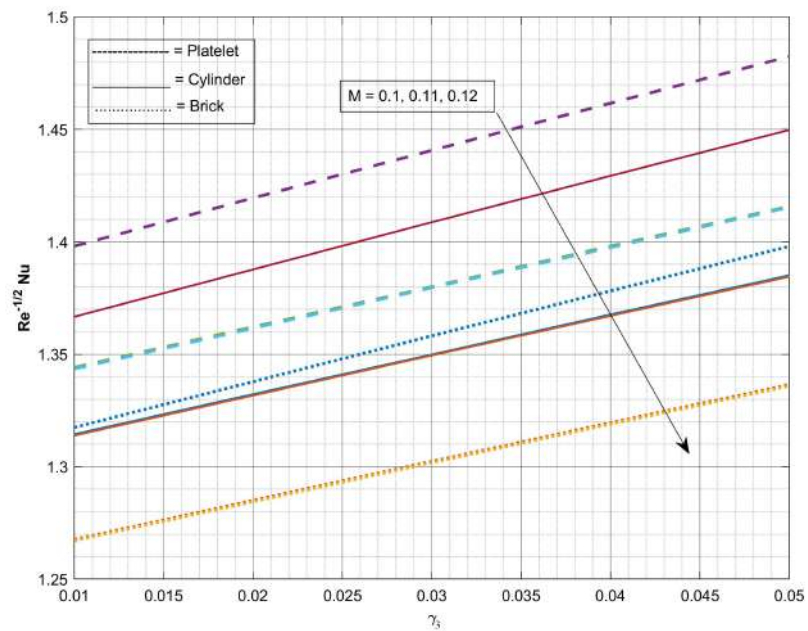


Figure 7.7: Variation of Nusselt number for varied M and γ_3 .

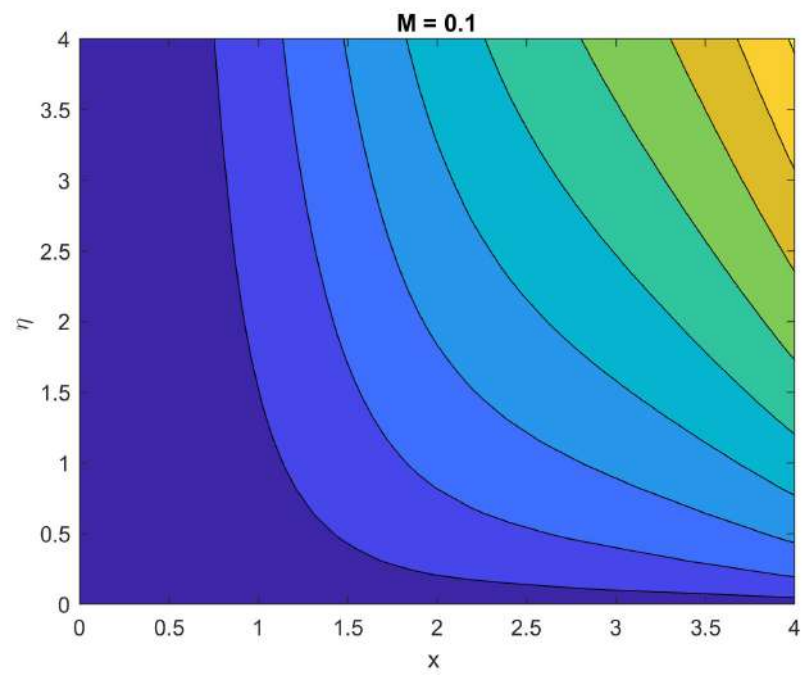


Figure 7.8: Stream lines for $M = 0.1$.

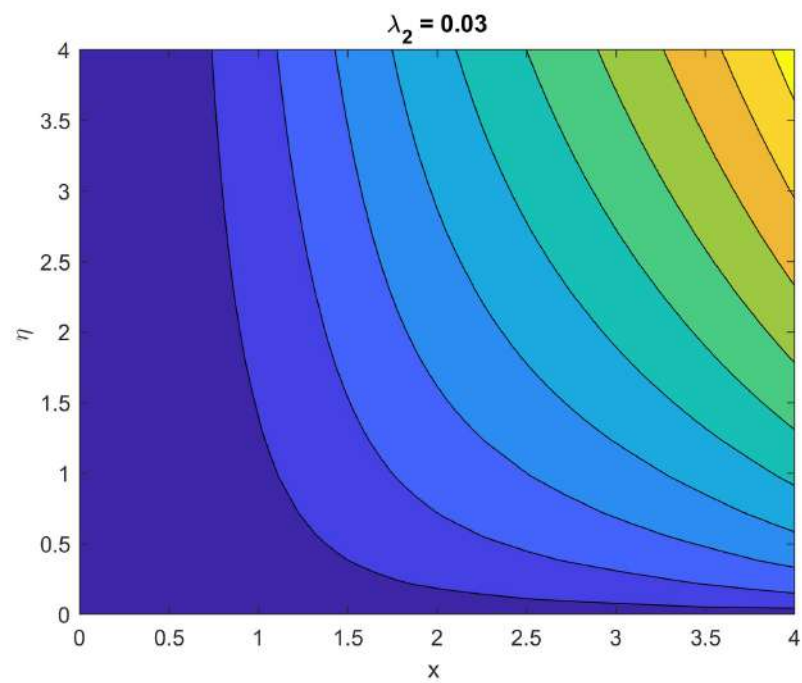


Figure 7.9: Stream lines for $\lambda_2 = 0.03$

Table 7.4: Numerical values for $f''(0)$ with respect to varied λ_2 and M values

λ_2	M	$f''(0)$
0.01	0.1	1.2272
0.02		1.2277
0.03		1.2281
0.04		1.2286
	0.12	1.2142
	0.13	1.2077
	0.14	1.2012

Table 7.5: Numerical values for $\theta'(0)$ with respect to varied γ_3 , R and M values

M	γ_3	R	Platelet	Cylinder	Brick
0.1	0.02	0.5	-0.6836	-0.6932	-0.7092
0.12			-0.6831	-0.6928	-0.7087
0.13			-0.6829	-0.6925	-0.7084
0.14			-0.6827	-0.6923	-0.7082
	0.01		-0.6733	-0.6827	-0.6984
	0.03		-0.6938	-0.7037	-0.72
	0.04		-0.7039	-0.714	-0.7306
		0.1	-0.7419	-0.7548	-0.7765
		0.3	-0.7107	-0.7218	-0.7402
		0.4	-0.6966	-0.707	-0.7241

Chapter 8

Significant consequences of uniform horizontal magnetic field (UHMF) on three-dimensional radiative flow of ZnO-SAE50 nano-lubricant over a porous rotating disk

8.1 Prelude:

The influence of a uniform horizontal magnetic field and thermal radiation on the flow of Zinc Oxide-Society of Automotive Engineers 50 nanolubricant (ZnO-SAE50 nanolubricant) through a porous spinning disk is the main aim of this chapter. Suitable transformations are used to reduce the governing partial differential equations (PDEs) into ordinary differential equations (ODEs). Later, the obtained system is numerically solved using the shooting technique and Runge–Kutta–fourth–fifth Fehlberg’s order approach (RKF-45). The obtained numerical findings are then graphically shown and analysed in depth. The results show that radiation has a significant impact on boosting heat transfer for the ZnO-SAE50 nanolubricant flow across the disk surface. The temperature boundary layer creates energy when the heat source/sink parameter values increase, causing thermal profiles to rise.

8.2 Mathematical Elucidation:

In the current examination, we deal with a steady incompressible flow of $ZnO - SAE50$ nano lubricant flow over a disk rotating with a constant angular velocity Ω about its axial axis z under the influence of uniform horizontal magnetic field. The flow geometry for the proposed work is illustrated through Fig.8.1. Let, $V = (u, v, w)$ be the induced velocity field. The heat transport analysis is done in the presence of thermal radiation and heat source/sink (HSS). The current density for conducting disk is expressed as $J = \sigma_1(E + V \times B)$ with uniform magnetic field vector B represented in cylindrical coordinate system as $B = (B_r, B_\varphi, B_z)$. The Lorentz force owing to the magnetic field acting on the fluid flow may be represented as $J \times B = \sigma_1(V \times B) \times B$. Further, the Lorentz force is expressed as (see Turkyilmazoglu [93]):

$$J \times B = \sigma \left(-B_\varphi (B_\varphi u - B_r v), -B_r (B_\varphi u - B_r v), - (B_\varphi^2 + B_r^2) w \right), \quad (8.2.1)$$

If the angle of inclination between the r -direction and the direction of the magnetic field vector $B = (B_r, B_\varphi, 0)$ is defined as α , it can be written as (see Turkyilmazoglu [93]):

$$B_\varphi = |B| \sin \alpha, B_r = |B| \cos \alpha. \quad (8.2.2)$$

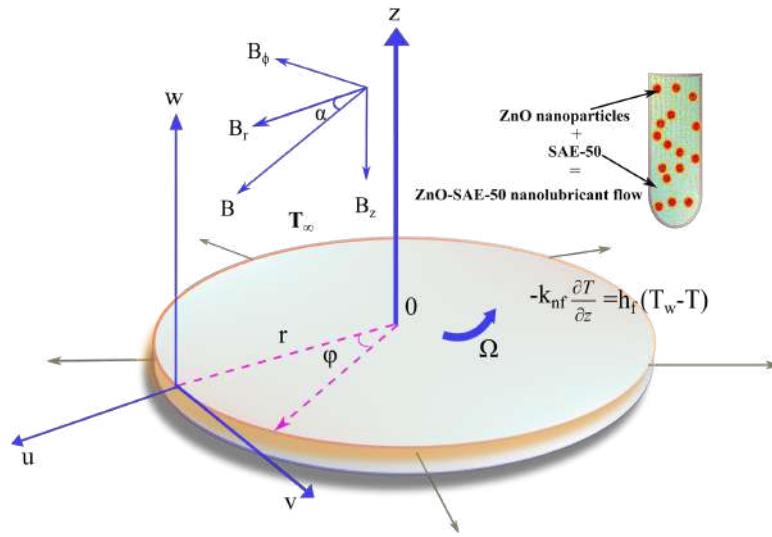


Figure 8.1: Flow Geometry

The governing equations for the flow affected by all the above assumptions and the horizontal magnetic field lead to the following equations:

$$(\nabla \cdot V) = 0, \quad (8.2.3)$$

$$(V \cdot \nabla)V = \nu_{nf} \nabla^2 V + \frac{1}{\rho_{nf}} J \times B, \quad (8.2.4)$$

$$(V \cdot \nabla)T = \alpha_{nf} \nabla^2 T - \frac{1}{(\rho C_p)_{nf}} \nabla \cdot q_r + \frac{1}{(\rho C_p)_{nf}} \widehat{Q}(T - T_\infty). \quad (8.2.5)$$

Here, using Rosseland approximation, the radiative heat flux q_r is expressed as follows:

$$q_r = \frac{4\sigma^{**}}{3k^{**}} \frac{\partial T^4}{\partial z}. \quad (8.2.6)$$

Following expression can be obtain by expanding T^4 using Taylor's series and ignoring higher order terms

$$T^4 \cong 4T_\infty^3 T - 3T_\infty^4. \quad (8.2.7)$$

Adopting Eqs. (8.2.6) and (8.2.7), in Eq. (8.2.5) one can write

$$\left. \begin{aligned} u \frac{\partial T}{\partial r} + w \frac{\partial T}{\partial z} = a_{nf} \left(\frac{\partial^2 T}{\partial r^2} + \frac{1}{r} \frac{\partial T}{\partial r} + \frac{\partial^2 T}{\partial z^2} \right) + \frac{16\sigma^{**} T_\infty^3}{(\rho C_p)_{nf} 3k^{**}} \left(\frac{\partial^2 T}{\partial r^2} + \frac{1}{r} \frac{\partial T}{\partial r} + \frac{\partial^2 T}{\partial z^2} \right) \\ + \frac{1}{(\rho C_p)_{nf}} \widehat{Q}(T - T_\infty), \end{aligned} \right\} \quad (8.2.8)$$

The boundary constraints for the proposed work are;

$$\left. \begin{aligned} u = C_0, r = U_w(r), v = \Omega r, w = w_w, -k_{nf} \frac{\partial T}{\partial z} = h_f (T_w - T) \quad \text{at } z = 0, \\ u \rightarrow 0, v \rightarrow 0, w \rightarrow 0, T \rightarrow T_\infty \quad \text{as } z \rightarrow \infty. \end{aligned} \right\} \quad (8.2.9)$$

Invoking Ref.[94-96], the effective dynamic viscosity, the effective density, the heat capacitance and the effective thermal conductivity of the ZnO-SAE50 nanolubricant is given by

$$\mu_{nf} = \mu_{ZnO-SAE50} = \mu_{SAE50}(-0.002407T + 1.035 + 0.04336\phi), \quad (8.2.10)$$

$$\mu_{SAE50} = 2.174e^{-0.06062T}, \quad (8.2.11)$$

$$\rho_{nf} = \rho_{ZnO-SAE50} = (1 - \phi)\rho_{SAE50} + \phi\rho_{ZnO}, \quad (8.2.12)$$

$$(\rho C_p)_{nf} = (\rho C_p)_{ZnO-SAE50} = (1 - \phi)(\rho C_p)_{SAE50} + \phi(\rho C_p)_{ZnO}, \quad (8.2.13)$$

$$\frac{k_{nf}}{k_f} = \frac{k_{ZnO-SAE50}}{k_{SAE50}} = 1 + \frac{k_{ZnO} A_{ZnO}}{k_{SAE50} A_{SAE50}} + ck_{ZnO} P_e \left(\frac{A_{ZnO}}{k_{SAE50} A_{SAE50}} \right), \quad (8.2.14)$$

$$c = 25000, P_e = \frac{d_{ZnO} u_{ZnO}}{\alpha_{SAE50}}, \frac{A_{ZnO}}{A_{SAE50}} = \frac{d_{SAE50}}{d_{ZnO}} \left(\frac{\phi}{1 - \phi} \right), u_{ZnO} = \frac{2k_B T}{\pi \mu_{SAE50} d_{ZnO}^2}. \quad (8.2.15)$$

The governing equations are reduced into the non-dimensional form by using the following similarity variables transform:

$$u = r\Omega F(\eta), \eta = \sqrt{\frac{\Omega}{\nu_f}} z, v = r\Omega G(\eta), w = \sqrt{\nu_f \Omega} H(\eta), \theta(\eta) = \frac{T - T_\infty}{T_w - T_\infty}. \quad (8.2.16)$$

The following set of non-dimensional nonlinear differential equations are obtained:

$$H' + 2F = 0, \quad (8.2.17)$$

$$\varepsilon_1 F'' - HF' - F^2 + G^2 - \varepsilon_2 M \sin \alpha [\sin \alpha F - \cos \alpha G] = 0, \quad (8.2.18)$$

$$\varepsilon_1 G'' - 2FG - HG' + \varepsilon_2 M \cos \alpha [\sin \alpha F - \cos \alpha G] = 0, \quad (8.2.19)$$

$$\varepsilon_1 H'' - HH' - \varepsilon_2 MH = 0, \quad (8.2.20)$$

$$\frac{1}{Pr} \varepsilon_3 \left(\frac{k_{nf}}{k_f} + R \right) \theta'' - H\theta' + \varepsilon_3 Q^* \theta = 0, \quad (8.2.21)$$

where,

$$\varepsilon_1 = \frac{1.035 + 0.04336\phi - 0.002407T}{(1 - \phi) + \phi \frac{\rho_{ZnO}}{\rho_{SAE50}}}, \quad \varepsilon_2 = \frac{1}{(1 - \phi) + \phi \frac{\rho_{ZnO}}{\rho_{SAE50}}}, \quad \varepsilon_3 = \frac{1}{(1 - \phi) + \phi \frac{(\rho C_p)_{ZnO}}{(\rho C_p)_{SAE50}}},$$

The reduced boundary constraints for the proposed work are:

$$\left. \begin{aligned} F(0) = \omega, G(0) = 1, H(0) = W_s, \frac{k_{nf}}{k_f} \theta'(0) = -Bi(1 - \theta(0)), \\ F(\infty) \rightarrow 0, H(\infty) \rightarrow 0, G(\infty) \rightarrow 0, \theta(\infty) \rightarrow 0. \end{aligned} \right\} \quad (8.2.22)$$

where, $W_s = \frac{w_w}{\sqrt{\nu_f \Omega}}$. Here, W_s represents ($W_s < 0$) a uniform suction or injection ($W_s > 0$)

at the surface.

Non-dimensional parameters for the proposed problem are ;

$$Pr = \frac{\mu_f C_p}{k_f}, \quad R = \frac{16\sigma^{**}T_\infty^3}{3k^{**}k_f}, \quad \omega = \frac{C_0}{\Omega}, \quad Bi = \frac{h_f}{k_f} \sqrt{\frac{\nu_f}{\Omega}}, \quad M = \frac{\sigma^* |B|^2}{\rho_f \Omega}, \quad Re_x = \frac{r^2 \Omega}{\nu_f}, \quad \hat{Q} = \frac{Q}{\Omega (\rho C_p)_f}$$

8.3 Deliberation of Results:

The graphical effects of the physical dimensionless quantities on the involved profiles are discussed in this section. This study utilizes the RKF-45 method with the shooting process to simulate fluid flow, temperature, and mass transfer with the uniform horizontal magnetic field. The effect of relevant factors on respective profiles is shown in Figs.8.2–8.9 The thermo-physical properties of nanoparticles (ZnO) and base liquid (SAE50) are listed in Table 8.1 We also compared the numerical findings to previous studies (see Table 8.2).

Table 8.1: **Thermo-physical properties of nanopartcles ZnO and base liquid $SAE50$ see reference ([94-96]),**

	$d(nm)$	$k(W/mK)$	$\rho(Kgm^3)$	$\mu(Ns/m^2)$	$C_p(J/(kg.K))$
ZnO	60	19	5.606	-	544
$SAE50$	40	0.15	0.960	0.192543	1900

Table 8.2: **Comparison of the $-\theta'(0)$, $-H'(\infty) - G'(0)$ and $F'(0)$ values for some reduced cases.,**

	kelson and Desseaux[97]	Bachok et al. [98]	Turkyilmazoglu [99]	Present results
F'	0.510233	0.5102	0.51023262	0.51023265
$-\theta'(0)$	—	0.9337	0.93387794	0.93387798
$-H'(\infty)$	0.884474	—	0.88447411	0.88447411
$-G'(0)$	0.615922	0.6159	0.61592201	0.61592202

Fig. 8.2 and Fig.8.3 show the impact of M on the $F(\eta)$ and $G(\eta)$, respectively. The decrease in $F(\eta)$ and $G(\eta)$ is caused by an increase in M values. When the magnetic field intensity is increased, both velocity profiles are observed to fall dramatically. The Lorentz force is associated with the M . The velocity profiles with higher M values decline as a consequence of the Lorentz force (LF) resisting the motion in the system. The restricting character of LF formed as a consequence of interaction among conducting liquid and applied magnetic field may be seen as the cause for decay of fluid motion. The effect of ω on $G(\eta)$ is showed in Fig.8.4 The rise in ω drops down the $G(\eta)$. The rise in ω induces a higher fluid viscosity, which creates resistance between the fluid particles, resulting in more disorder in the system and a drop-in velocity. Fig.8.5 and Fig.8.6 show the influence of W_s on the $F(\eta)$ and $G(\eta)$, respectively. The decrease in $F(\eta)$ and $G(\eta)$ is caused by an increase in W_s values. The suction situation was studied in this research, based on the boundary-layer assumption, which said that the boundary-layer thickness should be extremely thin and that it should not be permitted to expand since it would contradict Prandtl's boundary-layer assumption in 1904. When suction is pragmatic to the disk surface, the quantity of liquid drawn into the surface decreases, and the hydrodynamic boundary layer thins.

Fig.8.7 validates the consequence of R on $\theta(\eta)$. The upsurge in R inclines the $\theta(\eta)$. The $\theta(\eta)$ seems to grow as the R increases. Physically, a rise in R correlates to an increase in radiation with heat transfer, consequential in higher energy levels of the molecules and hence the heat transport upsurgues noticeably. Fig.8.8 present the effects of Q on $\theta(\eta)$. Here, positive values for Q represents the heat generation(source) case and negative values for Q represents the heat absorption(sink) case. For high values of Q , the magnitude of the $\theta(\eta)$ increases. The temperature field rises when the quantity of heat absorption

decreases. With higher levels of $Q > 0$, it is discovered that layer related to $\theta(\eta)$ produces energy, causing $\theta(\eta)$ to rise. Fig.8.9 demonstrates the significance of Bi on $\theta(\eta)$. The upsurge in the value of Bi inclines the $\theta(\eta)$. This is due to the fact that when Bi increases, the heat resistance of the disk decreases. Without a doubt, convective heating expands the $\theta(\eta)$. Numerical values for F' and G' for diverse parameters are displayed in Table 8.3. Here, the growth in values of M and ω reduces the both F' and G' but differing trend is detected for augmented W_s . Numerical values for $\theta'(0)$ with the impact of pertinent parameters are displayed in Table 8.4. Here, the rise in Bi, M and R reduces the $\theta'(0)$ but contrary trend is detected for augmented Q .

8.4 Inference:

The current study looks at convective heat transfer with radiation, heat source/sink and horizontal magnetic field effects on nanolubricant flow over a disk. The modelled PDEs are turned into ODEs via apt similarity variables. The RKF-45 with shooting technique are employed to describe the equations. The influence of many non-dimensional components on physically interesting values is shown graphically. The nanolubricant (ZnO-SAE50) decreases wear impact in devices such as bore pistons, shafts, gaskets, and valve mechanisms in a way that other nanofluids do not. This is one of the reasons why nanolubricants are being considered in this research. The following are the most significant findings of this analysis.

- The decrease in $F(\eta)$ and $G(\eta)$ is caused by an increase in M values which causes Lorentz force.
- The radiation plays a vital role in increasing the heat passage from the disk's surface.

- With higher Values of $Q > 0$, it is discovered that the temperature boundary layer produces energy, causing thermal profiles to rise.
- The convective heating expands the thermal boundary layer.

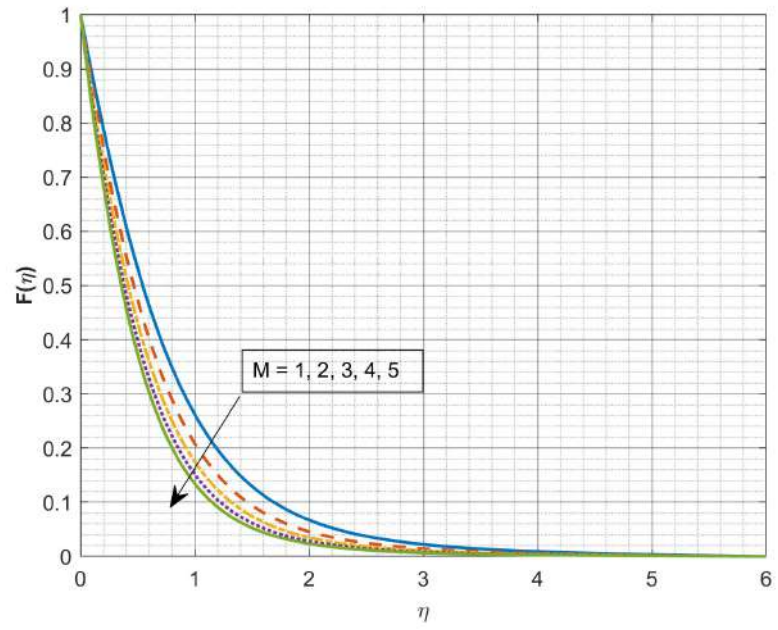


Figure 8.2: Effect of M on $F(\eta)$

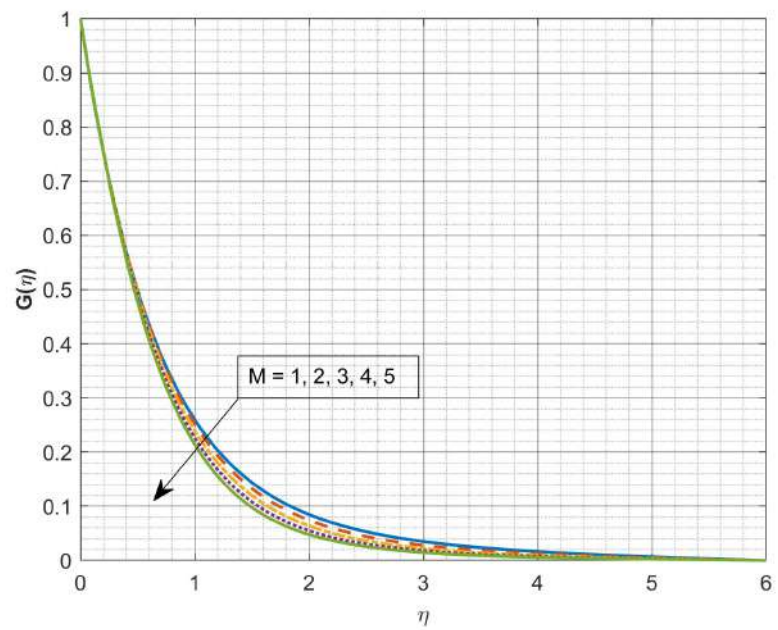


Figure 8.3: Effect of M on $G(\eta)$

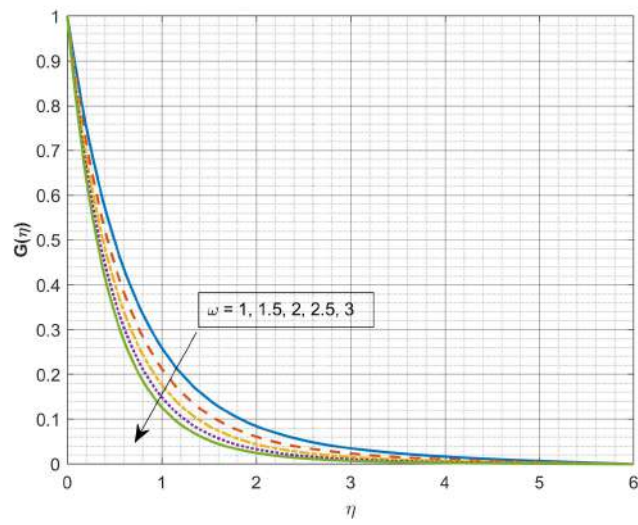


Figure 8.4: Effect of ω on $G(\eta)$

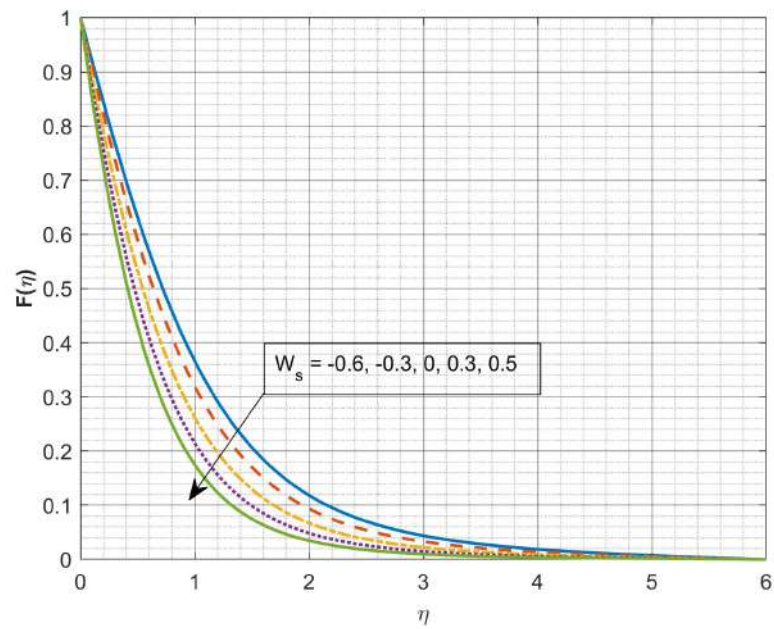


Figure 8.5: Effect of W_s on $F(\eta)$

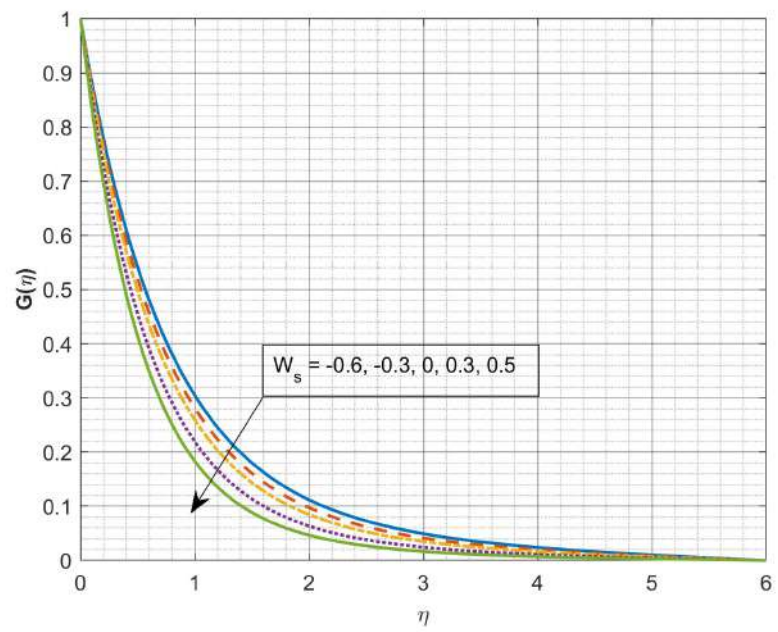


Figure 8.6: Effect of W_s on $G(\eta)$

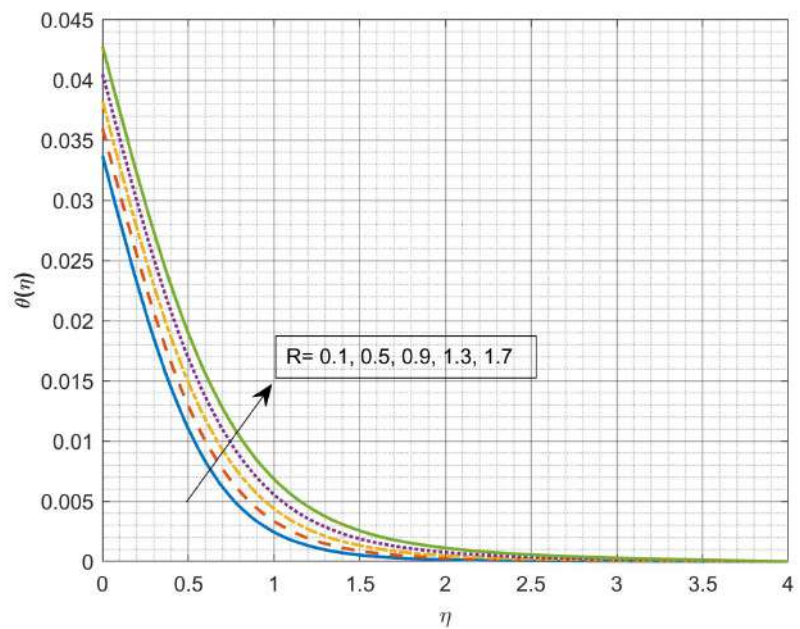


Figure 8.7: Effect of R on $\theta(\eta)$

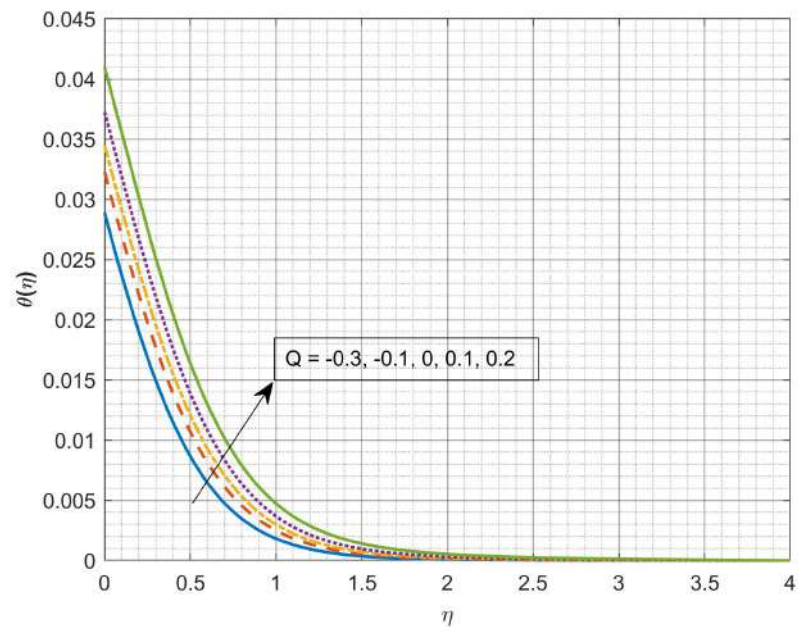


Figure 8.8: Effect of Q on $(\theta(\eta))$

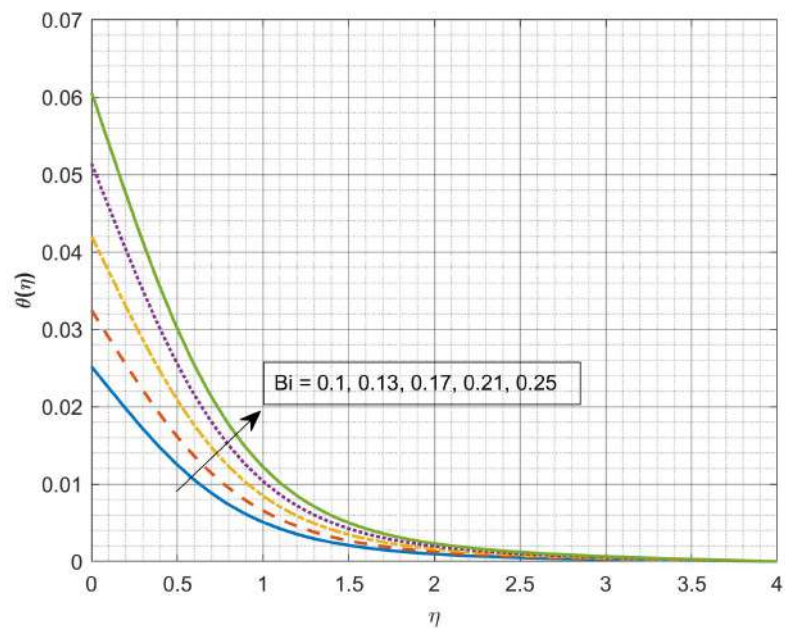


Figure 8.9: Effect of Bi on $(\theta(\eta))$

Table 8.3: Numerical values for F' and G' for varied parameters.

W_s	M	ω	F'	G'
0.001	3	1	-0.764578968427958	-0.752200354780472
0.01			-0.762660994618254	-0.750563617001044
0.1			-0.743802271450565	-0.734440826540028
	0.1		-0.756963551223748	-1.43846728926856
	1		-1.06190215540737	-1.39202715190809
	2		-1.29245912232373	-1.3608254297835
		0.8	-0.206796372150857	-0.655076336906186
		0.9	-0.38720663571073	-0.688484922067749
		1.1	-0.573186028799712	-0.720818593746491

Table 8.4: Numerical values for $\theta'(0)$ with respect to varied parameters.

M	Q	R	Bi	$\theta'(0)$
3	0.1	0.1	0.2	-0.0917768857548684
4				-0.0995243526965264
5				-0.10746511246978
	0.2			-0.0535571472424057
	0.4			-0.0532900931505206
	0.5			-0.0528613395973525
		0.2		-0.0926222342363569
		0.3		-0.093472003678962
		0.4		-0.0943264393882579
			0.1	-0.0345370548580474
			0.3	-0.205064420250062
			0.4	-0.535682591980692

Bibliography

- [1] B.C. Sakiadis, *Boundary layer behavior on continuous solid flat surface*. AICHE.J, **7(1)** (1961), 26-28.
- [2] K. Vajravelu, *Viscous flow over a non-linearly stretching sheet*". Applied Mathematics and Computation, **124(3)** (2001), 281–288.
- [3] M. Sajid and T. Hayat. *Influence of thermal radiation on the boundary layer flow due to an exponentially stretching sheet*. International Communications in Heat and Mass Transfer, **35(3)** (2008), 347-356.
- [4] J.A. Khan, M. Mustafa, T. Hayat, A. Alsaedi. *Three-dimensional flow of nanofluid over a non-linearly stretching sheet: An application to solar energy*. International Journal of Heat and Mass Transfer, **86** (2015), 158–164.
- [5] B. J. Gireesha, M. Umshaiah, B.C. Prasannakumara, S. N. Shashikumar., M. Archana. *Impact of non-linear thermal radiation on magnetohydrodynamic three-dimensional boundary layer flow of Jeffrey nanofluid over a non-linearly permeable stretching sheet*. Physica A: Statistical Mechanics and Its Applications, **549** (2020), 124051.

- [6] E. O. Fatunmbi and S. S. Okoya. *Heat transfer in boundary layer magneto-micropolar fluids with temperature-dependent material properties over a stretching sheet*. Advances in Materials Science and Engineering, 2020 (2020).
- [7] A. Dawar, Z. Shah, A. Tassaddiq, S. Islam and P. Kumam. *Joule heating in magnetohydrodynamic micropolar boundary layer flow past a stretching sheet with chemical reaction and microstructural slip*. Case Studies in Thermal Engineering, **25** (2021), 100870.
- [8] V. Puneeth, S. Manjunatha, J.K. Madhukesh, G.K. Ramesh. *Three-dimensional mixed convection flow of hybrid casson nanofluid past a non-linear stretching surface: A modified Buongiorno's model aspects*. Chaos, Solitons and Fractals, **152** (2021), 111428.
- [9] M. A. Z. Raja, M. Shoaib, S. Hussain, K. S. Nisar and S. Islam. *Computational intelligence of Levenberg-Marquardt backpropagation neural networks to study thermal radiation and Hall effects on boundary layer flow past a stretching sheet*. International Communications in Heat and Mass Transfer, **130** (2022),105799.
- [10] Z. Shah, A. Dawar, I. Khan, S. Islam, D. L. C. Ching and A. Z. Khan. *Cattaneo-Christov model for electrical magnetite micropolar Casson ferrofluid over a stretching/shrinking sheet using effective thermal conductivity model*. Case Studies in Thermal Engineering, **13** (2019),100352.
- [11] W. D. Chang, N. D. Kazarinoff and C. Lu. *A new family of explicit solutions for the similarity equations modelling flow of a non-Newtonian fluid over a stretching sheet*. Arch. Ration. Mech. Anal. **113(2)** (1991),191–195.

- [12] S. Abel, P. H. Veena, K. Rajgopal, and V. K. Pravin. *Non-Newtonian magnetohydrodynamic flow over a stretching surface with heat and mass transfer*. *Int. J. Non-Linear. Mech*, **39(7)** (2004), 1067–1078.
- [13] M. Mustafa, T. Hayat, I. Pop, and A. Aziz. *Unsteady boundary layer flow of a Casson fluid due to an impulsively started moving flat plate*. *Heat Transf. - Asian Res*, **40(6)** (2011), 563–576.
- [14] M. Almakki, S. K. Nandy, S. Mondal, P. Sibanda, and D. Sibanda. *A model for entropy generation in stagnation-point flow of non-Newtonian Jeffrey, Maxwell, and Oldroyd-B nanofluids*. *Heat Transfer—Asian Research*, **48(1)** (2019), 24–41.
- [15] M. Irfan, M. Khan, W. A. Khan, M. Alghamdi, and M. Z. Ullah. *Influence of thermal-solutal stratifications and thermal aspects of non-linear radiation in stagnation point Oldroyd-B nanofluid flow*. *International Communications in Heat and Mass Transfer*, **116** (2020), 104636.
- [16] S.M. Abo-Dahab, M.A. Abdelhafez, F. Mebarek-Oudina, S.M. Bilal. *MHD Casson nanofluid flow over non-linearly heated porous medium in presence of extending surface effect with suction/injection*, *Indian J Phys.* **95** (2021), 2703–2717.
- [17] S. Pandey, S. Y. Yoon, S. Balachandar and M. Y. Ha. *Experimental and numerical investigations of thermal and flow characteristics of a shear-thinning non-Newtonian fluid in a differentially heated cavity*, *International Journal of Heat and Mass Transfer.* **187** (2022), 122570.
- [18] P. G. Saffman, *On the stability of laminar flow of it dusty gas*. *J Fluid Mech.* **13** (1961),120–128.

- [19] K. Vajravelu and J. Nayfeh, *Hydromagnetic flow of a dusty fluid over a stretching sheet*. Int. J. Non. Linear. Mech. **27(6)** (1992), 937–945.
- [20] A. J. Chamkha. *The Stokes problem for a dusty fluid in the presence of magnetic field, heat generation and wall suction effects*. Int. J. Numer. Methods Heat Fluid Flow, **10(1)** (2000), 116–133.
- [21] B. J. Gireesha, B. Mahanthesh, O. D. Makinde, and T. Muhammad. *Effects of Hall current on transient flow of dusty fluid with nonlinear radiation past a convectively heated stretching plate*. Int. J. Numer. Methods Heat Fluid Flow, **387** (2018), 352-363.
- [22] B. Souayeh, K. G. Kumar, M. G. Reddy, S. Rani, N. Hdhiri, H. Alfannakh and M. R. Gorji. *Slip flow and radiative heat transfer behavior of Titanium alloy and ferromagnetic nanoparticles along with suspension of dusty fluid*. Journal of Molecular Liquids, **290** (2019), 111223.
- [23] M. G. Reddy and M. Ferdows. *Species and thermal radiation on micropolar hydro-magnetic dusty fluid flow across a paraboloid revolution*. Journal of Thermal Analysis and Calorimetry, **143(5)** (2021), 3699-3717.
- [24] Z. Khan, F. Ali, and M. Andualem. *Free convection flow of second grade dusty fluid between two parallel plates using Fick's and Fourier's laws: a fractional model*, Scientific Reports. **12(1)** (2022), 1-22.
- [25] P. Rana and R. Bhargava. *Numerical study of heat transfer enhancement in mixed convection flow along a vertical plate with heat source/sink utilizing nanofluids*, Commun Nonlinear Sci Numer Simul. **16(11)**, (2022), 4318–4334.

- [26] M. Sheikholeslami, M. Gorji Bandpy, R. Ellahi, M. Hassan and S. Soleimani. *Effects of MHD on Cu–water nanofluid flow and heat transfer by means of CVFEM*, J. Magn. Mater. **349** (2014), 188–200.
- [27] M. S. Hashmi, N. Khan, T. Mahmood and S. A. Shehzad. *Effect of magnetic field on mixed convection flow of Oldroyd-B nanofluid induced by two infinite isothermal stretching disks*, Int. J. Therm. Sci. **111** (2017), 463–474.
- [28] M. K. Nayak, R. Mehmood, O. D. Makinde, O. Mahian, and A. J. Chamkha. *Magnetohydrodynamic flow and heat transfer impact on ZnO-SAE50 nanolubricant flow over an inclined rotating disk*, J. Cent. South Univ. **26(5)** (2019), 1146–1160.
- [29] M. Ashraf, A. Abbas, A. Ali, Z. Shah, H. Alrabaiah, E. Bonyah. *Numerical simulation of the combined effects of thermophoretic motion and variable thermal conductivity on free convection heat transfer*, AIP Advances. **10** (2020), 085005.
- [30] Z. Uddin, K.S. Vishwak, S. Harmand. *Numerical duality of MHD stagnation point flow and heat transfer of nanofluid past a shrinking/stretching sheet: Metaheuristic approach*, Chinese Journal of Physics. **73** (2021), 442–461.
- [31] M. Z. Sharif, W. H. Azmi, N. N. M. Zawawi, and M. F. Ghazali. *Comparative air conditioning performance using SiO₂ and Al₂O₃ nanolubricants operating with Hydrofluoroolefin-1234yf refrigerant*, Appl. Therm. Eng. **205** (2022), 118053.
- [32] M. J. Uddin, Y. Alginahi, O. A. Bég, and M. N. Kabir. *"Numerical solutions for gyrotactic bioconvection in nanofluid-saturated porous media with Stefan blowing and multiple slip effects"*, Comput. Math. Appl. **72(10)** (2016), 2562–2581.

- [33] Kh. Hosseinzadeh, So. Roghani, A. R. Mogharrebi, A. Asadi, M. Waqas and D. D. Ganji. "*Investigation of cross-fluid flow containing motile gyrotactic microorganisms and nanoparticles over a three-dimensional cylinder*", Alex. Eng. J. **59(5)** (2020), 3297–3307.
- [34] P. Rana, N. Shukla, O. A. Bég, and A. Bhardwaj, "*Lie Group Analysis of Nanofluid Slip Flow with Stefan Blowing Effect via Modified Buongiorno's Model: Entropy Generation Analysis*", Differ. Equ. Dyn. Syst. **29** (2021), 193–210.
- [35] M. Imran, T. Kamran, S. A. Khan, T. Muhammad and H. Waqas. "*Physical attributes of bio-convection in nanofluid flow through a paraboloid of revolution on horizontal surface with motile microorganisms*", International Communications in Heat and Mass Transfer . **133** (2022), 105947.
- [36] S. Islam, A. Dawar, Z. Shah, and A. Tariq, "*Cattaneo–Christov theory for a time-dependent magnetohydrodynamic Maxwell fluid flow through a stretching cylinder*", Adv. Mech. Eng. , **13(7)** (2021), 1–11.
- [37] M. Khan, A. Ahmed, M. Irfan, and J. Ahmed. "*Analysis of Cattaneo–Christov theory for unsteady flow of Maxwell fluid over stretching cylinder*". J. Therm. Anal. Calorim , **144(1)**, (2021), 145–154.
- [38] Y.-X. Li, H. Waqas, K. Al-Khaled, A. A. Khan, M. I. Khan, S. U. Khan, R. Naseem, Y. M. Chu. "*Simultaneous features of Wu's slip, nonlinear thermal radiation and activation energy in unsteady bio-convective flow of Maxwell nanofluid configured by a stretching cylinder*". Chin. J. Phys. , **73** (2021), 462–478.

- [39] M. I. Khan, H. Waqas, S. U. Khan, M. Imran, Y. M. Chu, A. Abbasi, S. Kadry. "*Slip flow of micropolar nanofluid over a porous rotating disk with motile microorganisms, nonlinear thermal radiation and activation energy*", Int. Commun. Heat Mass Transf. , **122** (2021), 105161.
- [40] U. Farooq, H. Waqas, M. I. Khan, S. U. Khan, Y. M. Chu, S. Kadry. "*Thermally radioactive bio convection flow of Carreau nanofluid with modified Cattaneo-Christov expressions and exponential space-based heat source*", Alex. Eng. J. , **60(3)** (2021), 3073-3086.
- [41] Y. Q. Song, S. U. Khan, M. I. Khan, M. Awais, A. Abbasi, Q. H. Shi. "*Bidirectional non-linear stretched flow of Williamson nanofluid with swimming of motile gyrotactic microorganisms*", Appl. Math. Comput. **411** (2021), 126502.
- [42] C.Y. Wang. "*Fluid flow due to a stretching cylinder*", Phys. Fluids. **31** (1988), 466–468.
- [43] W.A. Khan, I. Pop. "*Boundary-layer flow of nanofluid past a stretching sheet*". Int. J.Heat Mass Transf. , **53** (2010), 2477–2483.
- [44] N. Acharya, K. Das, P. K. Kundu. "*Framing the features of MHD boundary layer flow past an unsteady stretching cylinder in presence of non-uniform heat source*". J. Mol. Liq. , **225** (2017), 418-425.
- [45] Choudhary S, Sharma PR, Makinde OD. "*MHD slip flow and heat transfer over an exponentially stretching permeable sheet embedded in a porous medium with heat source*",Front. Heat Mass Transf [FHMT]. **9(1)** (2017), 418-425.

- [46] Khan MN, Nadeem S. "*A comparative study between linear and exponential stretching sheet with double stratification of a rotating Maxwell nanofluid flow*". *Surf Interfaces*, **22** (2021), 100886.
- [47] Rana P, Bhargava R. "*Numerical study of heat transfer enhancement in mixed convection flow along a vertical plate with heat source/sink utilizing nanofluids*". *Communications in Nonlinear Science and Numerical Simulation*, **16(11)** (2011), 4318–4334.
- [48] Alhadhrami A, Alzahrani HAH, Naveen Kumar R, Punith Gowda RJ, Sarada K, Prasanna BM, Madhukesh, J.K. and Madhukeshwara, N . "*Impact of thermophoretic particle deposition on Glauert wall jet slip flow of nanofluid*", *Case Stud Therm Eng.* **28** (2021), 101404.
- [49] Wang F, Asjad MI, Zahid M, Iqbal A, Ahmad H, Alsulami MD. "*Unsteady thermal transport flow of Casson nanofluids with generalized Mittag-Leffler kernel of Prabhakar's type*", *J Mater Res Technol.* **14** (2021), 1292–1300.
- [50] Khan M, Gondal MA, Kumar S. "*A new analytical approach to solve exponential stretching sheet problem in fluid mechanics by variational iterative Padé method*", *J Math Comput Sci.* **3** (2011), 135–144.
- [51] Kameswaran PK, Narayana M, Sibanda P, Makanda G. "*On radiation effects on hydromagnetic Newtonian liquid flow due to an exponential stretching sheet*". *Boundary Value Problems*, **1** (2012), 1–16.
- [52] Magyari E, Keller B. "*Heat and mass transfer in the boundary layers on an exponentially stretching continuous surface*". *Journal of Physics D: Applied*, **32(5)** (1999), 577–585.

- [53] Abd El-Aziz M. "*Viscous dissipation effect on mixed convection flow of a micropolar fluid over an exponentially stretching sheet*". *Can. J. Phys.* **87(4)** (2009), 359–368.
- [54] Bidin B, Nazar R. "*Numerical solution of the boundary layer flow over an exponentially stretching sheet with thermal radiation*". *European journal of scientific research*, **33(4)** (2009), 710–717.
- [55] Ishak A. "*MHD boundary layer flow due to an exponentially stretching sheet with radiation effect*". *Sains Malaysiana*, **40(4)** (2011), 391–395.
- [56] Swati Mukhopadhyay, Rama Subba Reddy Gorla. "*Effects of partial slip on boundary layer flow past a permeable exponential stretching sheet in presence of thermal radiation*". *Heat and Mass Transfer*, **48(10)** (2012), 1773–1781.
- [57] S. A. Shehzad, A. Alsaedi, T. Hayat, and M. S. Alhuthali. "*Three-Dimensional Flow of an Oldroyd-B Fluid with Variable Thermal Conductivity and Heat Generation/Absorption*". *PLOS ONE*, **8(11)** (2013), e78240.
- [58] W. A. Khan, M. Irfan, and M. Khan. "*An improved heat conduction and mass diffusion models for rotating flow of an Oldroyd-B fluid*". *Results in Physics*, **8** (2017), 3583–3589.
- [59] M. I. Khan, S. Rashid, T. Hayat, M. Ayub, and A. Alsaedi. "*Magnetic effects in rotating flow of an Oldroyd-B fluid with chemical reaction and convective surface*". *Indian J. Phys.*, **94(9)** (2020), 1361–1367.
- [60] S. A. Shehzad, A. Alsaedi, T. Hayat, and M. S. Alhuthali. "*Thermophoresis particle deposition in mixed convection three-dimensional radiative flow of an Oldroyd-B fluid*". *J. Taiwan Inst. Chem. Eng.*, **45(3)** (2014), 787–794.

- [61] G. K. Batchelor and C. Shen. "*Thermophoretic deposition of particles in gas flowing over cold surfaces*". Journal of Colloid and Interface Science, **107(1)** (1985), 21–37.
- [62] L. Talbot, R. K. Cheng, R. W. Schefer, and D. R. Willis. "*Thermophoresis of particles in a heated boundary layer*". J. Fluid Mech., **101(4)** (1980), 737–758.
- [63] M. Subhas Abel, J. V. Tawade, and M. M. Nandeppanavar. "*MHD flow and heat transfer for the upper-convected Maxwell fluid over a stretching sheet*". Meccanica, **47(2)**, (2012), 385–393.
- [64] A. M. Megahed. "*Variable fluid properties and variable heat flux effects on the flow and heat transfer in a non-Newtonian Maxwell fluid over an unsteady stretching sheet with slip velocity*". Chinese Physics B , **22(9)**, (2013), 094701.
- [65] K. Sadeghy, H. Hajibeygi, and S.-M. Taghavi. "*Stagnation-point flow of upper-convected Maxwell fluids*". Int. J. Non-Linear Mech. , **41(10)**, (2006), 1242–1247.
- [66] M. Mustafa, T. Hayat, and A. Alsaedi. "*Rotating flow of Maxwell fluid with variable thermal conductivity: An application to non-Fourier heat flux theory*". Int. J. Heat Mass Transf. , **106**, (2017), 142–148.
- [67] A. Khan and I. Pop. "*Boundary-layer flow of a nanofluid past a stretching sheet*". Int. J. Heat Mass Transf. , **53(11)**, (2010), 2477–2483.
- [68] C. Y. Wang. "*Free Convection on a Vertical Stretching Surface*". ZAMM - J. Appl. Math. Mech. Z. Für Angew. Math. Mech. , **69(11)**, (1989), 418–420.
- [69] R. S. Reddy Gorla and I. Sidawi. "*Free convection on a vertical stretching surface with suction and blowing*". Appl. Sci. Res., **52(3)**, (1994), 247–257.

- [70] L. J. Grubka, K. M. Bobba. "*Heat transfer characteristics of a continuous, stretching surface with variable temperature*". ASME J Heat Trans., **107**, (1985), 248–250.
- [71] C. H. Chen. "*Laminar mixed convection adjacent to vertical, continuously stretching sheets*". Heat and Mass transfer , **33(5)**, (1998), 471–476.
- [72] M. Epstein, G.M. Hauser, R.E. Henry. "*Thermophoretic Deposition of Particles in Natural Convection Flow From a Vertical Plate*". Journal of Heat Transfer , **107**, (1985), 272–276.
- [73] A.S. Butt, M.N. Tufail, A. Ali. "*Three-dimensional flow of a magnetohydrodynamic Casson fluid over an unsteady stretching sheet embedded into a porous medium*". J. Appl. Mech. Tech. Phy. , **57**, (2016), 283–292.
- [74] C.S.K. Raju, N. Sandeep, M. Jayachandra Babu, V. Sugunamma. "*Dual solutions for three-dimensional MHD flow of a nanofluid over a non-linearly permeable stretching sheet*". Alexandria Engineering Journal , **55**, (2016), 151–162.
- [75] J.A. Khan, M. Mustafa, T. Hayat, A. Alsaedi. "*On Three-Dimensional Flow and Heat Transfer over a Non-Linearly Stretching Sheet: Analytical and Numerical Solutions*". PLOS ONE , **9**, (2014), e107287.
- [76] A. Khan, D. Khan, I. Khan, F. Ali, F. ul Karim, M. Imran. "*MHD Flow of Sodium Alginate-Based Casson Type Nanofluid Passing Through A Porous Medium With Newtonian Heating*". Scientific reports , **8(1)**, (2018), 1-12.
- [77] S.P.A. Devi, S.S.U. Devi. "*Numerical Investigation of Hydromagnetic Hybrid Cu – Al₂O₃/Water Nanofluid Flow over a Permeable Stretching Sheet with Suction*". In-

- ternational Journal of Nonlinear Sciences and Numerical Simulation , **17**, (2016), 249–257.
- [78] B. J. Gireesha, A. J. Chamkha, S. Manjunatha and C. S. Bagewadi. "*Mixed convective flow of a dusty fluid over a vertical stretching sheet with non-uniform heat source / sink and radiation*". Int. J. Numer. Methods Heat Fluid Flow , **23(4)**, (2011), 598-612.
- [79] P. T. Manjunatha, B. J. Gireesha, and B. C. Prasannakumara. "*Effect of radiation on flow and heat transfer of MHD dusty fluid over a stretching cylinder embedded in a porous medium in presence of heat source*". Int. J. Appl. Comput. Math. , **3(1)**, (2017), 293-310.
- [80] N. S. Akbar, S. Nadeem, R. U. Haq and Z. H. Khan. "*Numerical solutions of Magneto hydrodynamic boundary layer flow of tangent hyperbolic fluid flow towards a stretching sheet with magnetic field*". Indian Journal of Physics, , **87(11)**, (2013), 1121-1124.
- [81] Nagendramma V, Sreelakshmi K, and Sarojamma G. "*MHD Heat and Mass Transfer Flow Over a Stretching Wedge with Convective Boundary Condition and Thermophoresis*". Procedia Eng. , **127**, (2015), 963–969.
- [82] N. Amar and E. Al. "*Viscous Dissipation and Heat Transfer Effect on MHD Boundary Layer flow past a Wedge of Nano fluid Embedded in a Porous media*". Turk. J. Comput. Math. Educ. TURCOMAT , **12(4)**, (2021), 1352-1366.
- [83] M. S. Asmadi, R. M. Kasmani, Z. Siri, and S. Sivasankaran. "*Upper-Convected Maxwell Fluid Analysis Over A Horizontal Wedge Using Cattaneo-Christov Heat Flux Model*". Thermal Science , **25(2 Part A)**, (2021), 1013-1021.

- [84] N. G. Kafoussias and N. D. Nanousis. "*Magnetohydrodynamic laminar boundary-layer flow over a wedge with suction or injection*". Canadian Journal of Physics , **75(10)**, (1997), 733-745.
- [85] T. Hayat, S. Nawaz, and A. Alsaedi. "*Entropy generation in peristalsis with different shapes of nanomaterial*". Journal of Molecular Liquids, **248**, (2017), 447-458.
- [86] M. Hatami, R. Nouri, and D. D. Ganji. "*Forced convection analysis for MHD Al_2O_3 -water nanofluid flow over a horizontal plate*". Journal of Molecular Liquids, **187**, (2013), 294-301.
- [87] M. Sheikholeslami. "*Numerical approach for MHD Al_2O_3 -water nanofluid transportation inside a permeable medium using innovative computer method*". Comput. Methods Appl. Mech. Eng., **344**, (2019), 306-318.
- [88] N. Ahmed, Adnan, U. Khan, and S. T. Mohyud-Din. "*Influence of shape factor on flow of magneto-nanofluid squeezed between parallel disks*". Alex. Eng. J., **57(3)**, (2018), 1893-1903.
- [89] K.A. Yih. "*Uniform Suction/Blowing Effect on Forced Convection about A Wedge: Uniform Heat Flux*". Acta Mechanica, **128**, (1998), 173-181.
- [90] W. A. Khan and I. Pop. "*Boundary-Layer Flow past A Wedge Moving in A Nanofluid*". Mathematical Problems in Engineering, **2013**, (2013), 637285.
- [91] R. Kasmani, S. Sivasankaran and Zailan Sirib. "*Convective Heat Transfer of Nanofluid past A Wedge in the Presence of Heat Generation/Absorption with Suction/Injection*". AIP Conference Proceedings, **1605**, (2014), 506-511.

- [92] M. Turkyilmazoglu. "*MHD fluid flow and heat transfer due to a stretching rotating disk*". Int. J. Therm. Sci., **51**, (2012), 195-201.
- [93] M. Turkyilmazoglu. "*Flow and heat over a rotating disk subject to a uniform horizontal magnetic field*". Zeitschrift für Naturforschung A, **77(4)**, (2022), 329-337.
- [94] K. Sepyani, M. Afrand, and M. Hemmat Esfe. "*An experimental evaluation of the effect of ZnO nanoparticles on the rheological behavior of engine oil*". J. Mol. Liq, **236**, (2017), 198–204.
- [95] O. Pourmehran, M. Rahimi-Gorji, and D. D. Ganji. "*Heat transfer and flow analysis of nanofluid flow induced by a stretching sheet in the presence of an external magnetic field*". J. Taiwan Inst. Chem. Eng., **65**, (2016), 162–171.
- [96] M. K. Nayak, R. Mehmood, O. D. Makinde, O. Mahian, and A. J. Chamkha. "*Magnetohydrodynamic flow and heat transfer impact on ZnO-SAE50 nanolubricant flow over an inclined rotating disk*". J. Cent. South Univ., **26(5)**, (2019), 1146–1160.
- [97] N. Kelson and A. Desseaux. "*Note on porous rotating disk flow*". ANZIAM J., **42**, (2000), C837–C855.
- [98] N. Bachok, A. Ishak, and I. Pop. "*Flow and heat transfer over a rotating porous disk in a nanofluid*". Phys. B Condens. Matter., **406(9)**, (2011), 1767–1772.
- [99] M. Turkyilmazoglu. "*Nanofluid flow and heat transfer due to a rotating disk*". Comput. Fluids. , **94**, (2014), 139–146.

Nomenclature

A	slip parameter
a, b	stretching constants
b^*	chemotaxis constant
B_0	Magnetic field strength [<i>Tesla</i>]
Bi	Biot number
C	concentration
C_w	surface concentration
C_∞	ambient concentration
C_p	specific heat [$J kg^{-1} K^{-1}$]
C_F	Forchheimer coefficient
Cf_x	skin friction
C_s	heat capacity of the solid surface
D	Diffusivity [$m^2 s^{-1}$]
D_B	Brownian diffusion coefficient [$m^2 s^{-1}$]
D_m	diffusivity of microorganisms [$m^2 s^{-1}$]
D_T	thermophoresis diffusion coefficient [$m^2 s^{-1}$]
E	Activation energy parameter
E_a	Activation energy
Ec	Eckert number
E_1	Electric field
$f'(\eta)$	dimensionless velocity profile
h_1	heat transfer coefficient
J	Current density
K	Porosity parameter

$K^* = \frac{K_0}{e^{\frac{x}{l}}}$	Porous medium permeability [m^2]
$K_r^2 = K_1^2 \frac{e^{\frac{x}{l}}}{2}$	Reaction rate [s^{-1}]
k	Thermal conductivity [$kg\ m\ K^{-1}\ s^{-3}$]
k^*	thermophoretic coefficient
k_r	reaction rate for chemical reaction [s^{-1}]
K_1	permeability parameter
k^{**}	mean absorption coefficient
l	mass concentration parameter of dust particles
L_b	bioconvection Lewis number
Le	Lewis number
M	magnetic parameter
M_E	melting parameter
m	Wedge angle parameter
M^* and N	mass and number density of the dust particles per unit volume
Nu_x	Nusselt number (dusty fluid flow)
Nu	Nusselt number
N_t	thermophoresis parameter
N	microorganism's density
N_b	Brownian motion parameter
N_∞	cylindrical ambient
n	Fitted rate constant
N_t^*	thermophoretic parameter (for thermophoretic particle deposition)
p	Pressure
$P(\eta)$	Dimensionless pressure profile
Pe	Peclet number

Pr	Prandtl number
Q	Heat generation parameter
\hat{Q}	Uniform heat generation coefficient
q_w	Heat flux
q_m	mass flux
q_r	radiative heat flux
R	radiation parameter
r_1	radius of dust particle
Re	Reynolds number
Re_x	Local Reynolds number
Rc	Chemical reaction rate parameter
S_1	unsteadiness parameter
Sh	Sherwood number
Sn	microorganism's density number
Sc	Schmidt number
S	Suction parameter
T	Temperature [K]
T_∞	ambient temperature[K]
T_w	wall temperature[K]
(u, v, w)	velocity components[ms^{-1}]
(u_p, v_p)	particle phase velocity components[ms^{-1}]
(r, φ, z)	Cylindrical coordinates[m]
$v_0 e^{\frac{x}{2l}}$	Suction velocity

V_T	thermophoretic velocity
W_s	Uniform suction/injection parameter
W_c	cell swimming speed
(x, y, z)	Coordinate axes[m]
(r, z)	polar coordinates[m]

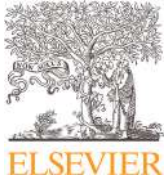
Greek Symbols

Ω	Angular disk speed[s^{-1}]
α_1	angle between the horizontal magnetic field components
λ_c	concentration relaxation time [s]
β	Casson parameter
σ	chemical reaction rate parameter
α	curvature parameter
μ	Dynamic viscosity [$kgm^{-1}s^{-1}$]
$\theta(\eta)$	dimensionless thermal profile
$\chi(\eta)$	dimensionless concentration profile
ρ_f	density of the liquid [kgm^{-3}]
ρ_p	density of the dust particle [kgm^{-3}]
$\beta_1 = \lambda_1 a$	Deborah number for relaxation time
$\beta_2 = \lambda_2 a$	Deborah number for retardation time
λ_2	dimensionless thermal relaxation time
$\vartheta(\eta)$	dimensionless motile microorganism profile
σ^*	electrical conductivity [$kg k^{-4}s^{-3}$]
β_v	fluid-particle interaction parameter
τ	heat capacity ratio

ν	kinematic viscosity [m^2s^{-1}]
ϖ	microorganism difference parameter
β^*	Maxwell fluid parameter
β_w	Measure of pressure gradient
σ_1	Magnetic conductivity
γ	Newtonian heating parameter
γ_1	positive constant
ω	Rotation strength parameter
$\lambda_c = a\Gamma_c$	relaxation time parameter of concentration
Γ_e	relaxation time for heat flux (for double diffusion) [s]
λ_2	retardation time [s]
$\lambda_E = a\Gamma_e$	relaxation time parameter of temperature
$\lambda = \frac{\Omega}{a}$	rotation parameter
Γ_c	relaxation time for mass flux
λ_1	relaxation time [s]
ψ	stream function
η	similarity variable
σ^{**}	Stefan-Boltzman constant
γ_2	specific heat ratio
θ_w	temperature ratio parameter
τ_T	thermal equilibrium time

Nomenclature

δ	Temperature difference parameter.
α_1	thermal diffusivity
β_t	thermal relaxation time parameter
λ_t	thermal relaxation time[s]
ϕ	Volume fraction
γ_3	viscoelastic fluid parameter



Combined impact of Cattaneo-Christov double diffusion and radiative heat flux on bio-convective flow of Maxwell liquid configured by a stretched nano-material surface

Yu-Ming Chu^{a,b}, B.M. Shankaralingappa^{c,d}, B.J. Gireesha^c, Faris Alzahrani^e,
M. Ijaz Khan^{e,f,*}, Sami Ullah Khan^g

^a Institute for Advanced Study Honoring Chen Jian Gong, Hangzhou Normal University, Hangzhou 311121, PR China

^b Department of Mathematics, Huzhou University, Huzhou 313000, PR China

^c Department of Studies and Research in Mathematics, Kuvempu University, Shankaraghatta, Shimoga, Karnataka 577 451, India

^d Department of Mathematics, Government Science College (Autonomous), Hassan, Karnataka 573201, India

^e Mathematical Modelling and Applied Computation Research Group (MMAC), Department of Mathematics, King Abdulaziz University, Jeddah, Saudi Arabia

^f Department of Mathematics and Statistics, Riphah International University I-14, Islamabad 44000, Pakistan

^g Department of Mathematics, COMSATS University Islamabad, Sahiwal 57000, Pakistan

ARTICLE INFO

Article history:

Received 26 May 2021

Revised 13 October 2021

Accepted 18 December 2021

Available online 29 December 2021

Keywords:

Maxwell liquid

Cattaneo-Christov concept

Stretching cylinder

Radiation effect

Bioconvection

ABSTRACT

The current research focuses on nano-material suspensions and flow characteristics in the context of their applications. The use of such materials in biomedical rheological models has garnered considerable attention. Having such practical and potential applications of nanofluids our goal is to analyse the radiative flow of Maxwell nanofluid on a stretching cylinder by considering magnetic effect, Stefan blowing and bioconvection. By selecting appropriate similarity variables, the equations that reflect the stated flow are transformed to ordinary differential equations. A Runge-Kutta-Fehlberg fourth-fifth order method (RKF-45) along with shooting scheme is used to solve the reduced equations. Graphical representations are used to give a clear knowledge of the behavior of dimensionless parameters on dimensionless velocity, concentration, and thermal profiles, which are strategized and debated by using physical descriptions. The significant results claimed via reported model convinced a declining velocity change due to curvature constant. The upshot change in thermal and mass relaxation times parameters declines the thermal and concentration pattern, respectively. The peak fluctuation in Brownian factor advances the thermal profile but declines the concentration profile. The rise in values of microorganism difference parameter and Peclet number declines the concentration of microorganisms.

© 2021 Elsevier Inc. All rights reserved.

1. Introduction

The non-Newtonian fluids are essential to research because of their applications in industry and engineering. In nature, there exists a variety of materials with various properties. The application of Navier-Stokes theory to all of these materials

* Corresponding author at: Mathematical Modelling and Applied Computation Research Group (MMAC), Department of Mathematics, King Abdulaziz University, Jeddah, Saudi Arabia.

E-mail address: mikhan@math.qau.edu.pk (M.I. Khan).

Evaluation of heat and mass transfer characteristics in a nanofluid flow over an exponentially stretchable sheet with activation energy

Proc IMechE Part E:
J Process Mechanical Engineering
1–10
© IMechE 2022
Article reuse guidelines:
sagepub.com/journals-permissions
DOI: 10.1177/09544089221074827
journals.sagepub.com/home/pie



JK Madhukesh¹ , BM Shankaralingappa^{2,3}, BJ Gireesha² 
and BC Prasannakumara¹ 

Abstract

The current study explores the impact of heat source/sink on the flow of nanofluid across an exponentially stretchable sheet with the suspension of TiO_2 as nanoparticle in base liquid water. Furthermore, activation energy, Newtonian heating and porous medium are accounted in the modelling. The modelling equations are transformed into a system of ordinary differential equations (ODEs) using similarity transformations. To solve these equations numerically, the Runge Kutta Fehlberg 45 (RKF 45) method and shooting approach are used. Graphical representations are used to study and address the effect of important factors on flow fields, heat, and mass transfer rates. The outcome reveals that, rising values of porous and suction parameters declines the velocity field. The rise in values of heat source/sink parameter declines the heat transfer. Moreover, rate of declination in heat transfer is faster for Newtonian heating (NH) case than common wall temperature (CWT) case. The rise in values of volume fraction and heat source/sink parameter declines the Nusselt number for both CWT and NH cases. Further, the fluid shows improved rate of heat transfer for CWT case than NH case.

Keywords

Nanofluid, Heat source sink, Activation energy, Newtonian heating, Exponential stretching sheet.

Date received: 8 August 2021; accepted: 23 October 2021

1. Introduction

Nanoparticle research is now a popular subject of discussion due to its wide range of applications in minerals, oil, solar energy, environmental and microelectronic applications. Traditional liquids such as engine oil, water, and ethylene-glycol are poor heat conductors, restricting their efficiency in heavy mechanical applications. Metals have a threefold increased heat conductivity. As a consequence, it makes sense to saturate metallic nanoparticles in a common base liquid in order to enhance thermophysical properties, especially thermal and electric conductivity. Nanoparticles having diameters less than or equal to 100 nm may stay suspended in a fluid for a longer period of time when compared to larger particles. As a consequence of this saturation, the heat-mass transmission capacity of the basic liquids is significantly increased, and such a liquid is referred to as a nanofluid. Nanofluids include up to 5% volume percentage of nanoparticles, increasing the effective heat transfer rate. This is why nanofluids are crucial in today's technology and engineering fields. As a result, many researchers investigated the flow of nanofluids through various surfaces. Rana and Bhargava¹ explored the heat conveyance improvement in convective stream of $\text{Ag}/\text{Cu}/\text{Cu}/\text{TiO}_2$ -water based nanoliquid flow on an upright plate.

Kumar et al.² conferred the Casson fluid flow with suspension of TiO_2 and graphene oxide nanoparticles past a poignant disk. Gowda et al.³ deliberated the dissipative stream of dusty liquid with suspension of Titania and Cupper nanoparticles. Patil and Kulkarni⁴ conferred the mixed convective stream of $\text{Ag}-\text{TiO}_2$ -water-based hybrid nanoliquid flow on a slender cylinder. Sinha and Filippov⁵ examined the stream TiO_2 water based nanofluid along a vertical permeable stretching surface. Some recent studies on different nanofluids are found in studies.⁶⁻¹⁰

Despite many physical challenges, the examination of heat source/sink characteristics of heat transfer is one of the utmost significant subjects in different engineering

¹Department of Mathematics, Davangere University, Davangere, Karnataka, India

²Department of Studies and Research in Mathematics, Kuvempu University, Shimoga, Karnataka, India


³Department of Mathematics, Government Science College (Autonomous), Hassan, Karnataka, India

Corresponding author:

BC Prasannakumara, Department of Mathematics, Davangere University, Davangere, Karnataka 577002, India.
Email: dr.bcprasanna@gmail.com

Article

The Impact of Cattaneo–Christov Double Diffusion on Oldroyd-B Fluid Flow over a Stretching Sheet with Thermophoretic Particle Deposition and Relaxation Chemical Reaction

Bheemasandra M. Shankaralingappa ^{1,2}, Ballajja C. Prasannakumara ³, Bijjanal J. Gireesha ¹
and Ioannis E. Sarris ^{4,*} 

¹ Department of Studies and Research in Mathematics, Kuvempu University, Shimoga 577451, India; shankar.gsch@gmail.com (B.M.S.); bjgireesu@gmail.com (B.J.G.)

² Department of Mathematics, Government Science College (Autonomous), Hassan 573201, India

³ Department of Studies and Research in Mathematics, Davangere University, Davangere 577002, India; dr.bcprasanna@gmail.com

⁴ Department of Mechanical Engineering, University of West Attica, 12244 Athens, Greece

* Correspondence: sarris@uniwa.gr; Tel.: +30-694-167-2950



Citation: Shankaralingappa, B.M.; Prasannakumara, B.C.; Gireesha, B.J.; Sarris, I.E. The Impact of Cattaneo–Christov Double Diffusion on Oldroyd-B Fluid Flow over a Stretching Sheet with Thermophoretic Particle Deposition and Relaxation Chemical Reaction. *Inventions* **2021**, *6*, 95. <https://doi.org/10.3390/inventions6040095>

Academic Editors: M.M. Bhatti and Sara I. Abdelsalam

Received: 29 October 2021

Accepted: 23 November 2021

Published: 25 November 2021

Publisher's Note: MDPI stays neutral with regard to jurisdictional claims in published maps and institutional affiliations.



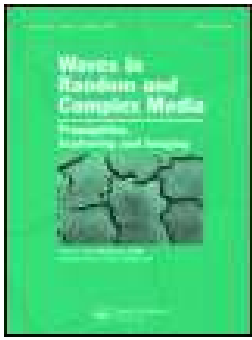
Copyright: © 2021 by the authors. Licensee MDPI, Basel, Switzerland. This article is an open access article distributed under the terms and conditions of the Creative Commons Attribution (CC BY) license (<https://creativecommons.org/licenses/by/4.0/>).

Abstract: The current study focuses on the characteristics of flow, heat, and mass transfer in the context of their applications. There has been a lot of interest in the use of non-Newtonian fluids in biological and technical disciplines. Having such a substantial interest in non-Newtonian fluids, our goal is to explore the flow of Oldroyd-B liquid over a stretching sheet by considering Cattaneo–Christov double diffusion and heat source/sink. Furthermore, the relaxation chemical reaction and thermophoretic particle deposition are considered in the modelling. The equations that represent the indicated flow are changed to ordinary differential equations (ODEs) by choosing relevant similarity variables. The reduced equations are solved using the Runge–Kutta–Fehlberg fourth–fifth order technique (RKF-45) and a shooting scheme. Physical descriptions are strategized and argued using graphical representations to provide a clear understanding of the behaviour of dimensionless parameters on dimensionless velocity, concentration, and temperature profiles. The results reveal that the rising values of the rotation parameter lead to a decline in the fluid velocity. The rise in values of relaxation time parameters of temperature and concentration decreases the thermal and concentration profiles, respectively. The increase in values of the heat source/sink parameter advances the thermal profile. The rise in values of the thermophoretic and chemical reaction rate parameters declines the concentration profile.

Keywords: Oldroyd-B liquid; Cattaneo–Christov double diffusion; stretching sheet; thermophoretic particle deposition; relaxation chemical reaction

1. Introduction

The non-Newtonian liquid concerns in fluid mechanics have attracted the interest of various researchers because of their usage in industry and technology. The flow behaviour of non-Newtonian liquids must be studied in depth to have a thorough grasp of them and their various applications. When it comes to non-Newtonian fluid mechanics, engineers, physicists, and mathematicians face a unique challenge. Due to the complexity of non-Newtonian liquids, no one constitutive equation can account for all of their characteristics. As a consequence, many non-Newtonian liquid models have been presented. In recent years, the Oldroyd-B fluid (OBF), which includes the Maxwell liquid and classical Newtonian liquid as special cases, has risen to a unique place among the many fluids of the rate type. Most polymeric and biological fluids have memory and elastic effects, which are accounted for by an OBF. It has been widely used in many applications, with



Darcy-Forchheimer flow of dusty tangent hyperbolic fluid over a stretching sheet with Cattaneo-Christov heat flux

B. M. Shankaralingappa, B. J. Gireesha, B. C. Prasannakumara & B. Nagaraja

To cite this article: B. M. Shankaralingappa, B. J. Gireesha, B. C. Prasannakumara & B. Nagaraja (2021): Darcy-Forchheimer flow of dusty tangent hyperbolic fluid over a stretching sheet with Cattaneo-Christov heat flux, *Waves in Random and Complex Media*, DOI: [10.1080/17455030.2021.1889711](https://doi.org/10.1080/17455030.2021.1889711)

To link to this article: <https://doi.org/10.1080/17455030.2021.1889711>



Published online: 25 Feb 2021.



Submit your article to this journal [↗](#)



View related articles [↗](#)



View Crossmark data [↗](#)

Article

Influence of Thermophoretic Particle Deposition on the 3D Flow of Sodium Alginate-Based Casson Nanofluid over a Stretching Sheet

Bheemasandra M. Shankaralingappa^{1,2}, Javali K. Madhukesh³ , Ioannis E. Sarris^{4,*} , Bijjanal J. Gireesha¹ and Ballajja C. Prasannakumara³

¹ Department of Studies and Research in Mathematics, Kuvempu University, Shankaraghatta, Shimoga 577451, India; shankar.gsch@gmail.com (B.M.S.); bjgireesu@gmail.com (B.J.G.)

² Department of Mathematics, Government Science College (Autonomous), Hassan 573201, India

³ Department of Studies and Research in Mathematics, Davangere University, Davangere 577002, India; madhukeshjk@gmail.com (J.K.M.); dr.bcprasanna@gmail.com (B.C.P.)

⁴ Department of Mechanical Engineering, University of West Attica, 12244 Athens, Greece

* Correspondence: sarris@uniwa.gr; Tel.: +30-2105-381131

Abstract: The wide range of industrial applications of flow across moving or static solid surfaces has aroused the curiosity of researchers. In order to generate a more exact estimate of flow and heat transfer properties, three-dimensional modelling must be addressed. This plays a vital role in metalworking operations, producing plastic and rubber films, and the continuous cooling of fibre. In view of the above scope, an incompressible, laminar three-dimensional flow of a Casson nanofluid in the occurrence of thermophoretic particle deposition over a non-linearly extending sheet is examined. To convert the collection of partial differential equations into ordinary differential equations, the governing equations are framed with sufficient assumptions, and appropriate similarity transformations are employed. The reduced equations are solved by implementing Runge Kutta Fehlberg 4th 5th order technique with the aid of a shooting scheme. The numerical results are obtained for linear and non-linear cases, and graphs are drawn for various dimensionless constraints. The present study shows that improvement in the Casson parameter values will diminish the axial velocities, but improvement is seen in thermal distribution. The escalation in the thermophoretic parameter will decline the concentration profiles. The rate of mass transfer, surface drag force will reduce with the improved values of the power law index. The non-linear stretching case shows greater impact in all of the profiles compared to the linear stretching case.

Keywords: non-linear stretching sheet; Casson fluid; nanofluid; thermophoretic particle deposition



Citation: Shankaralingappa, B.M.; Madhukesh, J.K.; Sarris, I.E.; Gireesha, B.J.; Prasannakumara, B.C. Influence of Thermophoretic Particle Deposition on the 3D Flow of Sodium Alginate-Based Casson Nanofluid over a Stretching Sheet.

Micromachines **2021**, *12*, 1474. <https://doi.org/10.3390/mi12121474>

Academic Editors: Jin-yuan Qian, Zan Wu, Junhui Zhang and Bengt Sundén

Received: 9 November 2021

Accepted: 27 November 2021

Published: 29 November 2021

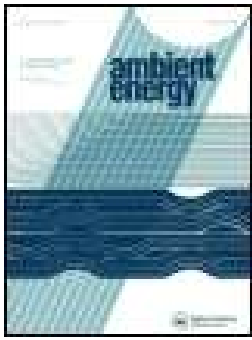
Publisher's Note: MDPI stays neutral with regard to jurisdictional claims in published maps and institutional affiliations.



Copyright: © 2021 by the authors. Licensee MDPI, Basel, Switzerland. This article is an open access article distributed under the terms and conditions of the Creative Commons Attribution (CC BY) license (<https://creativecommons.org/licenses/by/4.0/>).

1. Introduction

The vast range of technological applications of flow across moving or static solid surfaces has aroused the curiosity of researchers. The vaporisation of liquid coatings, the pulling of filaments through a static liquid, crystallization process techniques, the production of rubber and plastic films, and the nonstop cooling of fibre use these concepts. The research community has been studying various elements of such flows since the emergence of boundary layer models. Vajravelu [1] introduced the classical problem of two-dimensional motion caused by a non-linearly extending surface. Three-dimensional (3D) modelling must be considered to obtain a more precise estimation of flow and thermal transfer characteristics. As a result, many researchers have focused their efforts on studying three-dimensional flows. Recently, Gireesha and Umeshaih [2] examined the consequence of non-linear thermal radiation on a magnetohydrodynamic (MHD) 3D flow of Jeffery nanofluid flow over a non-linearly porous extending sheet. The statistical analysis of a three-dimensional MHD convective Carreau nanofluid flow caused by a bidirectional non-linear stretching sheet with a heat source and zero mass flux was swotted by Sabu et al. [3].



MHD flow and melting heat transfer of dusty Casson fluid over a stretching sheet with Cattaneo–Christov heat flux model

B. J. Gireesha , B. M. Shankaralingappa , B. C. Prasannakumar & B. Nagaraja

To cite this article: B. J. Gireesha , B. M. Shankaralingappa , B. C. Prasannakumar & B. Nagaraja (2020): MHD flow and melting heat transfer of dusty Casson fluid over a stretching sheet with Cattaneo–Christov heat flux model, International Journal of Ambient Energy, DOI: [10.1080/01430750.2020.1785938](https://doi.org/10.1080/01430750.2020.1785938)

To link to this article: <https://doi.org/10.1080/01430750.2020.1785938>



Published online: 01 Jul 2020.



Submit your article to this journal [↗](#)



Article views: 76



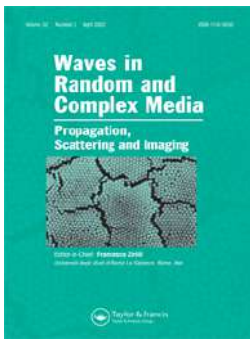
View related articles [↗](#)



View Crossmark data [↗](#)



Citing articles: 1 View citing articles [↗](#)



Particle shape effect on MHD steady flow of water functionalized Al_2O_3 nanoparticles over wedge

K. Thanesh Kumar, Pudhari Srilatha, Talib K. Ibrahim, B. M. Shankaralingappa, B. J. Gireesha & M. Archana

To cite this article: K. Thanesh Kumar, Pudhari Srilatha, Talib K. Ibrahim, B. M. Shankaralingappa, B. J. Gireesha & M. Archana (2022): Particle shape effect on MHD steady flow of water functionalized Al_2O_3 nanoparticles over wedge, Waves in Random and Complex Media, DOI: [10.1080/17455030.2022.2053234](https://doi.org/10.1080/17455030.2022.2053234)

To link to this article: <https://doi.org/10.1080/17455030.2022.2053234>



Published online: 28 Mar 2022.



Submit your article to this journal [↗](#)



View related articles [↗](#)



View Crossmark data [↗](#)